STUDIES ON HEAT TRANSFER IN MICROCHANNEL

Ph.D. Thesis

By
KADAM SAMBHAJI TANAJI

DISCIPLINE OF MECHANICAL ENGINEERING
INDIAN INSTITUTE OF TECHNOLOGY INDORE

AUGUST 2017

STUDIES ON HEAT TRANSFER IN MICROCHANNEL

A THESIS

Submitted in partial fulfillment of the requirements for the award of the degree

of

DOCTOR OF PHILOSOPHY

by

KADAM SAMBHAJI TANAJI

DISCIPLINE OF MECHANICAL ENGINEERING

INDIAN INSTITUTE OF TECHNOLOGY INDORE

AUGUST 2017

INDIAN INSTITUTE OF TECHNOLOGY INDORE

CANDIDATE'S DECLARATION

I hereby certify that the work which is being presented in the thesis entitled **STUDIES ON HEAT TRANSFER IN MICROCHANNEL** in the partial fulfillment of the requirements for the award of the degree of **DOCTOR OF PHILOSOPHY** and submitted in the **DISCIPLINE OF MECHANICAL ENGINEERING, Indian Institute of Technology Indore**, is an authentic record of my own work carried out during the time period from July 2011 to August 2017 under the supervision of **Dr. Ritunesh Kumar**, **Associate Professor, IIT Indore.**

The matter presented in this thesis has not been submitted by me for the award of any other degree of this or any other institute.

Signature of the student with date
(KADAM SAMBHAJI TANAJI)

This is to certify that the above statement made by the candidate is correct to the best of my/our knowledge.

Signature of Thesis Supervisor with date
(Dr. Ritunesh Kumar)

KADAM SAMBHAJI TANAJI has successfully given his/her Ph.D. Oral Examination held on 10th August 2017.

Signature of Chairperson (OEB)
Date:

Signature of External Examiner
Date:

Signature of Thesis Supervisor
Date:

Signature of PSPC Member #1
Date:

Signature of PSPC Member #2
Date:

Signature of Convener, DPGC
Date:

Signature of Head of Discipline
Date:

ACKNOWLEDGEMENTS

I would like to thank that almighty God, for his continuous blessings, it had been sole reasons for the completion of this work.

First of all, I would like to express my sincere appreciation to my supervisor **Dr. Ritunesh Kumar** for his endless patience, continuous support and encouragement during whole research work. This work could not have been accomplished without his valuable guidance and support at every phase of the research.

Many thanks go to my committee member **Dr. E. Anil Kumar**, Discipline of Mechanical Engineering and **Dr. Ram Bilas Pachori**, Discipline of Electrical Engineering for their valuable suggestion and comments during this work. I would like to thank **Dr. Anand Parkash** and **Dr. Antony Vijesh** of Mathematics Dept. IITI, for the helpful discussion while developing mathematical model.

I am also extremely indebted to **Prof. Pradeep Mathur**, Director, Indian Institute of Technology Indore for providing necessary infrastructure and resources to accomplish my research work. I am grateful to him for sanctioning financial support to present research work in International conferences in abroad.

I would like to acknowledge **Dr. Devendra Deshmukh**, Head, Discipline of Mechanical Engineering, **Dr. Kiran Bala**, Inspired faculty, for their continuous motivation and personal cheering.

I am indebted to my lab manager Mr. Aswin Wagh, Mr. Anand Petare, Deputy General Manager (Workshop) and colleagues Vikas, Digvijay, Gurjeet, Suchit. Their company always facilitated me to accomplish PhD work.

I am ever indebted to friends for their cooperation, encouragement and moral support. I would like to thanks my native friends for their continuous motivation, namely, Ganesh, Somnath, Sandip, Manoj, Deepak, Swapnil, Vinayak, Amol, Tushar, Sujit, Nitin, Yogesh.

I wish to thank my friends at IITI, Manish, Vinod, Ajay, Hari, Yogesh, Sandesh, Mayank, Rajan, Pramod, Balmukund, Aniket, Mayur, Sagar, Vinayak, Ajinkya, Agnel and Shaifali.

Finally, I would like to thank my father Late Mr. Tanaji Ramkrushn Kadam for allowing me to do PhD. Also, my mother Ms. Laxmibai Kadam and my brothers Mr. Santosh (Yesunta), his wife (Kavita) and daughters (Anushka and Pari) for the most needed encouragement to finish my studies.

Last but not the least; special thanks are given to my wife, Deepali, for years of support and my daughter, Krushnali. Without their sacrifice, it would have been impossible for me to complete this work.

Kadam Sambhaji Tanaji

In Loving Memory

of

my father

Late Shree Tanaji Ramkrushna Kadam (1962-2014)

my friend

Late Shree Sharad Rangnath More (1986-2015)

LIST OF PUBLICATIONS

List of International Journals

1. **Kadam S. T**., Kumar R., Baghel K. (2014), Simplified model for prediction of bubble growth at nucleation site in microchannels, ASME J Heat Trans, 136, DOI: 10.1115/1.4026609.
2. **Kadam S. T**., Kumar R. (2014), Twenty first century cooling solution: microchannel heat sink, Int J Therm Sci, 85, 73-92, http://dx.doi.org/10.1016/j.ijthermalsci.2014.06.013.
3. Kumar R., **Kadam S. T**. (2015), Development of new critical heat flux correlation for microchannel using energy based bubble growth model, ASME J Heat Transf, 138, DOI:10.1115/1.4032148
4. **Kadam S. T.**, Kumar R., Understanding of bubble growth at nucleation site using energy based non-dimensional numbers and their impact on CHF condition in microchannel, (Submitted).

List of international conferences

1. **Kadam S. T**., Kumar R. (2014), Variation of important non-dimensional numbers during bubble growth at nucleation site in microchannels, *4th Micro and Nano Flows Conference*, 7-10 September, London, UK,.
2. **Kadam S. T**., Kumar R., Baghel K. (2013), Bubble growth at nucleation cavity in microchannels, *Proceedings of the ASME 2013 4th International Conference on Micro/Nanoscale Heat and Mass Transfer*, 11 -14 December, Hong Kong, China.

ABSTRACT

Due to rapid evolution in a wide range of technologies in twentieth century, heat dissipation requirement has increased very rapidly especially from compact systems. There is an urgent need for high-performance heat sinks to ensure the integrity and long life of these petite systems. Use of forced convection cooling has been limited by the requirement of the excessively high flow velocity and associated noise and vibration problems. Microchannel heat sink seems to be most reliable cooling technology due to its superior command over heat carrying capability. Detail literature review of the microchannel heat sink addressing various aspects such as flow visualization, flow regime map, bubble dynamics, pressure drop and heat transfer characteristics, different instabilities and critical heat flux (CHF) has been carried out. Formation of the first bubble at nucleation site is an inception of flow boiling in microchannel. Present study is emphasis in understanding bubble dynamics in microchannel and its theoretical modeling. A new energy balance bubble growth model has been proposed to predict the bubble growth behavior at nucleation site in microchannel. It is assumed that heat supplied at nucleation site is divided between the liquid phase and the vapor phase as per instantaneous void fraction value. The energy consumed by the vapor phase is utilized in bubble growth and overcoming resistive effects; surface tension, inertia, drag, gravity and change in momentum due to evaporation. Developed model shows good agreement with available experimental results. In addition, the bubble waiting time phenomenon for flow boiling is also addressed using proposed model. Waiting time predicted by the model is also close to that obtained from experimental data. Further, bubble growth model is extended to address bubble dynamics during bubble growth at nucleation site for microchannel in terms of non-dimensional energy ratio numbers and their variation from bubble inception until departure. New non dimensional energy ratio is also proposed, which helps in differentiating inertia controlled and thermal diffusion controlled region

during bubble growth at nucleation site. This new non dimensional energy ratio (E_1) is the ratio of the energy required for bubble growth to the energy required to overcome the surface tension effect. Moreover, effort has been made to develop new CHF model for microchannel combining non dimensional analysis and energy based bubble growth model. Two separate CHF correlations for refrigerants and water have been developed following a semi-empirical approach. Both CHF correlations show good agreement with experimental CHF data than previously proposed CHF correlations.

Eventually, heat transfer and pressure drop behavior of single phase flow in open type microchannel are measured experimentally. An experimental test rig is design and fabricated to carryout experimental investigation. Performance of the two configurations of the microchannel heat sink is tested: (1) microchannels with fins, (2) microchannels without fins. It is found that fins in the microchannel intensified heat transfer performance of open type microchannel heat sink by 15%. Whereas, penalty in pressure drop increased by around 18%. Overall thermal performance of the extended open type microchannel is found to be above unity for all operating condition.

TABLE OF CONTENTS

Table of contents (continued) **Page No.**

Table of contents (continued) **Page No.**

LIST OF FIGURES

LIST OF TABLES

NOMENCLATURE

A	Area (m^2)
A_p	Plenum cross section area (m^2)
AR	Aspect ratio
a	Bubble centroid (m)
C_c	Contraction coefficient
Co	Confinement number
Cp	Specific heat (J/kgK)
C_{vv}	Two phase parameter based on laminar liquid-laminar vapor flow
C_{vt}	Two phase parameter based on laminar liquid-turbulent vapor flow
D	Diameter (m)
E	Non-dimensional energy ratio
E_{bubble}	Energy required for bubble growth (W)
Er	Energy required to overcome resistive effect (W)
e	Surface roughness (m)
F	Force (N)
f	Fanning friction factor
f_{app}	Apparent friction factor for developing single-phase liquid flow
f_D	Darcy friction factor
G	Mass flux (kg/m^{2}s)
g	Acceleration due to gravity (m^2/s)
H	Height (m)
H_b	Distance between heater and microchannel bottom wall (m)
H_g	Glass thickness (m), Gap thickness
h	Heat transfer coefficient (W/m^{2}K)
h_{fg}	Latent heat (kJ/kg)
K	Thermal conductivity (W/mK), Coefficient
K_c	Contraction coefficient

K_∞	Hegenbach factor
L	Channel length (m)
l	Heated length of channel (m)
M	Molecular mass of the fluid (kg/kmol)
m	Mass flow rate (kg/s)
N	Number of microchannel
N_f	Number of fin
Nu	Nusselt number
ΔP	Pressure drop (Pa)
P	Pressure (bar)
Pr	Prandtl number
P_r	Reduced pressure (Inlet pressure/saturation pressure)
Re	Reynolds number
R_p	Surface roughness parameter (μm)
r	Bubble radius (m)
r_h	Hydraulic radius (m)
r_i	Instantaneous bubble radius (m)
Q_{net}	Net heat supplied (w)
q''_{CHF}	Critical heat flux (W/m^2)
q''	Effective heat flux (W/m^2)
T	Temperature (°C)
t	Time (s)
u	Mean velocity in port (m/s)
u_{ch}	Mean velocity in microchannel (m/s)
V	Velocity (m/s), Bubble volume (m^3)
v	Specific volume (m^3/kg), Liquid mean velocity (m/s)
v_{fg}	Difference in specific volume of saturated liquid and vapor
W	Width (μm)
We	Weber number
W_f	Fin width (μm)
X	Martinelli parameter

x_e	Thermodynamic equilibrium quality
x_L	Equilibrium quality at end of the heated length

Greek Symbols

α_{in}	Inlet void fraction
α_{out}	Outlet void fraction
β	Aspect ratio
η	Fin efficiency, Overall thermal performance factor
θ	Static contact angle (°)
μ	Dynamic viscosity (Pa-s)
σ_c	Contraction area ratio
σ_e	Expansion area ratio
ε	Void fraction.
ρ_l	Liquid density (kg/m^3).
ρ_v	Vapor density (kg/m^3).
σ	Surface tension (N/m)
τ	Shear stress (N/m^2)

Subscripts

1	Deep plenum.
2	Shallow plenum
3	Three sided wall heating
a	Acceleration
atm	Atmosphere
ave	Average
b	Base
bulk	Bulk
c	Contraction, Minimum visible cavity, Channel
cb	Convective boiling
ch	Channel
conv	Convective
c/s	Bubble cross section, Cross section
dev	Developing region

dyn	Dynamic
e	Expansion
eff	Effective
FV	First visualization
f	Friction, Fluid, Fin
fdev	Fully developed region
g	Gas, Gravity, Gap
h	Hydraulic
ht	Heat transfer
i	Inertia, Inlet, Instantaneous value when used with volume and areas
in	Inlet
incep	Inception
l	Liquid
MCHS	microchannel heat sinks
m	Evaporation momentum
min	Minimum visible
nb	Nucleate boiling
nh	Non heating
out	Outlet
s	Bubble surface, Solid surface
sat	Saturation
sf	Surface tension
sh	Shear
sp	Single phase
sub	Subcooled
T	Total
tp	Two phase
vt	Laminar liquid-turbulent vapor flow
vv	Laminar liquid-laminar vapor flow
w	Waiting, Wall

CHAPTER 1

INTRODUCTION

1.1 Introduction

Heat dissipation requirement in many cutting edge applications such as microelectronics, microsensor, microactuator etc. is rapidly rising as per Moore's law [1], which stated that the number of transistors per square inch on integrated circuit (IC) will be almost doubling every year. As number of transistors increases, the amount of energy to be dissipated as heat from the chip also goes on increasing. Hence, efficient cooling of such systems becomes mandatory for ensuring consistent performance and long life of the systems without requiring frequent maintenance. Heat generation rate has gone up to 10^2 W/cm^2 in densely packed integrated circuit (ICs) [2, 3] and laser mirror [4], 10^3 W/cm^2 in aviation and VLSI industry [5] and 10^4 W/cm^2 in fusion reactor and defense application [6, 7]. Further miniaturization and addition of new functionality in coming future will increase the heat dissipation requirement in aforementioned applications. Such high heat dissipation requirement from small base area even uproots the possibility of using conventional size heat sink working on two phase heat transfer mode. Here, some of cooling techniques such as forced air convection, heat pipe and jet impingement are discussed in brief.

1.1.1 Forced air convection

Forced convection air cooled technique, as shown in Fig. 1.1, is simple and widely used for cooling of the computer chips for low heat dissipation rate. Many improvements have been made like optimization in heat sink design and thermal consideration in the integrated circuit layout. However, these improvements do not meet the requirements and its usage is restricted for heat flux beyond 100 W/cm^2 [8].

1.1.2 Heat pipe

Heat pipe is a device used for cooling purpose, having no moving part. It consists of two region i.e. evaporator, adiabatic section and condenser embedded in the metal pipe which is attached to the heat dissipation surface. Figure 1.2 shows simple schematic of the heat pipe [10]. Limited volume of working fluid is a main problem with use of heat pipes in electronics due to the wick structures, which limits the heat carrying capacity of the heat pipe. Current heat pipes heat sinks are used for removal heat power about 100 W [11].

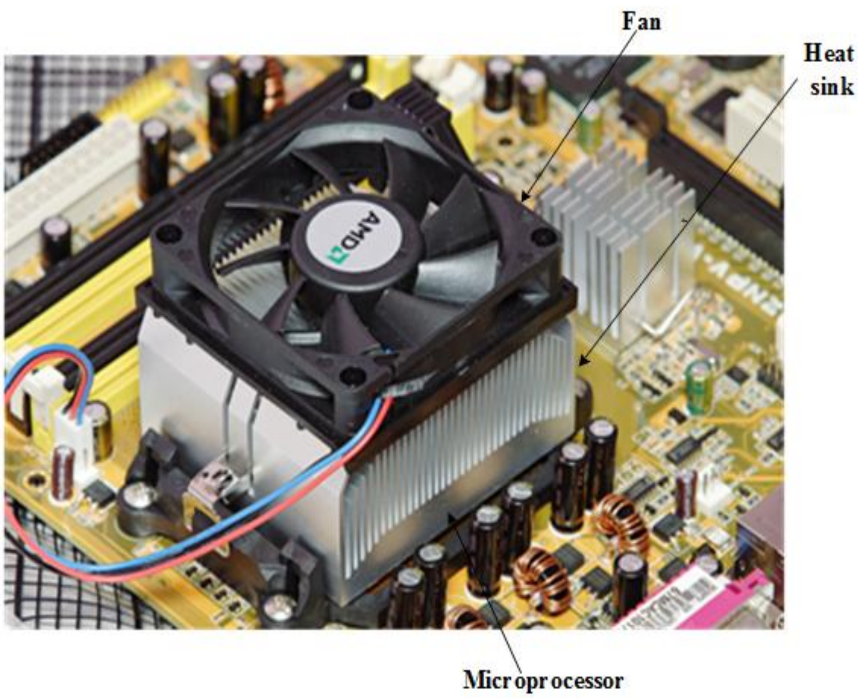

Figure 1.1 Finned heat sink and fan clipped onto a microprocessor [9]

1.1.3 Jet impingement

Arrays of the nozzles are used to impinge a liquid on the heat transfer surface in jet impingement cooling method as shown in Fig. 1.3. Higher heat transfer rate can be achieved by smaller jet diameter with higher number of nozzles in jet array. Multi jet arrangement offers heat removal rate up to 300 W/cm^2 [12]. However, to achieve this high heat flux requirement, jet impingement method has to overcome issues like high pumping power requirements, control of the jet velocity and prone to possible surface erosion and nozzle obstruction. Thus, there is an urgent need of the enhanced cooling techniques that can meet the heat dissipation requirements of the aforementioned applications.

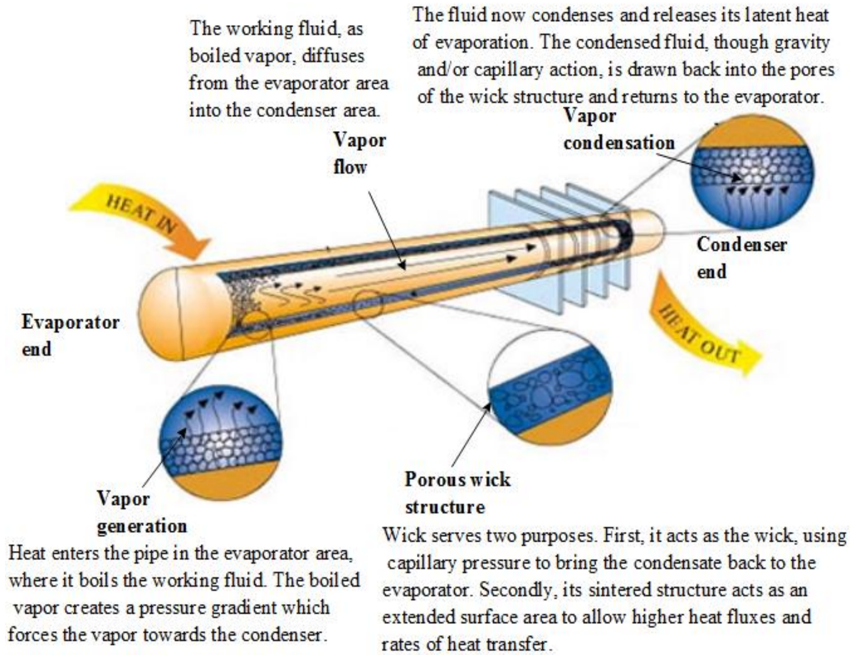

Figure 1.2 Heat pipe arrangements [10]

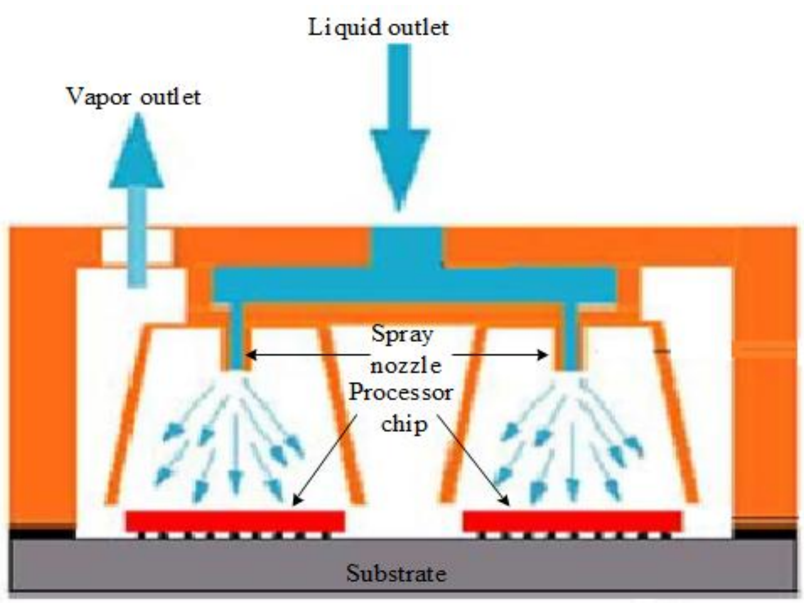

Figure 1.3 Jet impingement cooling method

1.1.4 Microchannel heat sink

For removal of higher amount of heat, microchannel heat sink is one of most promising solution of the twenty first century. Heat can be removed either by single phase or by two phase (flow boiling) flow through microchannel. In case of the single phase liquid flow, large surface area to volume ratio is due to small hydraulic diameter which is responsible for high heat removal. Single phase liquid flow in microchannel heat sink is capable of removing heat flux over 500 W/cm^2 [13]. Under high heat flux condition, microchannel heat sinks with single phase that are limited by the high pumping power requirements due to large pressure drop, and non uniform temperature distribution because they rely of sensible heat of the fluid [14].

Heat generation in aforementioned applications crosses 10^4 W/cm^2. Hence, flow boiling in the microchannel heat sinks seems to be more reliable solution over single phase flow in microchannel for high heat dissipation task. Thermal performance of the flow boiling in microchannels is impressively high due to the combined effect of very small hydraulic diameter and associated latent heat of evaporation. It can remove heat flux of more than 10^3 W/cm^2 [15]. Based on its superiority, different companies started its implementation in real life application. Recently, IBM scientists addressed that liquid cooled microchannel heat sinks are capable of maintaining super computer's component temperature below 45°C and found that overall energy consumption of the cooling system is reduced by 40% as compared to conventional air cooled systems [16]. Gradually, microchannel heat sinks are expected to be used in variety of other day to day applications.

1.2 Motivation of the study

Heat dissipation requirement will continue to rise with more advancement in technologies and further reduction in the size of above mentioned applications. Continuous quest for miniaturization and enhanced functionality demands have further narrowed down available options.

Flow boiling in microchannel can help in efficient cooling of the aforementioned applications without abdicating their performance level. Considering above facts, it can be concluded that flow boiling in microchannel heat sinks seem to be the plausible solution of twenty first century over cooling problems as it offer several advantages such as:

- Very high heat transfer coefficient can be obtained due to combined effect of small hydraulic diameter and involvement of latent heat of evaporation.
- Low pressure drop due to low flow rate resulted into low parasitic power requirement.
- Uniform temperature distribution along the surface can be achieved due to constant vaporization temperature.
- Low coolant and material inventory requirement.
- Compact size due involvement of micron size channel.

However, flow boiling in microchannels, while very promising solution of thermal management of highly compacted systems in twenty first century, is still a subject of intense research that requires comprehensive investigation. While designing the microchannel heat sink based application, challenging issues related to the flow boiling in microchannel heat sink have to be addressed such as bubble dynamics (which has great influence on the flow boiling in microchannel heat sink) and its intrinsic relation with different boiling mechanism, critical heat flux etc. Further, understanding of the heat transfer augmentation techniques in microchannel heat sink and its impact on the performance of microchannel heat sink is underlying in case of the single phase liquid flow. Following section gives brief idea about the thesis organization.

1.3 Organization of the Thesis

This thesis is organized in six chapters, the first chapter provides brief introduction to the research problem.

Chapter 2 reviews the previously reported work by researchers in the field of microchannel heat sink. This comprises both single phase liquid flow and two phase boiling flow in microchannel. It covers various aspects of microchannel heat sink such as historical background, flow visualization, flow regime map, bubble dynamics, pressure drop, heat transfer and comparative assessment of heat transfer coefficient correlations, associated instabilities and their mitigation methods, critical heat flux (CHF) and findings of the previous work etc. The conclusions emerging from the literature review and the objectives of the present work have been reported at the end of this chapter.

Chapter 3 deals with a detailed theoretical modeling of the bubble grow that nucleation site in microchannel. New theoretical energy based bubble growth model has been proposed and its validation has been checked by comparing its prediction with reported experimental works of [38, 39, 81, 186] and detailed numerical study of [35]. Furthermore, energy based bubble growth model is explored to discuss the waiting time phenomena in microchannel. Moreover, effort has been made to develop the energy based non dimensional energy ratio utilizing the energy based bubble growth and their variation during bubble growth at nucleation site from bubble inception to bubble departure is discussed. Eventually, an intrinsic connection of these ratios with inertia controlled region, thermal diffusion controlled region and critical heat flux is discussed.

Energy based bubble growth model is extended along with non dimensional analysis to develop the separate critical heat flux correlations for water and refrigerants and is discussed in chapter 4. These correlations are developed in conjunction with non dimensional analysis. The validity of proposed CHF correlations has been checked by comparing against of different experimental studies and also with existing CHF correlations.

Chapter 5 deals with experimentation of single phase liquid flow in open type microchannel heat sink. Experimental test rig is developed to study the heat transfer and pressure drop characteristics of two types of open microchannel heat sinks (1) microchannels with fins, (2) microchannels without fins. Their performance analysis and comparison are presented.

The overall conclusions of the present work and the recommendations for future work are discussed in **chapter 6**.

CHAPTER 2

LITERATURE SURVEY

This chapter deals with comprehensive literature review on two phase flow boiling in microchannel heat sink. It covers various aspects of microchannel heat sink such as flow visualization, flow regime map, bubble dynamics, pressure drop, heat transfer and comparative assessment of heat transfer coefficient correlations, associated instabilities and its mitigation methods and critical heat flux (CHF). The conclusions emerging from the literature review and the objectives of the present work are reported at the end of this chapter.

2.1 Introduction

In order to overcome the problem of high heat flux removal from small area, first time Tuckerman and Pease [17] had developed microchannel heat sink made up of silicon to remove heat flux of 790 W/cm^2 with water as working fluid. They found that the performance of VLSI circuit was accelerated with such type of microchannel heat sink. Keyes [18] carried out theoretical analysis of finned microchannel heat sink with conventional heat exchanger theory and concluded that the size of fin and channel dimensions could be optimized to provide maximum cooling under wide range of application. Thermal performance tests were conducted on silicon and indium phosphate microchannel heat sinks by Phillips [4]. He found that the thermal performance of microchannel heat sink was approximately two times better than conventional channel heat sink. Missaggia et al. [19] developed a microchannel heat sink (40 channels of dimension (W, H) (100, 400) μm made through etching on silicon wafer) for cooling of two dimensional high power density diode laser arrays, the use of microchannel heat sink provided significant increase in optical power output.

Classification of the microchannel is controversial issues. Some authors have classified based on channel dimension, whereas others believe that it should be based on flow stability. Following is the summery of criteria reported in literature to distinguish between microchannel and macrochannel. Kandlikar and Grande [20,21] had proposed the range as 10 μm ≤ D ≤ 200 μm and Mehendale et al. [22] had suggested the range as 1 μm ≤ D ≤ 100 μm for indentifying microchannel, where D is the diameter of tube or smallest dimension for other cross-sections. Cornwell and Kew [23] and Kew and Cornwell [24] had defined the confinement number (*Co*) in order to distinguish between macro to micro scale flow boiling as given by equation (2.1);

$$Co = \left[\frac{\sigma}{g(\rho_l - \rho_v){D_h}^2}\right]^{1/2} \tag{2.1}$$

As per their proposed criteria, channels with $Co \geq 0.5$ can be classified as microchannels, as influence of the gravity was surpassed by the surface tension above this level.

Manufacturing of the microchannel of required shape and size on required material is another major issue. Researchers have used different manufacturing techniques for the fabrication of microchannel. Table 2.1 summarizes few of the typical manufacturing techniques and the type of microchannel produced.

Kandlikar and Grande [20, 21] had reported that the technology to fabricate microchannels had quickly evolved from the miniaturization of traditional machining techniques (milling and sawing) to the adoption of modern techniques (anisotropic wet chemical etching, dry plasma etching and surface micromachining, LASER cutting) used in the semiconductor manufacturing industry. These techniques have changed the scenario of microchannel heat sink field, lot of companies i.e. IBM Zurich Research laboratory, AAVID THERMALLOY, Furukawa electric Co., Ltd. and Siliton R&D Corporation have come in business related with microchannels.

Table 2.2, presents the summary of geometric parameters of microchannel, working fluid and operating conditions used by different researchers. Figure 2.1 shows typical parallel microchannel heat sink and different cross sections of microchannel used.

Table 2.1

Different microchannel fabrication techniques

Author	**Process**	**Material**	**Dimensions (W, H) µm**
Papautsky et al. [25]	Electroplating	Silicon and Glass	Rectangular, W = 300 to 1500, H = 50 −100
Lee et al. [26]	Micro-milling	Copper	Rectangular, W = 194 to 534, H = 5 * W
Wu and Cheng [27]	Photolithography method	Silicon	Trapezoidal, W_1 = 251, W_2 = 155.7, H = 56.5
Mei et al. [28]	Micro – moulding	Copper and Aluminium	Rectangular, W = 137 − 174, H=400
Wu et al. [29]	Deep reactive chemical etching	Silicon	Rectangular, W = 483.4, H = 50
Chen and Garimella [30]	Saw- Cutting	Silicon	Rectangular, W = 100, H = 389
Lee et al. [31]	Reactive ion etching	Silicon	Rectangular, W = 100, H = 100
Hwang et al. [32]	Laser	Mythacrylate	Circular, D_h = 8 − 20

It can be concluded from Table 2.2 that majority of studies have been carried out on copper and silicon substrate based test sections. Copper is very popular material in thermal process equipments due its high thermal conductivity and silicon is good semiconductor extensively used in VLSI and electronics industries. From the Table 2.2, it can also be concluded that most of studies have been carried out by using water or refrigerant as working fluid. Water is not an appropriate coolant for electronic devices due to its current carrying capability and corrosive nature, which may be responsible for complete burnout of electronic devices or scale formation hampering heat transfer characteristics. However, common refrigerants used in field of microchannel heat sink are R410A, R134a, FC – 72, FC – 77, HFE – 7000 and HFE – 7100. Table 2.3 compares thermo-physical properties, ODP and GDP values of different refrigerant. Thermo – physical properties play an important role in boiling process like high viscosity of liquid phase, stabilizes thin liquid layer in slug flow and annular flow. Hence, ensure smooth boiling process (by slowing down flow instabilities). Similarly, large density of vapor will facilitate boiling process by ensuring more energetic vapor bubbles (vapor bubble will travel along heated wall after departure, discussed in the flow visualization section) are generated in boiling process. High liquid density is not desirable as it tries to suppress growth of bubble. Whereas, low enthalpy of vaporization, activates large number of nucleation site at early stage. Hence, facilitating boiling process and reduces the thermal non equilibrium of liquid and vapor phase. Thus, low enthalpy of vaporization also helps in reducing the boiling instabilities associated with microchannel.

In following sections, effort has been made to review single phase flow and two phase flow in microchannel. In case of flow boiling, different flow patterns observed, flow regime map, pressure drop characteristics, heat transfer characteristics of microchannel heat sink are discussed in detail. Dependency of pressure drop and heat transfer characteristics of microchannels on various parameters is described in pressure drop and heat transfer section. Further, instabilities associated with microchannels such as flow reversal, pressure fluctuation, wall temperature fluctuation, Ledinegg instability and their mitigation techniques are addressed.

Table 2.2

Summary of microchannel geometry and operating parameters

Sr no	**Author**	**Fluid**	**Microchannel Geometry ((W, H)/ D) (µm), N**	**Material**	**Operating condition**
1	Tuckerman and Pease [17]	Water	Rectangular, W = 56, 50, 55, H = 320, 287,302	Silicon	P_{in} =1 − 2 bar, q" = 1810 to 7900 kW/m^2, $\dot{V}$=4.7x10^{-6} to 8.6x10^{-6} m^3/s
2	Peng and Wang [33]	Deionised water	Rectangular, W = 600, H = 700, N = 3	Stainless steel	T_{in} = 30 − 60 60 °C, G = 1480 − 3947 kg/m^{2}s
3	Qu and Mudawar [34]	Water	Rectangular, W = 231, H = 713, N = 21	Copper	G = 135 − 402 kg/m^{2}s , T_{in} = 30, 60 °C, P_{out} = 1.17 bar
4	Qu and Mudawar [35]	Deionised water	Rectangular, W = 215, H = 821, L = 44.8 mm, N = 21	Copper	G = 86 − 368 kg/m^{2}s, T_{in} = 30, 60 °C, P_{out} = 1.13 bar
5	Steinke and Kandlikar [36]	Water	Rectangular, W = 214, H = 200, L = 57.15 mm, N = 6	Copper	G =157 − 1782 kg/m^{2}s, q" = 5 − 930 kW/m^2, T_{in} = 22 °C, P_{out} =

Table 2.2 continued

					1.13 bar, x = 0 – 1
6	Coleman and Krause [37]	R134a	D_h = 830, L = 5 mm, N = 18 ports		G = 185 to 785 kg/m^2s
7	Lee et al. [38]	Deionised Water	Trapezoidal, W_1 = 102.8, W_2 = 59.18, H = 30.1, N = 1	silicon	q" = 1.47 – 449 kW/m^2, G = 170 – 477 kg/m^2s
8	Li et al. [39]	Deionised Water	Trapezoidal, W_1 = 100, W_2 = 41, H = 41, N = 2	Silicon	q" = 12.4 – 303 kW/m^2 G = 105 – 555 kg/m^2s
9	Lee and Mudawar [40]	R134a	Rectangular, W = 231, H = 713 µm, N = 21	Copper	P = 1.44 – 6.6 bar, x_{in} = 0.001 – 0.25, x_{out} = 0.49 – supreheated, q = 316 – 938 kW/m^2, G = 127 – 654 kg/m^2s
10	Kosar et al. [41]	Water	Rectangular, W = 200, H = 264, L = 10 mm, N = 5	Silicon	q" = 280 – 4450 kW/m^2, G = 41 – 302 kg/m^2s
11	Ling et al. [42]	Distilled Water	D = 13, 20 , L = 40 to 100 mm,	Silex Glass	At room temperature

Table 2.2 continued

12	Chen and Garimella [43]	FC – 77	Rectangular, W = 389, H = 389, N = 24	silicon	T_{in} = 71 ^oC, P_{exit} = atms., q" = 94 − 617 kW/m^2, $\dot{m}$ = 35, 47, 60 ml/min,
13	Yun et al. [44]	R410a	Rectangular, D_h = 1360 (N = 8), 1440 (N = 7)		T_{sat} = 0, 5, 10 ^oC, q" = 10 to 20 kW/m^2, G = 200 to 400 kg/m^2s
14	Sobierska et al. [45]	Water	Rectangular, W = 860, H = 2000, L = 330 mm, N = 1,	Copper	T_{sub} = 2 − 20 K, T_{in} = 36.4 − 36.5, P_{out} = atms., q" = 100 kW/m^2, G =50 −1000 kg/m^2s
15	Huh et al. [46]	Deionised water	Rectangular, W = 100, H = 107, N = 1	Silicon	P_{out} = atms., q" = 200 − 530 kW/m^2, G = 170, 360 kg/m^2s
16	Qi et al. [47]	Liquid Nitrogen	Circular tube, D = 531, 834, 1042, 1931, N = 1,	stainless steel	Re = 10000 to 90000, system pressure = 1 − 9 bar
17	Lee and Mudawar [5]	HFE – 7100	Rectangular, W = 123.4 to 259, H = 304.9 to 1041.3, L = 10 mm, N = 24,11	Copper	T_{in} = 30 ^oC, P_{out} = 1.138 bar, q" = 0 − 7500 kW/m^2, G = 670 to 6730 kg/m^3s

Table 2.2 continued

18	Wang et al. [48]	Water	Trapezoidal, W_1 = 427, W_2 = 208, H = 146, N = 8	Silicon	T_{in} = 35 ºC, q" = 184.2 − 485.5 kW/m^2
19	Agostini et al. [49]	R134a	Circular, D = 509, 790, N =1	Glass	T_{in} = 30 ºC, q" = 6.5 − 31.8 kW/m^2, G = 200 to 1500 kg/m^2s, x = 0.02 to 0.19
20	Singh et al. [50]	Water	D_h = 142 constant, L = 20 mm, β = 1.24, 1.43, 1.56, 1.73, 2.56, 3.6, 3.75, N = 1	Silicon	q" = 290 − 366 kW/m^2, G = 82.4 − 126.2 kg/m^2s
21	Ergu et al. [51]	Distilled Water, Potassium ferricyanide	Rectangular, W = 3700, H = 107.9, L = 35 mm, N = 1	Acrylic	T_{in} = 25 ºC, for pressure drop: Re = 100 − 845, for mass transfer: Re = 18 – 550
22	Schilder et al. [52]	Ethanol and Water	Circular tube, D_h = 600 , L = 110 mm, N =1	Glass	T_{in} = 23 ºC, G = 158 – 317 kg/m^2s, q" = 50 − 97 kW/m^2, Re = 25 −202

Table 2.2 continued

23	Krishnamurthy and pales [53]	HFE – 7000	Rectangular, W = 200, H = 243, L=10 mm, N = 5 , pin: D = 100 µm dia, N = 24, Pitch ratio= 4	Silicon	q" = 100 − 1100 kW/m^2, G = 350 − 827 kg/m^{2}s
24	Balasubramanian et al. [54]	Deionised Water	Rectangular, W = 300, aspect ratio = 4, N = 40,	Copper	T_{in} = 90 °C, q" = 1400 kW/m^2, G = 100 to 133 kg/m^{2}s
25	Megahed [55]	FC – 72	Rectangular, W = 225, H = 276, L = 16 mm, N = 45, Three cross linked channel 500 µm wide,	Silicon	q" = 7.2 to 104.2 kW/m^2, G = 99 to 290 kg/m^{2}s, X_{out} = 0.01 to 0.71
26	Barlak et al. [56]	Distilled Water	Circular, D_h = 200 − 589, L/D = 16 to 265, N =1	Stainless	T_{in} = 25 °C, Re = 100 − 1000
27	Edel and Mukherjee [57]	Water	Rectangular, W = 201, H = 266, L = 25 mm, N = 1	Brass	T_{in} = 64, 80, 98 °C, $\dot{m}$ = 0.41 to 0.82 ml/min

Table 2.2 continued

28	Lu and Pan [58]	Water	Rectangular Varying cross section, Inlet: W = 100, H = 76, Outlet: W = 560, H =76, N = 10	Silicon	G = 99 − 293 kg/m^2s
29	Lee et al. [31]	Water	Rectangular, W = 50, 100, H = 46, 48, 100, L = 64 mm, N = 1	Silicon	P_{in} = 1 − 10.15 bar, T_{in} = 24 °C, G = 138.9 kg/m^2s
30	Park et al. [59]	FC – 72	Rectangular, D_h = 67 (N=190), D_h = 278 (N=95).	stainless steel	case I: D_h = 67, q" = 0.6 − 3.6 kW/m^2, G = 188 − 742 kg/m^2s case II: D_h = 278, q" = 6 − 45.1 kW/m^2, G = 449 − 1538 kg/m^2s

Table 2.3

Thermo-physical properties at 25 °C, Global warming potential and ozone depletion potential index of different cooling fluids

Refrigerant	Dynamic viscosity (10^{-4} kg/m s)	Liquid Density (kg/m^3)	Vapor density (kg/m^3)	Thermal conductivity (W/ m K)	Enthalpy of evaporation (kJ/kg)	Surface tension (N/m)	ODP	GWP
R134a	1.95	1206	32.35	0.081	177.78	0.0080	0	1300
R410a	1.84	1189	29.94	0.076	185	0.0091	0	1890
FC – 72	6.40	1680	13.23*	0.057	88	0.0105	0	9000
FC – 77	6.14	1664	16.63*	0.059	89	0.0130	0	9000
HFE – 7000	6.00	1400	5.71	0.075	142	0.0124	0	400
HFE – 7100	6.10	1520	9.87#	0.062	125	0.0136	0	320
R290	0.97	492	21.18	0.094	335	0.0070	0	3
R600a	1.50	549	9.12	0.088	229	0.0101	0	4
R718	0.09	997	0.023	0.607	2441	0.0719	0	0

Foot note: * T_s = 56.6 °C, # P_{sat} = 1 bar, ODP = Ozone Depletion Potential
Courtesy: properties collected from various websites and product data sheet.

Eventually, critical heat flux (CHF) associated with microchannel is discussed briefly and different CHF correlations are also compiled.

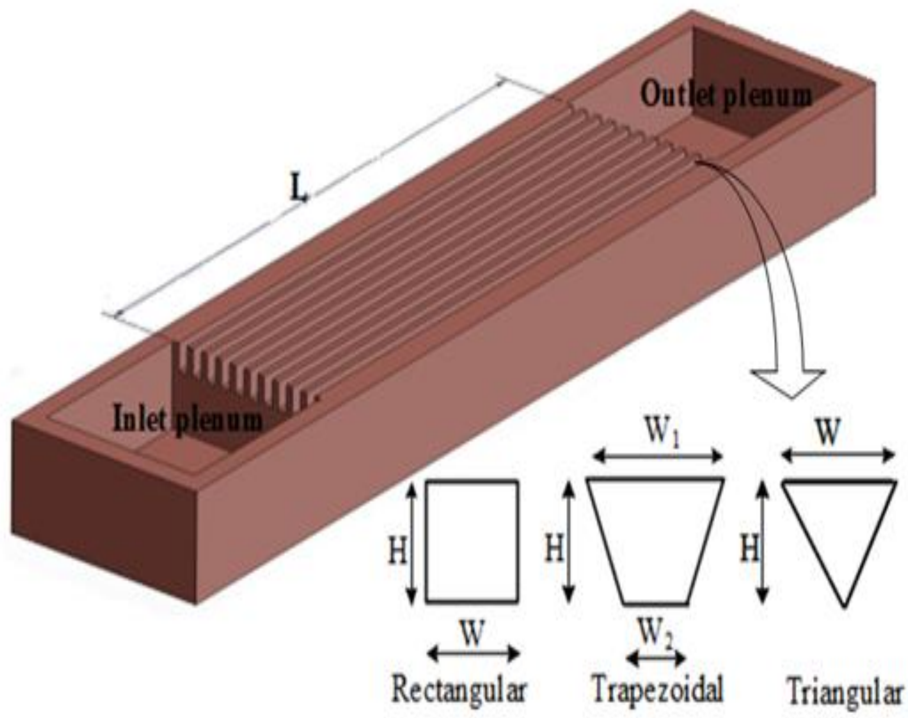

Figure 2.1 Parallel microchannel heat sink

2.2 Flow visualization

The study of different flow regimes that exist in microchannels is important because the pressure drop and heat transfer characteristics can not be predicted accurately in absence of comprehensive information about different types flow regime. It is very difficult to predict the sequence of flow patterns in microchannels unlike conventional channels without high speed photography. In conventional channels as explained by Thome [60], the sequence of flow pattern in vertical channel are: bubbly, slug, churn, wispy-annular and annular flow, whereas for the horizontal channel are: bubbly, slug, plug, annular, stratified, annular with mist and wave flow exists, as shown Fig. 2.2 (a) and 2.2 (b), respectively.

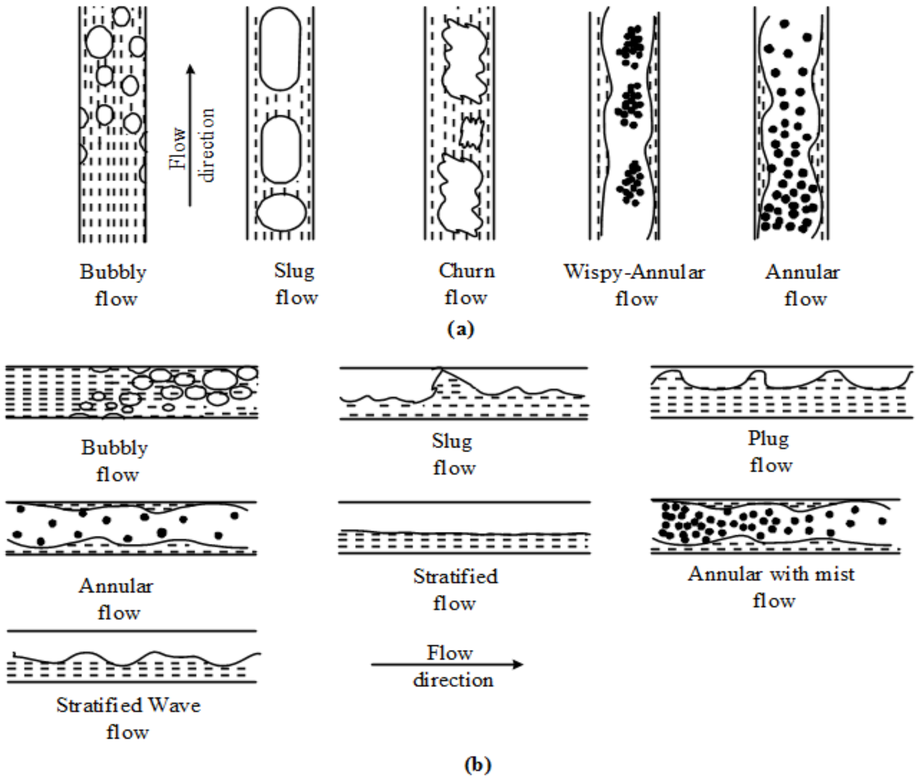

Figure 2.2 Flow patterns in conventional channel (a) vertical channel, (b) horizontal channel

In case of microchannels flow patterns are quite different than conventional channels. Hence, two phase flow pattern maps and flow boiling heat transfer methods developed for macrochannels fail to predict behavior of microchannels through simple extrapolation. Pfahler et al. [61] carried out experiments on three different microchannels (W, H) (100, 8) (100, 17) and (53, 135) using N – propanol. They found that the largest cross section channel roughly followed Navier – Stokes equation. However, as the channel size reduced, they observed significant deviation from Navier – Stokes prediction.

In the last two decades various researchers have carried out flow visualization study on a single microchannel, multiple microchannels and microtubes.

Sobierska et al. [45] performed experiments using water in a single rectangular microchannel (W, H) (2000, 860) and observed bubbly, slug and annular flow. Lee and Mudawar [5] visualized the nucleate flow boiling at inlet, middle and outlet section of microchannel and related the flow patterns with boiling curve. Megahed and Hassan [62] carried out experiments on 45 rectangular microchannels (W, H) (225, 276) with FC – 72 as working fluid over wide range of the heat flux (q = 60.4 −130.6 kW/m^2) and mass flux (G = 341 − 531 kg/m^2s). They concluded that two phase flow in microchannel can be divided into three main flow regimes; bubble, slug and annular flow. Zhang and Fu [63] performed experiments on vertically upward microtubes of 531 and 1042 μm inner diameter using liquid nitrogen as working fluid. They reported bubbly flow, slug flow, churn flow and annular flow as the main flow patterns. They also observed confined bubble flow (Fig. 2.3 (a)), mist flow, bubble condensation (Fig. 2.3 (b)) and flow oscillation in their study. Two types of flow pattern were reported by Kawahara et al. [64]; (a) quasi-homogeneous (Fig. 2.3 (c)): shorter gas plugs at high liquid flux (b) quasi-separated (Fig. 2.3 (d)): longer gas bubble surrounded by smooth and wavy liquid film at high gas flux. Experiments were performed by mixing Nitrogen gas with distilled water and aqueous solution of ethanol on circular tube of diameter 250 μm. Choi and Kim [65] carried out water and Nitrogen-gas two-phase flow experiments over range of superficial velocity of liquid (0.06 – 1.0 m/s) and gas (0.06 – 72 m/s) on five different types of rectangular microchannels (D_h = 141, 143, 304, 322 and 490). They reported the bubbly flow, slug bubble flow, elongated bubble flow (Fig. 2.3 (e)), transition flow and liquid ring flow (Fig. 2.3 (f)) in their flow visualization study. The elongated bubble flow and the liquid ring flow are repeated periodically in transition flow. Choi et al. [66] observed bubbly flow, transition flow and liquid ring flow on rectangular microchannels of varying aspect ratio (α = 0.16, 0.47, 0.67, 0.92). They found that two phase flow became homogeneous with decrease in aspect ratio, which they attributed to decreased liquid thickness at low aspect ratio. Cornwell and Kew [23] conducted experiments with R-113 flowing inside rectangular microchannels of size (W, H) (1200, 900). They reported three flow patterns isolated bubble (≈ bubbly flow), confined bubble and annular flow in their experimental study.

Kasza et al. [67] performed experiments on small channel of D_h = 3.53 mm. They observed small size nucleating bubble under the thin liquid film that formed between channel wall and vapor core during the slug flow as shown in Fig. 2.3 (g). Similar situation is even possible in case of microchannels but observing such small vapor bubble underneath liquid layer is quite difficult in case of microchannels, dominating surface tension effect worsens the situation.

Chung and Kawaji [68] performed experiments on four microtubes (D = 50, 100, 250, 530), using physical mixture of water and nitrogen gas as working fluid. They observed the bubbly, slug, swirling pattern in churn flow (Fig. 2.3 (h)), serpentine-like gas core in churn flow (Fig. 2.3 (i)), liquid bridge in slug-annular flow (Fig. 2.3 (j)) and fully developed annular flow for tubes with 250 and 500 µm diameter. Bubbly, churn, slug-annular flows were absent for 50 and 100 µm tubes. The serpentine-like gas flow was having meandering motion. This was attributed to the strong effect of surface tension and liquid viscosity in 50 and 100 µm tubes, which prohibited the turbulence.

Lee and Mudawar [69] carried out experiments to study the two phase flow patterns in test specimen with 53 rectangular microchannels (W, H) (231, 713) for R134a at different heat flux and inlet quality. They observed that bubbly flow regime and nucleate boiling occurred only at low qualities (x_e < 0.05) corresponding to low heat fluxes. Whereas, annular film evaporation flow dominated at high heat fluxes producing medium quality (0.05 < x_e < 0.55) or high quality (0.55 < x_e < 1.0).

Chen and Garimella [43] carried out flow visualization study of test specimen with 24 square microchannels of size 389 µm and wall thickness of 100 µm. They performed experiments under wide range of heat and mass flux. They observed that at low heat fluxes, bubbly flow was dominant, with the bubbles coalescing to form vapor slugs with increase in heat flux. At high heat fluxes, the flow regimes after slug

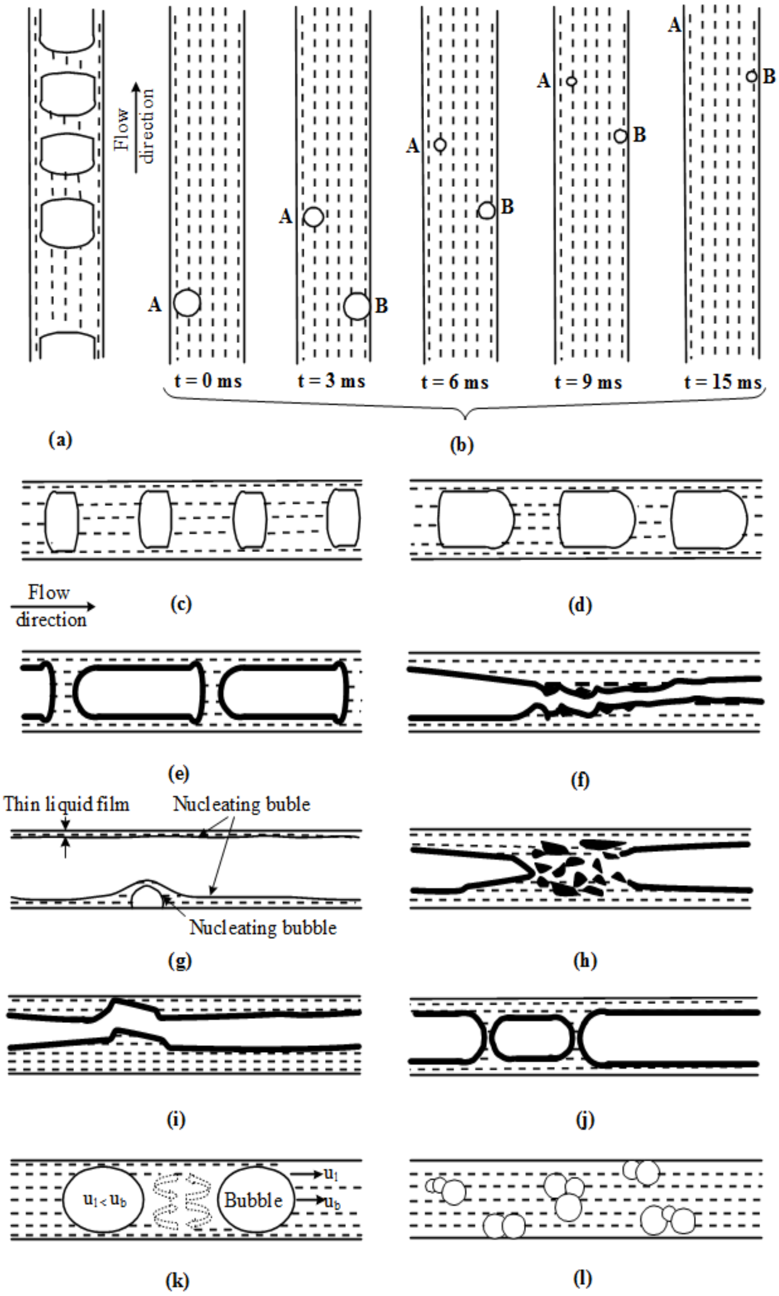

Figure 2.3 Various types of flow patterns in microchannel (a) confined bubble flow [63], (b) bubble condensation [63], (c) quasi-homogeneous flow [64], (d) quasi-separated flow [64], (e) elongated bubble flow [65], (f) liquid ring flow [65], (g) bubble nucleation in the liquid film [67], (h) swirling pattern in churn flow [68] , (i) serpentine-like gas core in churn flow [68], (j) liquid bridge in slug–annular flow [68], (k) circulation in microchannel [70], (l) bubble interacting [53]

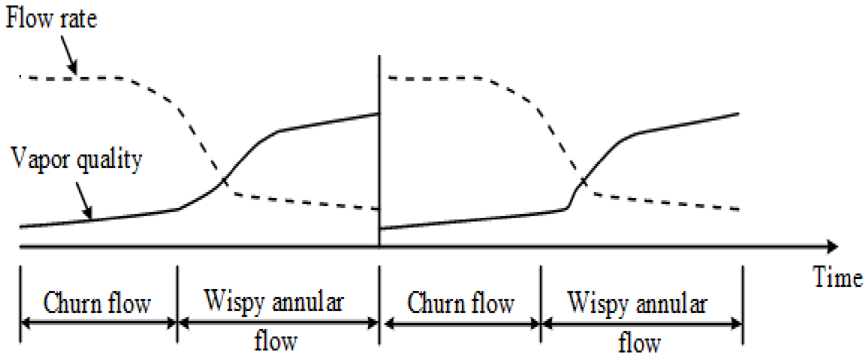

Figure 2.4 Periodic variation of flow patterns with time (Chen and Garimella [43])

flow in the downstream portion of the microchannels had characteristic of alternating wispy-annular flow and churn flow (Fig. 2.4), while flow reversal was observed in the upstream region near the microchannel inlet. They attributed the alternating flow patterns to the flow reversal towards upstream and found that flow reversal continued as heat flux was increased and it lasted until the complete dryout of the channel was reached.

Wang et al. [48] carried out flow visualization study in parallel microchannels with three different types of inlet/outlet configurations. Type – A had inlet and outlet port perpendicular to the microchannels. In Type – B, flow entering to and exiting from microchannels freely without restriction. Type – C had inlet restrictions of triangular shape and flow entering with restriction and exiting without restriction in microchannels. They observed that the flow pattern changed with operating condition as well as inlet/ outlet configuration. With B type configuration, steady bubbly/slug flow regimes were observed for vapor quality $x_e < 0.044$, in the range from $0.044 < x_e < 0.103$, bubbly/ annular alternating flow regimes were observed and for the value of vapor quality $x_e > 0.103$, annular/mist alternating flow were observed. With C type configuration, bubbly, elongated bubble and annular flow were the main flow regimes observed.

Kashid et al. [70] reported circulation of the liquid behind bubble as shown in Fig. 2.3 (k) within the liquid slug. Which they attributed to the formation of vacuum generated behind the rapidly moving vapor bubble that caused the recirculation of liquid at nose of the upcoming bubble. They further concluded that the recirculation may cause bubble distortion at tail of leading bubble or at nose of upcoming bubble. Agostini et al. [49] observed similar distortion at the tail of elongated bubbles in their study.

Schilder et al. [52] observed in their flow visualization study that the bubble growth took place in both upstream and downstream directions leaving behind a thin evaporating wavy liquid film on the tube. They attributed the shear between vapor and liquid phase during slug flow for the formation of wavy pattern on the film surface. Lee et al. [31] also carried out similar flow visualization study for microchannel with single artificial cavity. An explosive bubble growth was observed at cavity due to high degree of superheat at artificial nucleation site. Krishnamurthy and Peles [53] observed the flow for rectangular microchannels (D_h = 222 μm) containing a single row of 24 pin fin of 100 μm in diameter. Flow visualization revealed the existence of isolated bubbles, bubbles interacting (Fig. 2.3 (l)), multiple flow and annular flow.

Barber et al. [71] had observed the variation in interfacial velocities of growing vapor slug over time along with bubble nucleation and growth in a single microchannel (D_h = 727) using refrigerant FC – 72. The downstream end of the bubble was called as nose and upstream end was named as bubble tail. The tail and the nose moved with same velocity until bubble was not confined. After confinement, tail velocity was reduced due to inertia of incoming fluid suppressing the bubble tail. Whereas, the bubble nose velocity increased as negligible resistance of fluid was present in downstream direction.

Megahed [55] carried out flow visualization study on 45 straight microchannels (D_h = 727) connected through three cross-links of width 500 μm. They carried out experiments under heat flux range (37 – 69.6 kW/m^2), mass flux range (109 – 195 kg/m^{2}s) and vapor quality range (0.2 – 0.4). They observed only slug flow under entire range of experimentation. They did not observe transition from slug flow to annular flow, which they attributed to transverse flow within the cross link.

Edel and Mukherjee [57] observed that elongation of the vapor bubble after confinement Fig. 2.5 (a – b) resulted into suppression of preceding vapor bubble. As vapor bubble started expanding after confinement, pressure spike was generated in upstream direction. This pressure suppressed preceding bubble, hence the size of preceding bubble was reduced as shown in Fig. 2.5 (c). This smaller size bubble again started growing, when larger bubble pushed enough liquid out of the channel for decreasing built up pressure as shown in Fig. 2.5 (d).

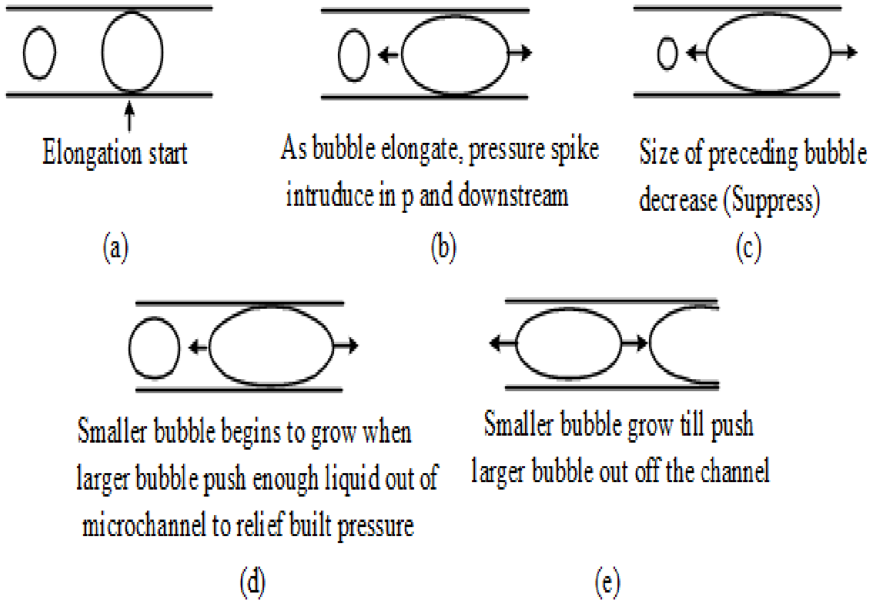

Figure 2.5 Sequence of interacting bubble suppression in microchannel (Edel and Mukherjee [57])

The small vapor bubble growth continued until it pushed larger bubble out of the channel, as shown in Fig. 2.5 (e). Entire process repeated itself in the same sequence after some time interval.

David et al. [72] performed experiments with single copper microchannel (W, H) (124, 94) using mixture of air and water as working fluid. One side wall of the microchannel was made up off the hydrophobic Teflon membrane of 65 µm thicknesses and 220 nm pore diameter in order to study the effect of venting process. This wall acted as venting wall, which helped in removing the air only through it, thus avoiding instability due to vapor locking. Air was injected from opposite site of hydrophobic thin membrane. They also observed that with increase in inlet air flow, flow patterns followed sequence of bubble, wavy, wavy-stratified, stratified, slug annular, annular at constant water flow rate.

Table 2.4

Summary of important flow visualization studies

Author	**Remark**
Kasza et al. [67]	• Bubble growing pattern inside thin liquid film (below vapor slug) tries to avoid early occurrence of dryout condition.
Chung and Kawaji [68]	• They studied effect of microtube diameter on flow pattern.
Lee and Mudawar [69]	• Bubbly, slug, alternating wispy-annular flow and churn flow.
Schilder et al. [52]	• Temporary dryout can even initiate at low vapor quality due to instable liquid film. • Instability issues are more severe in case of low viscous flow.
Krishnamurthy and Peles [53]	• Extended surface can help in mitigating early stage flow instability.
Megahed [55]	• Flow stability can be improved by mass flux retardation from downward direction.
Edel and Mukherjee [57]	• Instability issues easily provoke in case of single microchannel.
David et al. [72]	• Bubbly flow was observed towards the end of channel due to air venting by hydrophobic membrane.

At higher water flow rates, jetting type breakup was observed and no air venting could take place as annular flow followed by jetting type breakup. Table 2.4 presents main summary of few important flow visualization studies. Use of flow map for predicting two phase pattern is extremely popular and well established for conventional size channels [73 – 77]. Flow map is basically two-dimensional graph with transition criteria for separating various flow regimes of two phase flow. As the state is transformed towards boundary (separating two regimes), it become unstable and further transition beyond boundary converts flow patterns. Few authors have tried to develop flow map for microchannel. Perhaps, Triplett et al. [78] were the first to develop flow map for microchannel. They identified the transition boundaries between different flow patterns using gas liquid superficial velocities as coordinates. Harirchian and Garimella [79] developed comprehensive flow regime map for FC – 77 using non dimensional form of heat flux ($Bl \cdot Re$) as abscissa and convective confinement number ($Bo^{0.5}Re$) as ordinate on flow map. They also suggested new transition criteria ($Bo^{0.5}Re$ < 160) for physical confinement in microchannel. Sur and Liu [80] developed flow map for adiabatic air water two phase flow using modified Weber number (We_G $(D/\lambda)^2$, We_L) as X and Y coordinates. They also observed that boundary of the annular flow regimes shifted to higher gas superficial velocity as the channel dimension is reduced from 324 μm to 100 μm. From the reviewed literature related to flow regime map, it has been observed that exact location of the transition boundaries on flow map varies dramatically even for microchannels of same geometry under same flow conditions. More efforts are needed for developing comprehensive flow map for microchannels.

Authors have also studied complete bubble dynamics in microchannel since its inception through flow visualization. Bubble dynamics (bubble nucleation, growth, departure and its motion along the flow) plays an important role in heat transfer and pressure drop characteristics as well as various flow instabilities during two phase flow of microchannels. First step in the bubble dynamics is the inception of the bubbles at active nucleation site. Basically, nucleation site is small cavity, where the phase change process starts. Bubble grows for certain duration at nucleation site then it departs from it. Bubble departure diameter from nucleation site governs subsequent bubble dynamics. If departure diameter is around equivalent to channel dimension (in case of high heat flux or very small sized microchannel) then confinement may occurs at nucleation site itself [38, 39]. Bubble basically do not detach in such case before start of confinement process. However, if bubble departure diameter is small in comparison to channels dimension then bubble starts travelling along the flow direction [81] at heated surface after departing from nucleation site. Once bubble diameter grows equivalent to channels dimension then confinement process initiates. The bubble growth process rapidly increases after this due to heating from side walls. Once bubble confines complete cross section then starts elongating in flow direction. Elongated bubble finally leaves the microchannel or may lead to flow reversal phenomena (explained in instability section) at high heat flux values. Figure 2.6 shows complete bubble dynamics for microchannel.

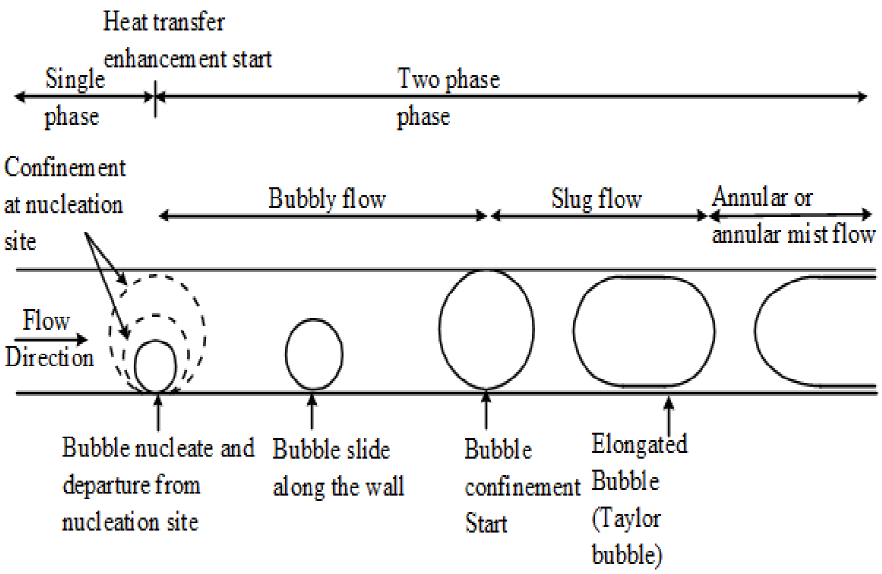

Figure 2.6 Complete bubble dynamics in microchannel

Hsu [82], first time proposed the phenomena of bubble inception at nucleation site during boiling. As per his theory bubble nucleation is possible only if the minimum surrounding temperature of nucleation site being at least equal to the saturation temperature corresponding to liquid pressure.

Mukherjee et al. [83] further concluded that bubble formation can also take place, if flowing fluid is mixture of liquid and gas in addition to the condition proposed by Hsu [82]. Various authors had proposed quadratic equation for finding the nucleation cavity radius, solution of these equations give minimum $r_{c,min}$ and maximum $r_{c,max}$ cavity radius. Hsu [82], Davis and Anderson [84] and Kandlikar and Spiesman [85] have proposed the relation for cavity radius for subcooled boiling based on different bubble height. Lui et al. [81] have developed relation for cavity radius for saturated flow boiling in microchannels. At heated surface number of cavities are present, but nucleation takes place only if cavity radius obeys following criteria: $r_{c,min} < r_c < r_{c,max}$. Such cavities are called as active nucleation sites.

Bubble growth at nucleation site is divided between two regions; inertia controlled region and diffusion controlled region (Bogojevic et al. [86]; Yin et al. [87];) as shown in Fig. 2.7. In the initial stage size of bubble is very small, bubble growth is governed by the reaction force of the surrounding liquid at the bubble interface. This stage is called as inertia controlled region. As the bubble starts growing, thermal diffusion (between vapor liquid interface and surrounding liquid) effect increases. Once it overcomes inertia effect, subsequent bubble growth is governed entirely by thermal diffusion process [86]. Liu et al. [81] observed linear bubble growth at nucleation site from its inception to the departure. Whereas, Lee et al. [38] observed explosive bubble growth also for a few combinations of heat flux and mass flux values. However, they failed to explain reason behind explosive bubble growth. In case of Lee et al. [85] experimental study, bubble even stretched away in flow direction during its growth at nucleation site.

Further, they observed that bubble confined entire channel cross-section before departing from the nucleation site.

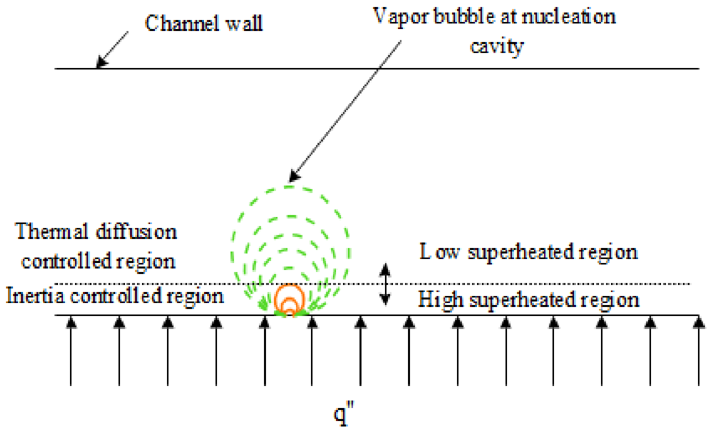

Figure 2.7 Inertia controlled and thermal diffusion controlled regions

Kew and Carnwell [24] were first to report the confined bubble growth in case of the small tube. Barber et al. [71] classified the confinement as the partial confinement (D_{bubble} = min (W, H) and full confinement (D_{bubble} = max (W, H). They observed that partial confinement produced both radial and elongated growth, whereas full confinement was coupled with elongated growth only. Fu et al. [89] carried out bubble growth study before and after bubble departure from nucleation site for minichannel (D = 1.3 − 1.5 mm) using nitrogen as working fluid. They reported linear and constant bubble growth in both cases. Gedupudi et al. [90] carried out experiments for the studying the growth of confined bubble in rectangular microchannel using water as working fluid. They observed exponential bubble growth after confinement from microchannel wall. Yin et al. [91] concluded that elongation of the bubble after confinement is influenced by effective heat supplied and bubble moving velocity along the flow. Recently, Tuo and Hrnjak [92] carried out complete bubble dynamic study using R134a refrigerant. They observed linear bubble growth before confinement and exponential bubble growth in axial direction after confinement. Exponential bubble growth was accredited to intensive evaporation of thin liquid layer trapped between vapor bubble and microchannel wall.

Bubble grows under the influence of various forces since its inception until final departure. These forces play vital role in bubble dynamics. Helden et al. [93] considered lift, surface tension, buoyancy, expansion due to pressure difference, drag and temperature induced drag force in analysis of bubble detachment from artificial nucleation site along vertical wall of square channel. Zeng et al. [94] considered surface tension, drag force in flow direction, drag force due to unstable growth, shear, buoyancy, hydrodynamic pressure and contact pressure force for analyzing the bubble departure diameter during flow boiling in horizontal square channel and Yeoh and Tu [95] considered same forces for analyzing the bubble departure diameter during flow boiling in vertical annular channel. Qu and Mudawar [96] had acknowledged drag and surface tension force (neglecting effect of buoyancy force) for the analysis of bubble departure during flow boiling in horizontal microchannels. Kandlikar [97] introduced an evaporation momentum force for analysis of the critical heat flux (CHF) characteristics in pool boiling and applied it successfully for CHF analysis in microchannels [98]. Kandlikar [99, 100] considered inertia, drag, surface tension, shear, gravity and evaporation momentum force for the scale effect on flow boiling heat transfer in microchannels.

Many researchers have carried out detailed numerical analysis of the bubble growth for studying boiling mechanism in microchannels. Mukherjee and Kandlikar [101] simulated a vapor bubble growth in microchannel. They had observed that bubble grows linearly till it fills the microchannel cross section, afterwards it expands rapidly due to evaporation of the liquid film trapped between wall and the vapor bubble [102]. They further concluded that bubble growth rate increases with increase in degree of superheat and decreases with increase in mass flux. Mukherjee et al. [83] carried out numerical analysis of the bubble growth and its effect on heat transfer in microchannels of cross section (200 μm x 200 μm). They observed that the wall superheat has dominating effect on bubble growth than the Reynolds number. Zhuan and Wang [103] carried out numerical study of the vapor bubble growth at nucleation site in microchannel. They concluded that in early stages bubble growth is dominated by the surface tension force and in later stages bubble growth is controlled by the heat supplied. Wang et al. [104] presented hybrid methodology (coupling micro-resolution particle image velocimetry and three dimensional iterative numerical simulation) that can be used for reconstructing three dimensional bubble geometry and finding associated three dimensional velocity field around the bubble during growth at nucleation site. Gedupudi et al. [90] addressed flow instabilities and uneven distribution associated with parallel microchannels. They developed one-dimensional model for partially and fully confined bubble growth in a single microchannel to study the effect of upstream compressibility due to subcooled boiling in the preheater or trapped non-condensable gas as associated with parallel microchannels. Majority of these numerical studies had been carried out for the bubble that is already departed from nucleation cavity. Moreover, detailed numerical bubble growth study is cumbersome and time consuming.

2.3 Pressure drop

It is of significant interest to understand the pressure drop characteristics across microchannel, when designing applications based on microchannel. As hydraulic diameter of microchannel is very small, it is expected that single phase pressure drop per unit length associated with microchannel will be much higher than macrochannels under same operating conditions. Boiling in microchannels even promotes the two phase pressure drop associated in comparison to conventional size channels. In spite of being associated with large pressure drop, microchannel heat sinks had attracted lot of attention due to their strong command over heat transfer characteristics. Large pressure drop is responsible for huge power consumption of the pump utilized. Thus, the study of pressure drop in microchannels is equally important similar to other aspects associated. Two phase flow/pressure drop can be modelled using the homogeneous flow model and separated flow model. In homogeneous flow model, two phases (liquid phase and vapor phase) are treated as a single phase. Another fundamental assumption of homogeneous model is that liquid and vapor have equal velocity. The separated flow model considers the phases to be artificially segregated into two streams, one contains only liquid and anther contains only vapor. The fundamental assumption of the separated flow model is that liquid and vapor have constant but not necessarily equal velocities. The pressure drop across the channel is mainly dependent on the fluid properties (density, viscosity and surface tension), mass flux (flow velocity, mass flow rate or Reynolds number), effective heat supplied (wall temperature), vapor quality and channel geometry (aspect ratio, hydraulic ratio and cross section). Various researchers have studied the effect of these parameters on the pressure drop characteristics of microchannels.

Researchers have carried out pressure drop analysis in single phase, two phase with subcooled and saturated inlet condition in microchannels. Very few studies have been carried out in single phase mode. Qu and Mudawar [105] carried out experimental and numerical study to predict the pressure drop for single phase in rectangular microchannel heat sink using water as working fluid. They observed that pressure drop reduced with increase in heat flux at constant Reynolds number. They accredited it to the decrease in viscosity of water at elevated temperature. Ergu et al. [51] carried out experiments in the range of Reynolds number from 100 – 845 using water as working fluid on rectangular microchannel (W, H) (3700, 107.4). They observed that pressure drop increased linearly with Reynolds number and concluded that single phase pressure drop behavior of microchannel is very much similar to the macrochannel for laminar flow region. Barlak et al. [56] conducted experiments on microtubes (D = 200, 250, 400, 505 and 589) having L/D ratio in the range of 16 – 265 using water as cooling fluid. They observed that at low Reynolds number (Re < 2000), pressure drop was weak function of L/D ratio and linear relationship existed between pressure drop and Reynolds number. Whereas, pressure drop was strongly dependent on L/D ratio at high Reynolds number. Unlike large diameter tubes, smaller diameter tubes faced a noticeable change in pressure drop with L/D ratio beyond Re > 2000. Ling et al. [42] carried out pressure drop analysis on circular tubes of 13 and 20 μm diameter and length ranging from 40 to 100 mm under pressure driven force condition. Linear relationship between the flow rate and pressure drop was projected by them. They further concluded that the flow characteristics of the microtubes are basically in agreement with macroscopic liquid flowing lows. Qi et al. [47] carried out pressure drop study on different diameter tubes (D = 531, 834, 1042 and 1931) of constant length (L = 250 mm) in the range of Reynolds number $10^4 – 9x10^4$. They observed that the total single phase pressure drop increased with increase in mass flux and decrease in tube diameter. It was also observed that friction factor obeyed conventional channel theory for tubes having diameter of 1042 and 1931 μm. However, for the 531 and 834 μm tubes, friction factor value deviated from conventional channel theory. They attributed it to the effect of the surface roughness on friction factor in case of small tubes. Akbari et al. [106] carried out pressure drop analysis on rectangular microchannels of varying aspect ratio in the range of 0.13 to 0.76. They observed that pressure drop increased with increase in the aspect ratio. However, it increased very rapidly as the width of channel also approached to the limiting criteria of microchannel. They also characterized different type of losses such as contraction and expansion loss, developing region and fully developed region loss and loss due to electro-viscous effect. Peiyi and Little [107] carried out single phase experiments on nitrogen, hydrogen and argon gas with eight different microtubes having diameter ranging from 55.81 to 83.08 μm. They concluded that friction factor is dependent on the channel geometry, roughness and mass flux.

Two phase pressure drop is of significant interest as far as flow boiling in microchannels is concerned. Figure 2.8 shows the variation of pressure drop for single phase and two phase with respect to $(q^{"}/q^{"}_{sat})$ for subcooled boiling and saturated boiling region in horizontal orientation of microchannel, following Lee and Mudawar [108]. In the single phase, pressure drop is primarily governed by the behaviour of liquid viscosity with temperature. For fluid like water pressure drop reduces with increase in wall heat flux at constant mass flux due to decrease in liquid viscosity for single phase region. Pressure drop reduction starts decreasing once onset on nucleate boiling (ONB) condition is approached. ONB is the location, where the first bubble forms. ONB indicates the termination of single phase flow and inception of the subcooled boiling region as shown in Fig. 2.8. Formation of bubble introduces two phase pressure drop components, frictional and acceleration. The magnitude of these components increases with increase in heat flux due to growth of vapor bubble or due to formation of new bubble at newly activated nucleation sites. They try to pull up pressure drop associated with microchannel unlike viscosity.

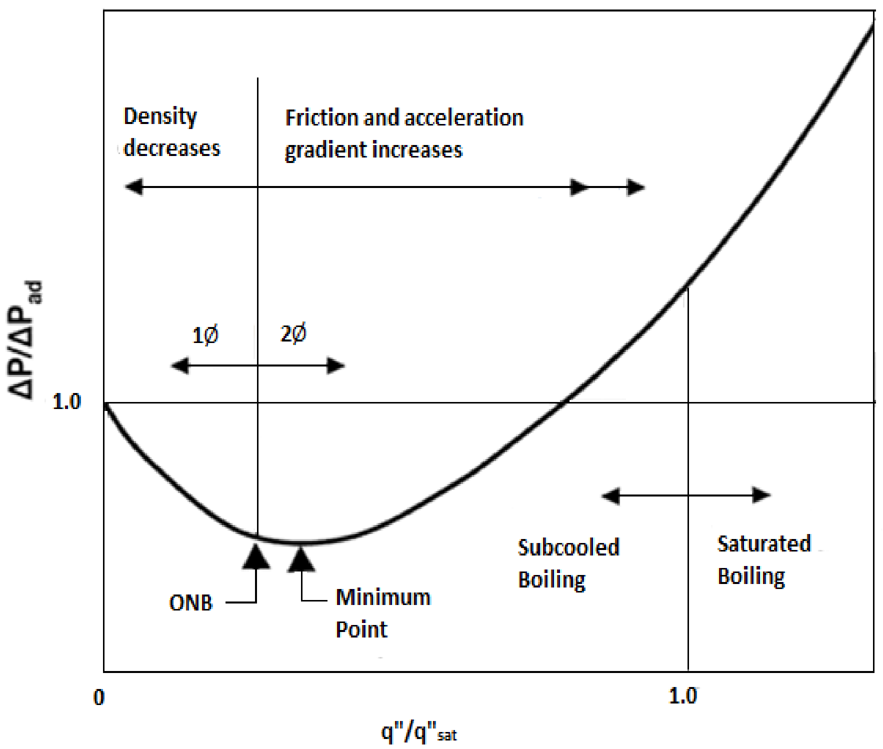

Figure 2.8 Normalized plot of pressure drop versus wall heat flux for subcooled boiling (Lee and Mudawar [108])

In subcooled boiling region pressure drop initially reduces after ONB and attains minima. This was attributed to the higher degree of subcooling, which suppressed the bubble growth initially after ONB. On further increase of heat flux beyond minima condition, the vapor bubble pressure drop components become dominating. Therefore, pressure drop starts increasing with increase in heat flux. This trend continued even in saturated boiling region. However, in case of the vertical orientation gravitational pressure drop/gain (upward flow/downward flow) will influence pressure drop characteristics of both single and two phase flow. Gravitational pressure drop/gain is more dominating than frictional pressure drop in case of single phase flow. As flow shifts from single phase to two phase, effect of frictional pressure drop supersede gravitational effect.

Yun et al. [44] carried out two phase experiments on microchannels of hydraulic diameter of 1.44 mm. They found that pressure drop increased with increase in mass flux at constant saturation temperature. At given mass flux, pressure drop decreased with increase in saturation temperature, which they attributed to change in viscosity and density of R410A.

Lee and Mudawar [40] carried out experiments using R134a to study the pressure drop characteristics in microchannels. Based on combined pressure drop data of R134a and water (Qu and Mudawar [109]), they developed two phase pressure drop multiplier empirical relations for separated flow model incorporating liquid viscosity and surface tension effect. These correlations were used to examine the effect of vapor quality, heat flux and mass flux on total pressure drop characteristics of R134a. They found that at constant heat flux total pressure drop decreased with an increase in exit vapor quality, which they attributed to decrease in mass velocity. They also found that for constant mass flux, pressure drop increased up to particular heat flux value beyond which pressure drop became constant or slightly decreased. Up to particular heat flux value, two phase frictional and accelerational losses increases due to conversion of liquid into vapor. After complete conversion into vapor, two phase frictional loss decreases but it is compensated by the increase in single phase vapor pressure loss.

However, acceleration loss remains at same value over complete conversion into vapor phase. Thus total pressure drop remained constant or slightly decreased beyond particular heat flux value. Balasubramanian et al. [54] had reported increasing trend of pressure drop for the variation of heat flux at constant mass flux in stepwise expanding microchannels with deionised water. However, they observed that in stepwise expanding microchannels pressure drop decreased with increase in mass flux, which was due to increase in mass flux (inducing reduction in saturation flow length). Reduction in saturation flow length reduces the magnitude of two phase pressure drop per unit length, which is substantially higher than magnitude of single phase pressure drop per unit length. They also observed that pressure drop associated with stepwise expanding microchannel was smaller than straight microchannel, which they attributed to the deceleration of vapor in downstream direction.

Megahed [55] carried out pressure drop analysis of cross linked rectangular microchannels. They observed that two phase pressure drop increased linearly with exit vapor quality at a given mass flux and it increased very rapidly with increase in mass flux at constant vapor quality. They further reported slight increases in slope of pressure drop verses vapor quality line at low mass fluxes (G = 111, 141 kg/m^{2}s) and rapid increase in slope at high mass fluxes (G = 191, 245, 290 kg/m^{2}s). They accredited it in favour of presence of cross links between microchannels. The presence of cross link also increased associated sudden expansion and contraction pressure losses in addition to increase in pressure loss due to cross flow. Furthermore, they also compared experimental two phase pressure drop data with pressure drop correlations published by Lee and Garimella [110] for straight microchannels. They found that two phase pressure drop in cross link microchannels is almost 1.5 times greater than regular straight microchannels over tested range of mass flux, except at minimum value of mass flux (G = 111 kg/m^{2}s). From Balasubramanian et al. [54] and Megahed [55] experimental study, it can be concluded that expanding microchannels have superior pressure drop characteristics than straight and cross link microchannels. Sobierska et al. [45] carried out experiments using water as working fluid on a straight vertical single rectangular microchannel in the range of mass flux from 50 to 1000 kg/m^{2}s. They also observed that pressure drop associated with two phase increases with increase in mass flux and exit vapor quality separately. However, pressure drop increased moderately in the range of mass flux (50 – 300 kg/m^{2}s) and rapidly beyond of it. Megahed and Hassan [62] and Park et al. [59] measured experimentally the pressure drop per unit length across rectangular microchannels. In both works, it was observed that pressure drop per unit length increased with increase in mass flux and vapor quality respectively. Megahed and Hassan [62] attributed this behaviour to the impact of void fraction on pressure drop. Park et al. [59] used rectangular microchannels (D_h = 61 and 278 μm) in their experimental study on refrigerant FC – 72. They observed that for a microchannel (D_h = 278 μm) at mass flux of G = 112 kg/m^{2}s, the pressure drop increased continuously beyond vapor quality of 0.9. This was attributed to the absence of turbulent wave at higher vapor qualities because of very thin liquid film. Eventually, they concluded that existing macroscale pressure drop correlations could not be directly used for microscale (below D_h = 100 μm) due to change in flow patterns below this dimension.

Phan et al. [111] analyzed experimentally the effect of surface wettability on two phase pressure drop using four test-sections having single rectangular microchannel (W, H) (5000, 500) and coated with hydrophilic (Polydimethylsiloxane (SiOx), titanium (Ti), diamond like carbon (DLC)) and hydrophobic (Polydimethylsiloxane (SiOC)) substances. These surfaces had static contact angle of 29°, 49°, 63° and 103° respectively. They found that at a given mass flux and exit vapor quality, two phase pressure drop increased significantly with increase in static contact angle, which they attributed to the effect of contact angle on surface tension force generated. For unwetted surface (SiOC) having higher contact angle, surface tension force intended to maintain the bubble at the solid wall, which resulted into increase in frictional pressure drop. On the other hand for wetted surface (SiOx), surface tension helped in proper wetting of the surface. Thus, wetted surfaces were subjected to low two phase pressure drop in comparison to unwetted surface.

Singh et al. [50] investigated the effect of aspect ratio (β = W/H = 1.23, 1.44, 1.56, 1.73, 2.56, 3.6 and 3.75) of rectangular microchannel theoretically as well as experimentally. They observed that the pressure drop first reduced with increase in β, attained minima at $\beta = 1.56$, then started increasing rapidly with increase in β. The occurrence of minima, they speculated in favour of the opposite nature of frictional and accelerational pressure drop with respect to aspect ratio. With increase in β, acceleration pressure drop decreased and frictional pressure drop increased.

Choi and Kim [65] and Choi et al. [66] carried out experiments using water liquid-nitrogen gas adiabatic two phase flow in microchannel. They concluded that the typical two phase pressure drop characteristics of microchannel can be divided in three regions. Region I: Bubbly flow regime, including bubbly, slug bubble and elongated bubble, Region II: transition flow region, Region III: Liquid ring flow regime. In the Region I, number of bubbles amplified the pressure drop on increase in superficial gas velocity. In the Region II, pressure drop decreased due to collapse of elongated bubble on increase in superficial gas velocity. In the Region III, pressure drop increased very rapidly with increase in superficial gas velocity

Table 2.5 summarizes relations proposed by different researches to predict pressure drop across microchannels. Bowers and Mudawar [112] considered the total pressure drop as summation of the single phase, two phase frictional, two phase acceleration and two phase outlet pressure drop components. Qu and Mudawar [109] splited the single phase pressure drop into the developing and the fully developed region pressure drop components and also introduced contraction and expansion pressure drop components to calculate exact total pressure drop associated in microchannels. In two phase flow, vapor has higher velocity than the liquid due to its low density in comparison to corresponding liquid phase. In order to accommodate this effect of liquid and vapor, Lee and Mudawar [40] defined two phase frictional pressure drop component in terms of two-phase pressure drop multiplier (∅). Two phase pressure drop multiplier was defined in terms of Martinelli parameter (X) and two-phase multiplier parameter (C), which defined the type of the two phase flow (Table 2.5). Megahed [55] introduced dynamic two phase pressure drop component, which accounted for the enlargement at outlet and bends of microchannels.

Table 2.5
Summary of pressure drop correlations for microchannel

Author	Channel geometry and fluid (W, H, D) µm	Operating condition	Correlations
Bowers and Mudawar [112]	Circular, D = 2540, 510 R113	P_{in} = 1.38 bar, T_{sub} = 10 − 32 °C, m = 19 − 95 ml/min Subcooled boiling and saturated boiling	$\Delta P_T = \Delta P_{sp} + \Delta P_f + \Delta P_a + \Delta P_{out,nh}$ $\Delta P_a = \left(\frac{G^2}{\rho_f}\right)\left(\frac{v_{fg}}{v_f}\right)(x_L)$ $\Delta P_{sp} = \frac{2\, f_{sp} G^2 L_{sp}}{\rho_f D}$ $\Delta P_f = \left(\frac{2\, f_{tp} G^2 L_b}{\rho_f D}\right)\left[1 + \frac{x_L}{2}\left(\frac{v_{fg}}{v_f}\right)\right]$ $\Delta P_{out} = \left(\frac{2\, f_{tp} G^2 L_o}{\rho_f D_h}\right)\left[1 + x_L\left(\frac{v_{fg}}{v_f}\right)\right]$ $f_{tp} = 0.005$
Qu and Mudawar [109]	Rectangular, W = 231, H = 713 Deionised water	T_{in} = 30, 60 °C, P_{out} = 1.17 bar, G = 134.9 −400.1 kg/m^{2}s Subcooled boiling and saturated boiling	$\Delta P_T = \Delta P_{c1} + \Delta P_{c2} + \Delta P_{sp,dev} + \Delta P_{sp,fdev} + \Delta P_f + \Delta P_a + \Delta P_{e1} + \Delta P_{e2}$ $\Delta P_{c1} = \frac{v_f}{2}\,(G_2^2 - G_1^2) + \frac{v_f K_{c1}}{2}\, G_2^2$ $\Delta P_{c2} = \frac{v_f}{2}\,(G^2 - G_2^2) + \frac{v_f K_{c2}}{2}\, G^2$ $\Delta P_{e1} = \frac{v_f + x_e\, v_{fg}}{2}\,(G_1^2 - G_2^2) + K_{e1}\,\frac{(v_f + x_e\, v_{fg})}{2}\, G_2^2\,,\ K_{e1} = \left(1 - \frac{NA}{A_{p2}}\right)^2$ $\Delta P_{e2} = \frac{v_f + x_e\, v_{fg}}{2}\,(G_2^2 - G^2) + K_{e2}\,\frac{(v_f + x_e\, v_{fg})}{2}\, G^2\,,\ K_{e2} = \left(1 - \frac{A_{p2}}{A_{p1}}\right)^2$ $\Delta P_{sp,dev} = \frac{2\, f_{app} G^2 L_{sp,dev} v_f}{D_h}$ $f_{sp,dev} Re_{sp,dev} = 24\,(1 - 1.355\beta + 1.947\beta^2 - 1.701\beta^3 + 0.956\beta^4 - 0.254\beta^5)$

Table 2.5 continued

			$Re_{sp,d} = \frac{GD_h}{\mu_{sp,dev}}$; $\beta = \frac{W}{H}$ $\Delta P_{sp,fd} = \frac{2\, f_{app} G^2 L_{sp,fdev} v_f}{D_h}$ $f_{app} = \frac{1}{Re_{sp,fdev}} \left[3.44\left(L^{+}_{sp,fdev}\right)^{-0.5} + \frac{\frac{1.089}{\left(4L^{+}_{sp,fdev}\right)} + f_{sp,fdev} Re_{sp,dev} - 3.44\left(L^{+}_{sp,fdev}\right)^{-0.5}}{1 + 1.31\times10^{-4}\left(L^{+}_{sp,fdev}\right)^{-2}} \right]$ $L^{+}_{sp,fdev} = \frac{L_{sp,fdev}}{Re_{sp,fdev} D_h}$; $Re_{sp,fdev} = \frac{GD_h}{\mu_{sp,fdev}}$ $f_{sp,fdev} Re_{sp,fdev} = 24\,(1 - 1.355\beta + 1.947\beta^2 - 1.701\beta^3 + 0.956\beta^4 - 0.254\beta^5)$ $\Delta P_f = \frac{2 f_{tp} G^2 L_{tp} v_f}{d_h}\left[1 + \frac{x_e}{2}\left(\frac{v_{fg}}{v_f}\right)\right]$, $f_{tp} = 0.003$ $\Delta P_a = G^2 v_f x_e$
Lee and Mudawar [40]	Rectangular, W = 231, H = 713 µm R134a	P = 1.44 − 6.6 bar, x_{in} = 0.001 − 0.25, x_{out} = 0.49 − supreheated, q = 316 − 938 kW/m^2, G = 127 − 654 kg/m^{2}s Saturated boiling	$\Delta P_T = \Delta P_c + \Delta P_f + \Delta P_a + \Delta P_{sp,g} - \Delta P_e$ $\Delta P_c = \frac{G^2 v_f}{2}\left[\left(\frac{1}{C_c} - 1\right)^2 + \left(1 - \frac{1}{\sigma_c^2}\right)\right]\left[1 + \frac{v_{fg} x_{e,in}}{v_f}\right]$ $\Delta P_e = G^2 \sigma_e\,(1 - \sigma_e) v_f \left[1 + \frac{v_{fg} x_{e,out}}{v_f}\right]$ $\Delta P_{sp,g} = \frac{2L_{sp,g}}{D_h} f_{sp,g} G^2 v_g$ $f_{sp,g} Re_g = 24\,(1 - 1.3553\beta + 1.947\beta^2 - 1.701\beta^3 + 0.956\beta^4 - 0.254\beta^5)$ for $Re_g < 2000$ $f_{sp,g} = 0.079 Re_g^{-0.25}$ for $2000 < Re_g < 20{,}000$ $f_{sp,g} = 0.046 Re_g^{-0.2}$ for $20{,}000 < Re_g$ $\Delta P_a = G^2 \left\{ \left[\frac{v_g x_{e,out}^2}{\alpha_{out}} + \frac{v_f (1 - x_{e,out})^2}{(1 - \alpha_{out})}\right] - \left[\frac{v_g x_{e,in}^2}{\alpha_{in}} + \frac{v_f (1 - x_{e,in})^2}{(1 - \alpha_{in})}\right] \right\}$ $\alpha = \left[1 + \left(\frac{1-x}{x}\right)\left(\frac{v_f}{v_g}\right)^{2/3}\right]^{-1}$ $\Delta P_f = \frac{2\, G^2 L_{tp}}{D_h x_e} \int_{x_i}^{x_o} f_f (1 - x) v_f \emptyset_f^2\, dx$, $\emptyset_f^2 = 1 + \frac{C}{X} + \frac{1}{X^2}$, $X^2 = \left[(dP/dz)_f / (dP/dz)_g\right]$

Table 2.5 continued

			$C_{vv} = 2.15Re_l^{0.047}We_l^{0.6}$ laminar liquid–laminar vapor $C_{vt} = 1.45Re_l^{0.25}We_l^{0.23}$ laminar liquid–turbulent vapor
Megahed [55]	Rectangular, W = 225, H = 276 FC−72	q = 7.2 to 104.2 kW/m^2, G = 99 to 290 kg/m^{2}s, X_{out} = 0.01 to 0.71 subcooled boiling and saturated boiling	$\Delta P_T = \Delta P_{sp} + \Delta P_{tp}$ $\Delta P_{sp} = \frac{\rho_f}{2}\left[\left(\frac{4f_{sp,l}L_{sub}}{D_h} + K_c + K_\infty\right) u_{ch}^2 + 2K_{90}u^2\right]$ $L_{sub} = \frac{\dot{m}c_p(T_{sat}-T_{in})}{qA}$ $f_{sp,l} = \frac{24}{Re}\ (1 - 1.3553\beta + 1.9467\beta^2 - 1.7012\beta + 0.9564\beta^4 - 0.2537\beta^5)$ $K_\infty = 0.6796 + 1.2197\beta + 3.3089\beta^2 - 9.5921\beta^3 + 8.9089\beta^4 - 2.9959\beta^5$ K_{90}= bending pressure loss coefficient $\Delta P_{tp} = \Delta P_f + \Delta P_a + \Delta P_{tp,dyn}$ $\Delta P_{tp,dyn} = \frac{G^2 v_f}{2}\ (1-\sigma_c)^2\left[1 + x_e\left(\frac{v_{fg}}{v_f}\right)\right],\ \sigma_c = \frac{A}{A_p}$ $x_e = \frac{1}{h_{fg}}\left[\frac{Q_{net}}{m} - C_p(T_{sat} - T_{in})\right]$ $Q_{net} = Q_{input} - Q_{loss}$

2.4 Heat transfer

Heat transfer coefficient is the most important parameter governing the usefulness of microchannel heat sinks. Heat transfer coefficient for flow boiling in microchannels is impressively high due the combined effect of very small hydraulic diameter and associated latent heat of evaporation. Heat transfer coefficient is primarily influenced by fluid properties (density and viscosity), mass flux, effective heat flux, channel geometry (cross section area and aspect ratio) and vapour quality. Various researchers had carried out experimental studies in single phase as well as two phase heat transfer in microchannels. However, major focus had been given to two phase heat transfer studies.

Peng and Wang [33] studied the effect of force convection on single phase heat transfer characteristics using rectangular microchannels (W, H) (700, 600). They observed that decrease in liquid subcooling and increase in flow velocity induced steep increase in heat transfer coefficient. Wang and Peng [113] also carried out single phase forced convection study using six heat sinks of microchannel dimesions (W, H, N) (800, 700, 4), (600, 700, 4), (400, 700, 4), (400, 700, 6), (200, 700, 4) and (200, 700, 6) using water as working fluid. They observed three different trends for the variation of single phase heat transfer coefficient in above microchannels. In first the trend on (800, 700, 4) heat sink, heat transfer coefficient smoothly increased with wall temperature. In second trend on (600, 700, 4), (400, 700, 4) and (400, 700, 6) heat sink, steep increase in heat transfer coefficient at low wall temperature was observed. This was followed by moderate increase in heat transfer coefficient at high wall temperature. In third trend on (200, 700, 4) and (200, 700, 4) heat sink, heat transfer coefficient decreased first and then moderately increased as the wall temperature was increased. They further concluded that heat transfer characteristics in laminar and transition region of microchannels are highly complicated compared to conventional channel. This was attributed to the considerable change in thermo-physical properties of the flowing fluid because of large variation in liquid temperature along the length of microchannel. Qu and Mudawar [105] carried out experimental and numerical study of single phase heat transfer using twenty one rectangular microchannels (W, H) (231, 713) heat sink. They compared the result of numerical study with experimental data and suggested that Navier-Stoke and energy equation can successfully predict heat transfer behavior of the single phase flow. Unlike previous studies, they did not observe the flow transition in the tested range of Reynolds number from 139 to 1672. Qi et al. [47] carried out experiments of the single phase heat transfer analysis on microtube using liquid nitrogen as working fluid. They observed that contrary to water in case of nitrogen heat transfer coefficient and local heat transfer coefficient both decreased in the flow direction with increase in heat flux, which they attributed to the inverse relationship between temperature and thermal conductivity of nitrogen. They concluded that thermal properties of working fluid play an important role on flow and heat transfer characteristics of microchannels. Herwig and Mahulikar [114] had proved importance of change in thermal properties of the working fluid on heat transfer characteristics through their numerical study. Sui et al. [115] carried out experiments using deionised water on three wavy microchannels test pieces (W, H) (205, 404) with different wavy magnitude (0, 138 and 259 μm). They compared the heat transfer performance of the wavy microchannels with straight microchannels and concluded that wavy microchannels had superior heat transfer performance than straight microchannels. The accredited it in favour of secondary flow inside curves of wavy microchannels.

It is widely accepted that the saturation flow boiling in microchannels is governed by nucleate boiling and forced convection boiling (Collier and Thome [116]). The nucleate boiling region is normally associated with the bubbly and slug flow pattern, and the forced convection boiling region is associated with the annular flow pattern. In the nucleate boiling region, the wall temperature is few degree higher than the saturation temperature of the working fluid, which is sufficient for the bubble nucleation and its growth. In this region the heat transfer coefficient is primarily influenced by the heat flux, whereas the effect of mass flux and vapor quality is less significant. In forced convection region, heat is mainly transferred through the single phase annular liquid film and is carried away by the evaporation at an interface of liquid and vapour. In this region heat transfer coefficient mainly depends on mass velocity, vapours quality and heat flux. Peng and Wang [33] observed that flow boiling was reached to the fully developed nucleate boiling for wall temperature slightly higher than saturation temperature and was not affected by liquid velocity and subcooling.

Two phase heat transfer coefficient along the length of the microchannel was measured by Lee and Mudawar [69]. In their experiment, the quality of vapour was maintained by changing the mass flow rate of R134a. They suggested dividing the quality region into smaller interval for better estimate of heat transfer coefficient. They proposed three regions, $x_e < 0.05$ for nucleate boiling generated at low heat flux, $0.05 < x_e < 0.55$ for annular film evaporation generated at high heat flux and high mass flux and $x_e > 0.55$ for annular film evaporation generated at high heat flux and low mass flux. Whereas, Yen et al. [117] claimed through their experiments that nucleate boiling region remained dominate up to $x_e < 0.4$ in case of HCFC123 followed by convective boiling region. From the above discussion it can be concluded that vapor quality limit which determines the dominance of either nucleate boiling or convective boiling is dependent on individual fluid.

Kosar et al. [41] monitored variation of the two phase heat transfer coefficient with heat flux and mass flux. They observed that at low (G = 41 kg/m^{2}s) and moderate (G = 83 and 166 kg/m^{2}s) mass fluxes, two phase heat transfer coefficient dropped rapidly after critical heat flux condition due to complete dryout. However, at higher mass flux (G = 302 kg/m^{2}s), two phase heat transfer coefficient decreased continuously from nucleate boiling to critical heat flux condition. They also observed large fluctuations in two phase heat transfer coefficient at low mass flux with exit vapor quality. They attributed it to the oscillatory flow pattern. Oscillatory flow pattern continuously shifted between confined bubble moving back and forth along the channel. Eventually, they concluded that nucleate boiling is dominant at low mass flux under all heat fluxes and moderate mass fluxes under low heat flux conditions. Whereas, for moderate mass fluxes under high heat flux and for high mass flux under all heat fluxes convective boiling is a dominant heat transfer mechanism. Schilder et al. [52] performed the experiments on circular glass tube (D_h = 600) using ethanol as working fluid. They observed that for single phase liquid flow, the measured Nusselt number approached the classical value for constant heat flux under Poiseuille flow (Nu = 4.36) at about 80% of the heated tube length. Based on two phase experiments they concluded that evaporation of thin liquid film covering the tube wall is dominating heat transfer mechanism. They further concluded that presence of wavy patterns on the film surface indicated the existence of shear force between the vapor and the liquid phase.

Steinke and Kandlikar [36] carried out flow boiling experiments on six rectangular microchannels with D_h = 207 μm using subcooled inlet conditions. They carried out experiments in heat flux range of 5 − 950 kW/m^2 and mass flux range of 157 − 1782 kg/m^{2}s. They found that local heat transfer coefficient value was very high at very low vapor quality ($x_e \approx 0$), which they attributed formation of first bubble (carting maximum energy) on that location. Local flow boiling heat transfer coefficient decreased very sharply with increase in vapor quality irrespective of heat flux value, this was accredited in favour of rapid bubble growth. Yen et al. [117], Sobierska et al. [45] Zhuan and Wang [118] and Kosar and Peles [119] also observed similar kind of trend in their studies as Steinke and Kandlikar [36]. Sobierska et al. [45] attributed the above to the following possible reasons; (i) partial dryout due to complete cross section filled by bubble, (ii) high pressure gradient associated with microchannels. Qu and Mudawar [34] also observed the same trend in their study and attributed it to appreciable droplet entrainment at the onset of annular flow regime. However, above reasons can not affect heat transfer characteristic in the vicinity of ONB, where vapor quality is very small. Retardation in local liquid phase velocity after ONB may be responsible for it. Park et al. [59] observed the same trend using FC – 72 but for low heat flux (q < 8.6 kW/m^2) region only, they attributed it to the insufficient heat flux for generating active boiling in microchannels. At high heat flux values (q > 8.6 kW/m^2), the local heat transfer coefficient first increases up to certain vapor quality and then decreased. They also observed decreasing trend of local heat transfer coefficient with increase in mass flux at constant heat flux value, which they attributed to the possible dry out of the liquid film surrounding the elongated bubble and annular flow.

Yun et al. [44] carried out experiments to study the effects of mass flux, heat flux and saturation pressure on heat transfer characteristics. They observed that effect of mass flux, heat flux and saturation pressure on heat transfer coefficient was more significant after dryout vapor quality. After dryout vapor quality region, heat transfer coefficient increased with increase in mass flux, heat flux and saturation pressure respectively.

The variation of heat transfer coefficient of HFE – 7100 with wall temperature and heat flux for different rectangular microchannels (W, H), (123.4, 304.9), (123.4, 526.9), (235.2, 576.8) and (259.9, 1041.3) was studied by Lee and Mudawar [108]. They concluded that smaller microchannel dimensions helped in improving the heat transfer characteristics by increasing mass velocity and wetted area. However, smaller width microchannels are more likely to face premature stability problems due to early transition from bubbly to slug flow. Balasubramanian et al. [54] compared the heat transfer coefficient in straight and expanding microchannel. They reported that heat transfer coefficient increased more rapidly with heat flux supplied in case of expanding microchannel as compared to straight microchannel. They attributed to it to the improved stability provided by expanding microchannel. Prajapati et al. [120] compared experimentally three different configurations (uniform cross-section, diverging cross-section and segmented fin microchannels) of microchannels. They observed that segmented fin microchannels perform better than uniform and diverging cross-section. This is attributed to the availability of more nucleation sites, breakage of thermal boundary layer, easy passage of bubbles or slug along main and secondary channel and minimum reverse flow. Law and Dhir [121] performed flow boiling experiments in straight-fin and oblique-fin microchannel using FC – 72 as working fluid. They observed improved thermal performance of the oblique-fin microchannel compared to the straight-fin microchannel and attributed to the stable flow boiling offered by oblique fin in terms of reduced wall temperature gradient and pressure fluctuation.

Study of Choo and Kim [122] was concentrated for finding the heat transfer characteristics of nonboiling two phase flow in microchannel. They observed the effect of microchannel hydraulic diameter on the heat transfer coefficient as shown in Fig. 2.9. When the channel diameter was smaller than about 235 − 260 µm, the two phase heat transfer was even lower than the single-phase case. They concluded that this may be due to the dominant effect of surface tension and liquid viscosity that prohibited the turbulent mixing in liquid film covering the wall. Furthermore, the transition channel diameter did not change once the gas Reynolds was increased beyond Re = 300. Experiments were performed with mixture of water and air on circular tubes of 140 µm to 506 µm diameter under different flow rates of air and water. Wang et al. [123] experimentally analyzed the effect of channel inclination (rectangular microchannel D_h = 825) by carried out experiments at different heat flux (25, 37.5) and mass flux values (100, 200, 300). Experiments were performed at five different inclinations – 90° (vertical downward), – 45°, 0°, 45° and 90° (vertical upward).

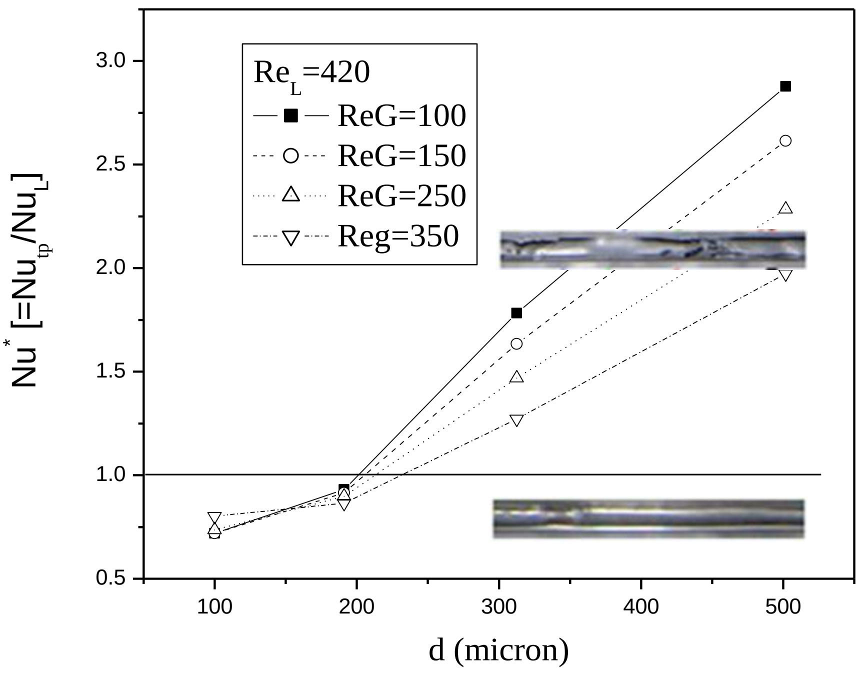

Figure 2.9 The variation of the Nusselt number with channel hydraulic diameter for different Reynolds number (Choo and Kim [122])

They observed that heat transfer coefficient increased by 30% at an inclination of 45° relative to horizontal orientation.They attributed the above to the two possible reasons (i) rise of distance between the bubble nose and contact surface brought the increase of velocity adjacent to the contact surface, (ii) concurrent nature of the inertia and buoyancy force. The heat transfer coefficient associated with vertical up (θ = 90°) and horizontal (θ = 0°) arrangements had almost same values due to the symmetric nature of the elongated bubble in both arrangements. For the vertical downward inclination heat transfer coefficient showed 50% lower value as compared to the inclination of 45° due to opposite direction of inertia and buoyancy forces.

Lu and Pan [58] observed significant enhancement in heat transfer coefficient in microchannels with artificial nucleation sites, which facilitated bubble nucleation. Yen et al. [117] observed high heat transfer coefficient in case of square microchannel as compared to circular microchannel up to vapor quality of 0.4. This was attributed to square corners that acted as host for active nucleation sites. They reported similar heat transfer at high vapor quality for both cases. However, the trend may be opposite at annular flow regime, surface tension force intends to attenuate liquid film (on the wall) more effectively in case of square cross section. Resulting local dryout in case of square channel will reduce its heat transfer performance in comparison to circular channel.

Few correlations to predict heat transfer coefficient in single phase and two phase flow are reported in open literature. Table 2.6 and 2.7 present details of these correlations for single phase and two phase respectively. These correlations for single phase and two phase heat transfer are plotted in Fig. 2.10 and Fig. 2.11, respectively against of experimental data of Koyuncuoglu et al. [126] for single phase and Qu and Mudawar [34] for two phase.

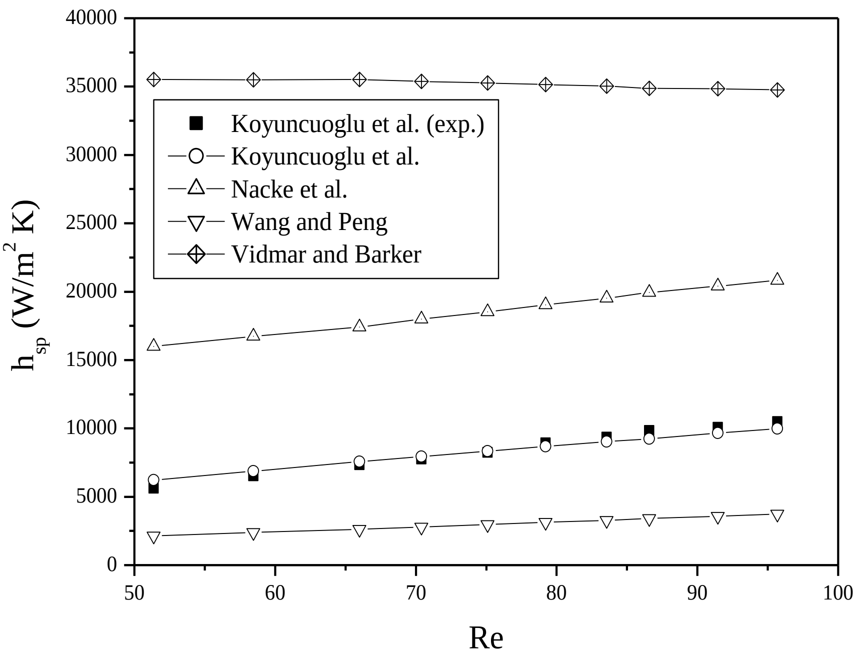

Figure 2.10 Single phase heat transfer coefficient variation with Reynolds number

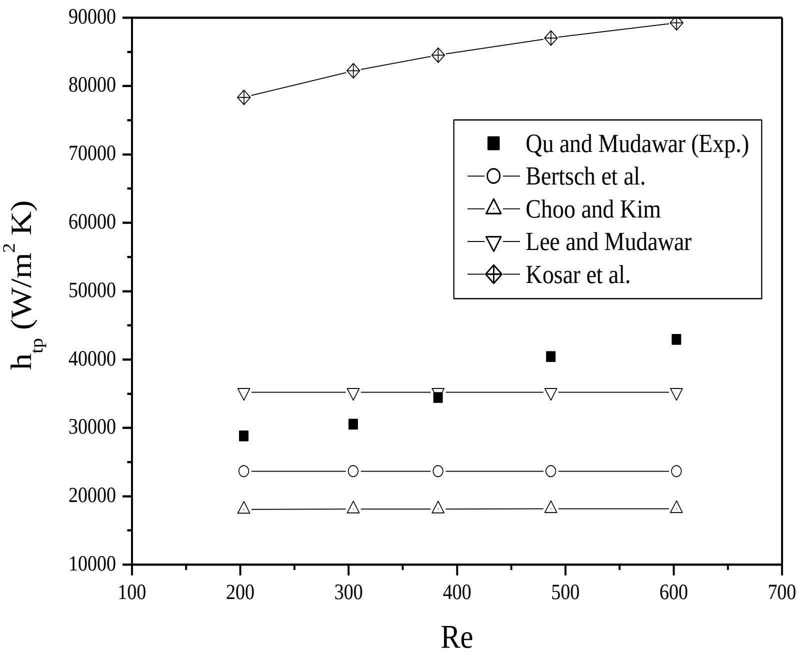

Figure 2.11 Two phase heat transfer coefficient variation with Reynolds number

Form Fig. 2.10 and Fig. 2.11, it can be concluded that existing heat transfer correlations are inconsistent and show large deviation in comparison to experimental data. This may be due to limited range of experimentation, difference in operating conditions, and difference in type of channel geometries used in these studies. Therefore, still lot of efforts are needed so that generalized equations can be found for finding out heat transfer coefficient associated with single phase and two phase flow in microchannels.

Table 2.6
Single phase heat transfer correlations

Author and year	Channels geometry and fluid (W, H, D) µm	Operating parameter	Correlation
Wang and Peng [113]	Rectangular, W = 200 to 800, H = 700 Water and methanol	P_{in} = 1 bar, $T_{in, w}$ = 10 to 35 ^{O}C, $T_{in, m}$=14 − 19 ^{O}C, Re = 1000 − 1500.	$Nu = \left[0.00805 Re^{4/5} Pr^{1/3}\right]$
Vidmar and Barker [124]	Circular, D = 131 Water	P_s = 500 to 4500 psi, T_{in} = 23.4 to 31.4 ^{O}C, T_{out} = 74 −163.1 ^{O}C, m = 1.510x10^{-3} to 4.43x10^{-3} kg/s.	$Nu = 4.36$, for Re<2300 $Nu = \left[\frac{(f/8)(Re-1000)Pr}{1+12.7(Pr^{2/3}-1)(f/8)^{1/2}}\right]$, for 2300<Re<20000 $Nu = \left[\frac{(f/8)Re\,Pr}{k_1+k_2(Pr^{2/3}-1)(f/8)^{1/2}}\right]$, for 10^4<Re<10^7 $k_1 = 1 + 13.6(f_D/4)$, $k_2 = 11.7 + 1.8/Pr^{0.33}$ $Re = \frac{\rho V D_h}{\mu}$, $Pr = \frac{\mu C_p}{k}$ $f = \begin{cases} 0.079 Re^{-0.25} & 4000 < Re < 20000 \\ 0.049 Re^{-0.25} & 20000 < Re < 10^6 \\ [1.581 \ln(Re) - 3.28]^{-2} & 10000 < Re < 10^7 \end{cases}$ $\frac{1}{f_D^{0.5}} = 1.14 - 2\,log_{10}\left(\frac{e}{D_h} + \frac{9.35}{Re f_D^{0.5}}\right)$
Nacke et al. [125]	Rectangular, W = 254 , H = 762 Water	T_{in} = 24.4, m = 0.001 to 0.0053 kg/s.	$Nu = 3.66 + \frac{0.0668\left(\frac{D_h}{L}\right)RePr}{1+0.04\left[\left(\frac{D_h}{L}\right)RePr\right]^{2/3}}$, for Re < 2300 and Pr ≥5 $Nu = 1.86\left(\frac{RePr}{L/D_h}\right)^{1/3}\left(\frac{\mu_l}{\mu_{l,s}}\right)^{0.14}$, for Re < 2300 and Pr < 5
Koyuncuoglu et al. [126]	Rectangular, W = 200 , H = 50, Water	T_{in} = 24.4 to 25.1 ^{O}C, T_{out} = 70.7 − 96.8 ^{O}C, m = 2.91x10^{-6} to 6.67 x10^{-6} kg/s.	$Nu = (W/H)^{-0.053}(Re)^{0.782}(Pr)^{0.041}$

Table 2.7
Two phase heat transfer coefficient correlations

Author	**Channel geometry and fluid (W, H, D) µm**	**Operating condition**	**Correlation**
Lee and Mudawar [69]	Rectangular, W = 231, H = 713 R134a	P_{in} = 1.44 − 6.6 bar, q = 159 − 938 kW/m^2, G = 127 − 654 kg/m^{2}s, x_{in} = 0.001 − 0.25, x_{out} = 0.49 − superheat	**For x_e=0 - 0.05,** $h_{tp} = 3.856X^{0.267}h_{sp,l}$, Where $X^2 = \frac{(dp/dz)_f}{(dp/dz)_g}$, $h_{sp,l} = Nu_3\frac{K_f}{D_h}$ $X_{vv} = \left(\frac{1-x_e}{x_e}\right)^{0.5}\left(\frac{\mu_f}{\mu_g}\right)^{0.5}\left(\frac{v_f}{v_g}\right)^{0.5}$ $X_{vt} = \left(\frac{f_f Re_g^{0.25}}{\mu_g}\right)^{0.5}\left(\frac{1-x_e}{x_e}\right)^{0.5}\left(\frac{v_f}{v_g}\right)^{0.5}$ $Nu_3 = 8.235\,(1-1.883\beta+3.767\beta^2-5.814\beta^3+5.361\beta^4-2\beta^5)$ **For x_e= 0.05 - 0.5** $h_{tp} = 436.48\,Bo^{0.522}We^{0.352}X^{0.665}h_{sp,l}$, Where $h_{sp,l} = Nu_3\frac{K_f}{D_h}$ **For x_e= 0.55 - 1** $h_{tp} = max\{108.6X^{1.667}h_{sp,g},\ h_{sp,g}\}$ $h_{sp,g} = Nu_3\frac{K_g}{d_h}$ for laminar flow $h_{sp,g} = 0.023Re_g^{0.8}Pr_g^{0.4}$ for turbulent flow
Kosar et al. [41]	Rectangular, W = 200, H = 264, L = 10 mm Water	q = 280 − 4450 kW/m^2, G = 41 − 302 kg/m^{2}s	$h_{tp} = 1.068(q")^{0.64}$ Nucleate boiling, $h_{tp} = 4.068\times10^4(Re_l)^{0.12}(1-x_e)^{0.8}\left(\frac{1-x_e}{x_e}\right)^{0.02}$ Convective boiling

Table 2.7 continued

Bertsch et al. [127]	D_h = 160 to 2920	T_{sat} = −194 to 90 ^{O}C, q = 4 − 1150 kW/m^2, G = 20 to 3000 kg/m^{2}s	$h = h_{nb}(1-x_e) + h_{cb}(1 + 80\ ({x_e}^2 - {x_e}^6)e^{-0.6\ Co})$ $h_{nb} = 55\ {P_r}^{(0.12-0.2(log_{10}R_p)}(-\ log_{10}\ \mathrm{P_r})^{-0.55}M^{-0.5}q''^{0.67}$ $h_{cb} = h_{conv,l}(1-x_e) + h_{conv,v}x_e,$ $h_{conv,L} = \left(3.66 + \frac{0.0668D_h/LRe_lPr_l}{1+0.04[D_h/LRe_lPr_l]^{2/3}}\right)\frac{k_l}{D_h}$ $h_{conv,v} = \left(3.66 + \frac{0.0668D_h/LRe_vPr_v}{1+0.04[D_h/LRe_vPr_v]^{2/3}}\right)\frac{k_v}{D_h},$ P_r=Inlet pressure/ critical pressure= Reduced Pressure, $Co = \left[\frac{\sigma}{g(\rho_l-\rho_v)D_h^2}\right]^{0.5}$, $Re_l = \frac{GD_h}{\mu_l},\ Re_v = \frac{GD_h}{\mu_v}\ ,\ Pr_l = \frac{C_{p,l}\mu_l}{k_l},\ Pr_v = \frac{C_{p,v}\mu_v}{k_v}$
Choo and Kim [122]	Circular, D_h = 140 − 506, Water and air	q = 340 − 950 kW/m^2, V_g = 1.24 − 40.1 m/s, V_l = 0.57 − 2.13 m/s,	$Nu_{tp} = 0.023Re_L^m Pr_L^{0.4}F,\ F = CX^{-n},\ m = 0.8 - 0.8\left[1 + e^{(d^*-37)/7}\right]^{-1},$ $C = 2.94 + 358\ e^{-0.1d^*},\ n = 0.7 - 0.8\left[1 + e^{(d^*-41)/2}\right]^{-1},\ d^* = d/\sqrt{\sigma/\rho g}$

2.5 Instability

Instability is also called as malfunctioning of the flow in microchannels. Instability in microchannel may cause several problems such as vibration, problems of system control, thermal fatigue and in extreme circumstances it may even be responsible for surface burnout. The well known instabilities associated with microchannels are flow reversal, pressure fluctuation, wall temperature fluctuation, flow maldistribution and Ledinegg instability. Out of above mention instabilities Ledinegg instability is static instability, whereas pressure fluctuation, wall temperature fluctuation and flow reversal are dynamic instabilities. A thorough understanding and determination of these associated instabilities are important.

Qi et al. [128] carried out experiments in order to study the two phase flow instabilities using liquid nitrogen as working fluid on two microtubes of diameter 1.042 and 1.931 mm. They observed repetitive regular oscillation of mass flux, pressure drop and wall temperature at ONB in both microtubes. These oscillations were referred as stable oscillation, as it remained stable, if system pressure, heat flux and outlet condition of the system did not change significantly. They explained that after ONB, many small bubbles nucleate, grow, detach from nucleation cavities and finally move along the flow in microtube. These small vapor bubbles entered and accumulated gradually into the outlet mixing chamber having diameter much larger than microtube that ultimately reduces bubble velocity. Hence, inertia force turned weaker and gravitational force magnitude increased significantly. Due to low vapor density these bubbles accumulated in upper part of outlet mixing chamber and formed vapor patch. This vapor patch temporarily blocked the mouth of outlet port. Thus, mass flux gradually decreased, which eventually resulted into increase in wall temperature and two phase vapor quality due to continual supply of heat flux. Higher exit vapor quality increased associated pressure drop. After discharge of the vapor patch, microchannel was again filled with fresh liquid nitrogen and the process repeated itself. Huh et al. [46] observed similar kind of oscillations in their study. They further concluded that pressure drop fluctuation and mass flux fluctuation remained in phase. Whereas, mass flux fluctuation and wall temperature fluctuation were exactly out of phase. They also observed that fluctuation period and fluctuation amplitude decreased with increase in mass flux and decrease in heat flux. Qu and Mudawar [109] carried out experiments on multiple parallel microchannels. They reported two types of instabilities, pressure drop oscillation and parallel channel instability associated with microchannels. Pressure drop oscillation produced fairly large periodic amplitude flow oscillation, which arose due to interaction between generated vapor and compressible volume coming from upstream direction. Whereas, parallel channels instability produced very mild flow oscillations resulting from density wave oscillation within each channels. They further reported that severe pressure drop can even lead to premature critical heat flux condition. Chang and Pan [129] concluded that large magnitude of the pressure drop oscillation may result into growing and shrinking of the bubble slug alternatively with flow reversal. Bogojevic et al. [130] carried out series of experiments on 40 parallel microchannels (D_h = 194) using water as working fluid. They observed that low inlet water temperature was subjected to higher magnitude of temperature oscillation. Whereas, high inlet water temperature promoted better flow distribution, which resulted into lower magnitude of temperature oscillation. Megahed [55] observed that microchannels were subjected to low magnitude of pressure and temperature fluctuation at high mass flux. Therefore, he concluded that flow becomes more stable at high mass flux. Balasubramanian et al. [54] observed that pressure fluctuation and wall temperature fluctuation were less severe in expanding microchannel than the straight microchannel under same operating conditions.

Flow reversal is another potential instability reported by several authors in which vapor slug flows back into inlet plenum. Qu and Mudawar [35] and Bergles and Kandlikar [131] observed that flow reversal occurs generally when CHF condition was approached. In the vicinity of CHF, rapid evaporation of the liquid caused bubble to expand in both upstream and downstream directions and form vapor slug. Kandlikar [132] concluded that location of the ONB decides the flow reversal. When nucleation occurred towards microchannel outlet (Fig. 2.12 (a)), no flow reversal was observed. This was due to the fact that vapor pressure of liquid could not overcome inertia of incoming fluid. On the other hand, when nucleation was initiated near microchannel inlet, vapor bubble could easily overcome lower inertia of the incoming fluid. Thus, flow reversal was observed as shown in Fig. 2.12 (b). Recently, Tuo and Hrnjak [133] studied the effect of the flow reversal on the performance of microchannel based evaporator of vapor compression system and concluded that it causes refrigerant flow maldistribution. They also concluded that local heat transfer coefficient may reduce because the vapor re-entrainment is likely to form a "dryout" bubble slug (without being surrounded by a thin liquid film). Kandlikar [132] mentioned that flow reversal could be avoided either by reducing the local liquid superheating at the ONB or by introducing pressure drop element at the entrance of each channel. Kaun and Kandlikar [134] performed experiments with inlet restrictors and observed that the flow become stable and flow reversal problem was reduced due to application of restrictors. Wang et al. [48] had also confirmed that the inlet restrictor helps in reducing flow reversal instability. Kuo and Peles [135] observed that the presence of reentrant cavities helped in reducing the pressure drop oscillation, parallel channel instability and flow reversal instability by acting as host for active nucleation sites at much lower heat flux.

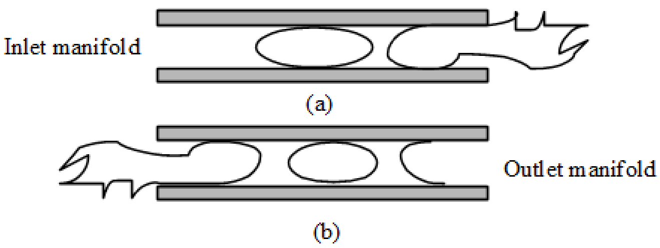

Figure 2.12 Effect of nucleation location ((a) towards outlet, (b) towards inlet) on flow reversal (Kandlikar [132])

Xu et al. [136] and Liu et al. [137] experimentally demonstrated seed bubble generation method to mitigate flow instabilities (flow reversal, pressure drop oscillation and temperatures oscillation) associated with microchannels, which arises mainly due to strong thermal non equilibrium of liquid and vapor phase. Originally this idea was proposed by Thome and Dupont [138]. Seed bubbles are micron size bubble, generated on the set of microheaters, which were installed near to inlet port at the top wall of microchannels. These microheaters were driven by pulse voltage signal. When the voltage signal was on during pulse cycle, heating of microheaters generates seed bubble, Marangoni effect help in sticking of these seed bubbles at microheaters. As the signal turned off in the same pulse cycle, Marangoni effect become weak and shear force from the flowing liquid took away seed bubbles from microheaters surface. These seed bubble grow further soaking up energy from superheated liquid. At low frequency, these seed bubbles not only decreased oscillation amplitudes of pressure drop and temperature but also reduced oscillation cycle periods. At high frequency, these seed bubbles completely suppressed the flow instabilities. However, this method had not facilitated the subcooled liquid flow and vapor flow at high vapor mass quantities. Han and Shikazono [139] demonstrated air injection as a stabilization method for flow boiling in microtube using water as working fluid. They observed that pressure fluctuation and wall temperature fluctuation reduced significantly with increase in air injection flow rate.

Recently, Tuo and Hrnjak [140] proposed new vapor venting method to mitigate problem associated with flow reversal in microchannel evaporator. Proposed method provides 5% increase in cooling capacity and 3% increase in COP of air conditioning system.

In case of two phase flow in parallel microchannel heat sink, equal mass flow distribution to each microchannel is very important. In absence of properly design inlet/outlet header, microchannel heat sink is bound to face large amplitude fluctuation of pressure and temperature due to backward flow which eventually decrease the cooling capacity of heat sink and has to be obliged by running the system at moderate load. The headers which connect all microchannels in case multiple microchannel heat sink unavoidably introduce additional pressure drop due to contraction/expansion, friction and pressure loss/gain due to deceleration/acceleration [141]. This causes uneven pressure difference across each tube, resulting in unequal mass flow through each microchannel. Researchers have also suggested modification in of inlet/outlet header for removing flow maldistribution problem. Tonomura et al. [142] carried out CFD simulation to find optimum design of manifold for parallel microchannel heat sink. They observed that large outlet manifold provide uniform flow distribution. However, enlargement of outlet manifold is increased dead volume inside microchannels. They also generated optimal shape header automatically (somewhat like trapezoidal header) by integration of optimization method with CFD simulation. Cho et al. [143] performed experiments on 33 straight and 33 diverging microchannels having rectangular as well as trapezoidal header. They observed that diverging microchannels with trapezoidal header gave more uniform flow distribution as compared to other configurations such as straight microchannel-rectangular header, straight microchannel-trapezoidal header and diverging microchannel-rectangular header. Cho et al. [144] carried out numerical simulation to obtained optimal header geometry which somewhat like trapezoidal in shape for two phase flow in the microchannel heat sink. Kumaraguruparan et al. [145] carried out numerical study on microchannel heat sink to investigate the causes of flow mal-distribution. They observed that flow field in inlet header was non uniform due to occurrence of circulation zone at inlet of some channels which resulted into flow mal-distribution. Numerical results also showed that smaller width or depth or larger channel length turn flow distribution more uniform. Furthermore, flow mal-distribution problem aggravated at high flow rate or by the use of less viscous fluid. Tuo and Hrnjak [146] in their experimental study on microchannel evaporator (34 tubes) identified two types of fluid mal-distribution:

quality induced mal-distribution and header pressure drop induced mal-distribution. They used flash gas bypass method to mitigate problem of the quality induced mal-distribution. They also observed that increase in outer header diameter resulted into uniform flow rate in each microctube. Szczukiewicz et al. [147] concluded through their visual observation on sixty seven rectangular microchannels (100, 100) evaporator that introduction of the inlet orifice successfully suppressed flow instability, vapor back flow and significantly improved flow uniformity across microchannel.

Study of Ledinegg instability is helpful to avoid malfunctioning of the pump used in microchannels heat sink loop. As per Kakac and Bon [148], Ledinegg instability is due to sudden variation in flow rate to a lower value.

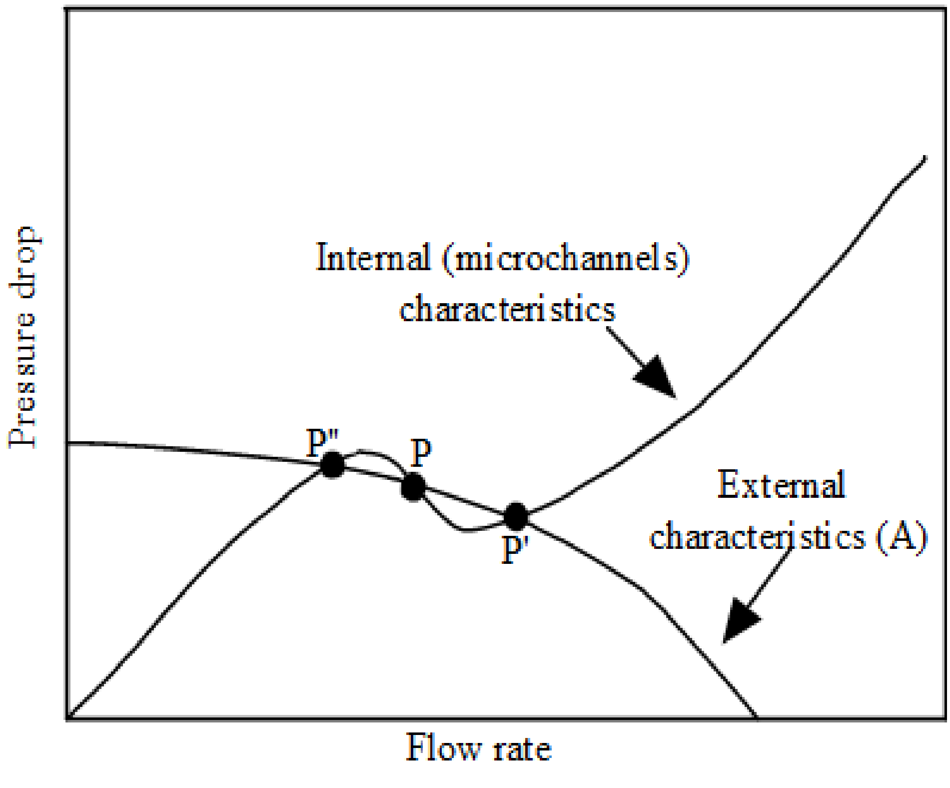

Figure 2.13 Ledinegg instability (Kakac and Bon [148])

It is explained through pressure drop verses mass flow rate characteristics reported by Kakac and Bon [148] in the Fig. 2.13. It occurred when slope of the channels demand curve (internal characteristics curve) is negative and steeper than the loop supply curve (external characteristics curve, A) and under multiple interaction of this both curves (*P, P', P''*). A slight variation in flow rate to the lower side result in more pressure drop is required to sustain the flow available from external curve. Zhang et al. [149] studied Ledinegg instability in microchannels and proposed ways to avoid this instability as having less number of channels, increased system pressure, lower heat flux, low sub cooling and short channels.

2.6 Critical heat flux

Boiling phenomenon in microchannel is associated with dissipation of large heat flux as long as heat transfer surfaces remain wetted with a fluid. Loss of contact between liquid and heat transfer surface results into sudden dramatic decrease in efficiency of heat transfer. This condition is termed as critical heat flux (CHF), which causes localized overheating of the heated surface. CHF condition is categorized as subcooled CHF and saturated CHF [150]. In the subcooled CHF, bubbles nucleated at heated surface coalesce and form a localized vapor blanket having inherent tendency of poor heat transfer rate due to low thermal conductivity of vapor phase. In the saturated CHF, evaporation of the thin liquid film trapped between vapor core and channel wall occurs, which causes direct exposure of surface to the vapor. Researchers have suggested different hypotheses for the occurrence of CHF under subcooled conditions. Kutateladze and Leontev [151] proposed that subcooled CHF occurs on account of intense boiling, which causes separation between heated surface and the bubble-liquid boundary layer and evaporation of resulting stagnant liquid. Another hypothesis accredits the accumulation of tinny vapor bubbles within liquid boundary layer, which inhibits direct contact between liquid and heated surface. Limited enthalpy transport between the bubbly layer and liquid leads to subcooled CHF condition [152]. Similarly, as per another hypothesis for subcooled CHF on vertical surface, vapor blankets (formed from small bubbles piling on heated surface) formed on heat transfer surface prevents the liquid from entering the bubbly sublayer from the sides of the blanket and CHF tends to occur when the amount of liquid entering the sublayer is less than the amount of liquid evaporated [153].

In summary, it is known that nucleation associated vapor blanketing of the heating-surface is the CHF mechanism for sub-cooled or saturated pool-boiling. CHF mechanisms and values for flow boiling in larger diameter ducts can depend on orientation with respect to gravity vector, method of heating/cooling (e.g. uniform or non-uniform temperature or heat-flux controlled heating of the in-tube boiling), whether or not inlet vapor flow rate is substantially different from zero [154], etc. Despite the possibility of CHF values dependence on the "method of heating," it is common practice to assume uniform heat-flux method of heating based characterization of CHF values to be most conservative.

Despite the aforementioned complexities, in broad terms, CHF has one of the following two mechanisms. (i) At small mass-fluxes and low quality (for cases where inlet quality is effectively zero in terms of vapor flow rate), it is typically due to vapor blanketing (of the heating-surface) as departure from nucleate boiling (DNB, associated with vigorous nucleation and coalescence of bubbles) is reached at rates that do not allow the possibility of subsequent attainment of steady plug/slug flow regimes. (ii) At high mass-fluxes and high vapor quality (typically if the flow achieves annular regime prior to dryout or, as in [154], the flow is annular right from the inlet), it is due to dryout instabilities associated with thin film boiling. For moderate mass-fluxes and qualities, one could have either of the two mechanisms [155]. This is likely due to the fact that the transition between these two mechanisms is influenced by other non-dimensional parameters (besides non-dimensional mass-flux and quality) and this transition has not yet been characterized.

At present, in the absence of availability of flow visualization for all the data reported in literature, mechanism classification in the above two broad categories is dependent on whether or not similar fluids in similar experiments (involving variations in inlet quality and non-dimensional mass-flux) fit a certain trend in CHF correlations.

For micro-channels, only the first of the two above stated mechanisms change slightly. This mechanism (for low inlet mass-flux and zero/low inlet quality) changes to bubbles clogging the entire micro-channel and not just the heating-surface and this can happen at lower CHF values than those for the larger diameter cases. For moderate to high mass-fluxes, the dryout CHF mechanism possibility remains the same as for the larger hydraulic diameter cases.

Qu and Mudawar [35] carried out experimental CHF study on twenty one parallel rectangular microchannels of cross section (215μm x 821μm). They concluded that flow reversal in microchannel may force early (near inlet) occurrence of CHF and observed that parallel channel instability (ascribing it to mild flow fluctuation occurring due to density wave oscillation of neighboring channels) becomes more severe once CHF condition is reached. Qi et al. [156] in their experimental study on circular microtubes of diameter (531, 834, 1042, 1931μm) observed that CHF occurred towards the exit end of microtubes. Importantly, they did not observe CHF caused due to flow reversal and attributed it to the longer length (and, possibly, larger pressure-gradients) of their microtubes. Wojtan et al. [157] observed that the magnitude of CHF increased with increase in internal diameter of microchannel tube and mass flux. They observed that CHF value decreased with increase in channel length. Bergles and Kandlikar [131] concluded that non uniform distribution of the circumferential heat flow in a specific microchannel introduces non uniform CHF condition in neighboring microchannels. Researchers have also investigated methods for improving/increasing the CHF value for a given set of operating conditions. Introduction of reentrant cavities [135, 41], provision of artificial nucleation site [132] and use of expanding microchannels [158] are the techniques reported in open literature for avoiding/delaying occurrence of CHF conditions.

Critical heat flux value is an important design parameter, which in spite of its negative influence, has attracted a lot of attention. Accurate prediction of CHF is important especially for heat controlled systems as it can cause disastrous failure of the systems. Its study is also important as it sets a maximum limit of performance of heat transfer system. In 1978, Katto [159] first time derived CHF correlation for circular tube following non-dimensional analysis. The CHF correlation proposed by Katto [159] is given by Eq. (2.2).

$$q_{CHF} = \left(Gh_{fg}\right) a' \left(\frac{\rho_v}{\rho_l}\right)^{b'} \left(\frac{1}{We}\right)^{c'} \left(1 \Big/ \left(d' + e' \left(\frac{\rho_l}{\rho_v}\right)^{f'} \left(We\right)^{h'} \left(\frac{l}{d_h}\right)^{i'} \right) \right) (AR)^{j'} \tag{2.2}$$

Where, *a'*, *b'*, *c'*, *d'*, *e'*, *f'*, *h'*, *i'* and *j'* are constants that depend on thermo-physical properties of working fluid and can be determined through experimental data. Several authors have proposed CHF correlation for microchannel following Kotto's work. Table 2.8 presents the summary of these correlations [35, 41, 112, 156, 157, 160, 161] and details of other CHF experimental studies [41, 162, 163, 164, 165, 166, 167, 168, 169, 170] associated with microchannel. Kandlikar [98] discussed effect of forces: surface tension (F_{sf}), evaporation momentum change (F_m), inertia (F_i) and gravity (F_g) on flow boiling in microchannel and showed that CHF condition during flow boiling in microchannel can be correlated in terms of two non-dimensional numbers given by $\left(K_1 = F_m/F_i\right)^{0.75} \times \left(K_2 = F_m/F_{sf}\right)$. Researchers had also attempted to develop mechanistic models for CHF condition in microchannel. Kuan and Kandlikar [171] developed CHF model for flow boiling in microchannel. They considered inertia, surface tension and evaporation momentum forces acting on the vapor bubble in their model and revealed that ratio of evaporation momentum to surface tension force is an important parameter influencing CHF condition in microchannel. Kandlikar [100] refined earlier work of [171] by introducing additional effect of shear force on vapor bubble.

They developed CHF expression in terms of non-dimensional numbers: Weber number, Capillary number and $K_2 = F_m / F_{sf}$. Eventually, they proposed generalized solution (including refrigerants and water) for CHF during flow boiling in microchannel following regression method. Both correlations are reported in Table 2.8.

Revellin and Thome [172] formulated theoretical model for prediction of saturated CHF condition for fluid boiling under stable conditions in circular microchannel. Basic transport equations along with Laplace-Young equation and semi-empirical expression for height of interfacial waves had been used to replicate evaporation of the thin liquid film in annular flow region just before CHF condition. Model showed very good agreement (96 % data within ±20 % error band) for refrigerants. Revellin et al. [173] modified CHF model of [172] to account for non-uniform axial heat conditions (generated due to presence of multiple hot spots) along the microchannel. They recommended many useful suggestions for dissipating heat flux of hot spots in better manner i.e. high mass flux, small size, and number of hot spots, large distance between two hot spots and low saturation temperature.

Table 2.8

Summary of CHF studies on microchannel

Author	**Working fluid**	**Geometry and dimension**	**Operating conditions**	**Correlation developed**	**Constants**								
		(*W*, *H*) *D*µm	***T* (^{O}C), *P*(bar), *G*(kg/m^{2}s)**		***a'***	***b'***	***c'***	***d'***	***e'***	***f'***	***h'***	***i'***	***j'***
Qu and Mudawar [35]	Water	Rectangular, 215, 821	T_{in} = 30 and 60, P_{out} = 1.13, G = 86–368	yes	33.43	1.11	0.21	0	1	0	0	0.36	0
Qi et al. [156]	Liquid nitrogen	Circular, 531, 834, 1042, 1931	T_{in} = 78.2 – 79.8, P_{out} = 1.4 – 5.8, G = 440 – 3000	yes	0.214+0.14*Co*	0.133	0.333	1	0.03	0	0	1	0
Wojtan et al. [157]	R134a	Circular, 500 800	T_{sub} = 2 – 15,T_{sat}= 30, 35, G = 400 –1600	yes	0.437	0.073	0.24	0	1	0	0	0.72	0
Kosar et al. [41]	Water	Rectangular, 200, 264	T_{in}= 22,P_{out} = 1.01, G = 41 – 302,	yes	0.0035	0	0.12	0	1	0	0	0	0

Table 2.8 continued

Miner [158]	R134a	Expanding rectangular, W_{in} = 138 – 154.1, W_{out} = 137.3 – 148.5, H_{in} = 528.5 – 626.5, H_{out} = 586.1 – 1046.1	T_{in} = 3.3 – 6.7, P_{in} = 3.4 – 4.17, G = 483 – 1500	no	-	-	-	-	-	-	-	-	-
Bowers and Mudawar [112]	R113	Circular, 510, 2540	T_{sub} = 10 –32, P_{in} = 1.38, G = 31 – 480	yes	0.16	0	0.19	0	1	0	0	0.54	0
Ong and Thome [160]	R134a, R236fa, R245fa	Circular, 1030, 2200, 3040	T_{sub} = 5 – 24, T_{sat} = 25 – 35, G = 100 – 1500	yes	0.12 $(\mu_l/\mu_v)^{0.183}(d_h/D_{th})^{0.11}$	0.062	0.141	0	1	0	0	0.7	0
Fu et al. [161]	HFE7100	Diverging rectangular, W_{in} = 300 – 870, W_{out} = 680 – 1590, H = 300 – 4000	T_{sub} = 44, 64, T_{sat} = 61, G = 39 – 180	yes	0.112	0	0.17	0	1	0	0	0.86	0.3

Table 2.8 continued

Kosar and Peles [162]	R123	Rectangular, 200, 264	T_{in} = 22, P_{out} = 2.27 – 5.2, G = 291 – 1118	yes	-	-	-	-	-	-	-	-	-
Kuan [163]	R123	Rectangular, 1057, 157	T_{in} = 17.2 , P_{out} = 2.1 – 2.358, G = 377.3 – 485.2	yes	-	-	-	-	-	-	-	-	-
	Water		T_{in} = 25.4 , P_{out} = 1, G = 50.4 – 231.7										
Agostini et al.[164]	R236fa	Rectangular, 223, 680	T_{sub} = 0.4 – 15.3, $T_{in,sat}$ = 20.31 – 34.27, $T_{out,sat}$ = 23.4 – 36.4, G= 276 – 992	no	-	-	-	-	-	-	-	-	-
Park [165]	R134a, R236fa, R245fa	Rectangular, 467, 4052 199, 756	T_{sub} = -1.1 – 24.0, T_{sat} = 0 – 45, G = 84– 3736.1	no	-	-	-	-	-	-	-	-	-
Mauro et al. [166]	R134a, R236fa, R245fa	Rectangular, 199, 756	T_{sub} = 5 – 25, T_{sat} = 20 – 50, G = 248 – 1500	no									
Basu [167]	R134a	Circular, 500, 960, 1600	T_{sub} = 5 – 40, P_{out} = 4.9 – 11.6, G = 300 – 1500	no	-	-	-	-	-	-	-	-	-

Table 2.8 continued

Roday [168]	Water	Circular, 286, 427,700	T_{sub} = 2.2 – 80.3, P_{out} = 0.253 – 1.79, G = 315 – 1570	no	-	-	-	-	-	-	-	-	-
Hsieh and Lin [169]	Water	Rectangular, 200, 100	T_{in} = 15, P_{out} = 1, G = 820 – 1600	no	-	-	-	-	-	-	-	-	-
Roach et al. [170]	Water	Circular, 1131, 1168	T_{in} = 48.9 – 71.1, P_{out} = 3.44 – 10.43, G = 250 – 1037	no	-	-	-	-	-	-	-	-	-

Models not based on Katto's correlation

Kosar and Peles [162]	$q''_{CHF} = Gh_{fg}\left\{\left(9.34\times10^{-2}\dfrac{P_e}{P_{cr}} - 0.34\left(\dfrac{P_e}{P_{cr}}\right)^2 - 1.3\times10^{-4}\right)x^{0.59}\right\}^{1/1.08}$	-
Kuan and Kandlikar [171]	$q''_{CHF} = Ch_{fg}\sqrt{\rho_g}\sqrt{\dfrac{2\sigma\cos\beta}{H} + \dfrac{G^2}{2\vec{\rho}}}$	C = 0.002492 Water = 0.003139 R123 = 0.002679 Common

Table 2.8 continue

Kandlikar [100]	$K_{2,CHF} = a_1\left(1+\cos\theta\right) + a_2We\left(1-x\right) + a_3Ca\left(1-x\right)$	$We < 900$, $L/D \le 140$
	$K_{2,CHF} = a_4\left[a_1\left(1+\cos\theta\right) + a_2We\left(1-x\right) + a_3Ca\left(1-x\right)\right]$	$We < 900$, $L/D \ge 230$
	$K_{2,CHF} = a_1\left(1+\cos\theta\right) + a_2We\left(1-x\right) + a_3Ca\left(1-x\right)$	$We \ge 900$, $L/D \le 60$
	$K_{2,CHF} = a_5\left(\frac{1}{WeCa}\right)^n\left[a_1\left(1+\cos\theta\right) + a_2We\left(1-x\right) + a_3Ca\left(1-x\right)\right]$	$We \ge 900$, $L/D \ge 100$
	$a_1 = 1.03 \text{ X } 10^{-4}$, $a_2 = 5.78 \text{ X } 10^{-5}$, $a_3 = 0.783$, $a_4 = 0.125$, $a_5 = 0.14$, $n = 0.07$	

Footnote: $D_{th} = 1/Co\,(\sigma/g(\rho_l-\rho_v))^{0.5}$, $Co=0.5$.

2.7 Summary

From the literature considered in this chapter, following remarks have been observed which are helpful in deciding the objectives for the current work.

i. Flow visualization study is very important as it gives an insight of the heat transfer and the pressure drop characteristics. Lot of flow visualization studies have been carried out on microchannels. However, unlike conventional channels, flow regimes are not well accepted yet for microchannels. Phenomena like bubble suppression, bubble circulation, bubble nucleation inside thin liquid film, bubble condensation, and their effect on flow regimes are not well studied yet. Hence, unusual states such as absence of bubbly flow, swirling pattern in churn flow and liquid bridges in slug–annular flow have been reported in different research works.

ii. Majority of the microchannel research work in the last two decades had been oriented for better understanding of mechanism involved in heat transfer. Current heat transfer correlations comparative study shows that still lot of efforts are needed for setting up generalized heat transfer correlations for microchannels. Limited range of experimentation, difference in operating conditions, and channel geometries could be possibly responsible for that. Future research will certainly focus more on finding suitable heat transfer augmentation techniques by choosing among from conventionally proven methods e.g. extended surfaces, artificial nucleation sites, surfactants, artificial surface roughness, nanofluid etc.

iii. Various instabilities associated with two phase flow are the main constraints limiting the application of microchannels. Few suggestions have been made in order to avoid instabilities such as flow reversal (reducing liquid superheating at ONB, throttling at inlet of microchannels and re-entrant cavities), Pressure and temperature oscillations (operating at high mass fluxes, and expanding microchannels) and Ledinegg instability (increased system pressure, lower heat flux, low sub cooling and short channels). More studies are needed in this direction such as novel design can be devised free from major instabilities.

iv. Majority of the studies have been carried out on rectangular microchannels or microtubes. Very few studies have been carried out on other cross sections like trapezoidal, V-shape, hexagonal, open microchannel heat sink etc. It would be interesting to know, what is the effect of channel geometry on heat transfer characteristics and especially on instabilities? Moreover, refrigerant like R600a and R290 (with low ozone layer depletion potential) have not been explored as working fluid in microchannels.

v. The bubble dynamics (i.e. such as vapor bubble nucleation, growth, departure from nucleation site and its motion along the flow) governs the two phase heat transfer, pressure drop characteristics and possibly associated instabilities also. Use of conventional channel theory is ambiguous for this task. Detailed numerical study of each stage will be helpful in accurately predicting heat transfer and pressure drop characteristics under wide range of operating conditions.

2.8 Objectives of the current work

Use of the microchannel heat sinks become more popular due to is very good command over the high heat removal capacity. It also has several other advantages such as compact and light weight, low coolant inventory and uniform temperature distribution. Hence it is very important to understand the boiling phenomena in microchannel heat sinks. Based on the literature reviewed, following objectives are decided for current work.

i. Formation of the bubble at nucleation site is first stage of the boiling and has great influence on two phase heat transfer, pressure drop characteristics and possibly associated instabilities. Use of conventional channel theory is ambiguous for this task. Thus the first objective of the present research is to develop simplified model to predict bubble growth in microchannel. Development of the bubble growth model will help in giving more insight of the flow boiling phenomena in microchannel.
ii. Bubble growth at nucleation site is divided between inertia controlled region and thermal diffusion controlled region. From the open literature, it is observed that no effort has been made to distinguish between these two regions. Thus the second objective current work is to explore bubble growth model to differentiate inertia controlled region and thermal diffusion controlled region.
iii. From the literature it is observed that unlike the conventional channels, the CHF correlation for microchannels are limited and associated with significant errors. Hence, third objective of present study is to develop the CHF correlation for microchannel utilizing bubble growth model.
iv. Lot of studies have been reported in the literature on the performance enhancement of microchannel. However, no efforts have been made to performed experimentation on open microchannel heat sink with single phase flow. Hence, last objective of current work is to analyze performance of the open microchannel heat sink with single phase liquid flow and possibility to improve its performance.

CHAPTER 3

DEVELOPMENT OF ENERGY BASED BUBBLE GROWTH MODEL FOR MICROCHANNEL

3.1 Introduction

The bubble dynamics governs the thermal and hydraulic behavior of the flow inside the microchannel heat sink. Hence, it is more important to pay attention to understand the bubble dynamics in microchannel. Bubble dynamics in homogeneous superheated bulk medium is governed by the well-known Rayleigh equation and its extended form [174 – 176]. Fu and Pan [177] had developed an elegant numerical model for mixing process of sulfuric acid and sodium bicarbonate in microchannel utilizing modified Rayleigh equation. However, Rayleigh equation predicts larger bubble growth rate than experimental value for heterogeneous bubble growth in microchannels [38, 178]. This indicates that, there is a clear need to develop simplified model that can predict the bubble growth at nucleation site inside the microchannel. Considering this fact, attempt has been made to develop a simplified model to predict the bubble growth at nucleation site in microchannel.

3.2 Development of energy based bubble growth model

As soon as fluid neighboring the nucleation site acquires saturation temperature corresponding to nearby pressure, bubble nucleation starts. Bubble starts growing at the nucleation site and after some time bubble departs from it. Bubble diameter continuously increases from inception to departure as the time progresses. Figure 3.1 shows growing bubble at the nucleation site. Following assumptions are made in present model.

1. Nucleation site is assumed in form of an inverted cone shape.

2. The bubble appears in the form of truncated sphere at nucleation site with contact angle ($t = t_{FV} = 0;\ \theta_{incep} = 90°$).
3. Thermal properties do not change with time.
4. Bubble growth is not affected by the heat supplied in neighboring region.
5. Heat supplied at the nucleation site is divided between liquid phase and vapor phase as per instantaneous void fraction value.
6. Condensation on bubble surface is assumed to be negligible.
7. No heat losses occur between the test section and atmosphere.

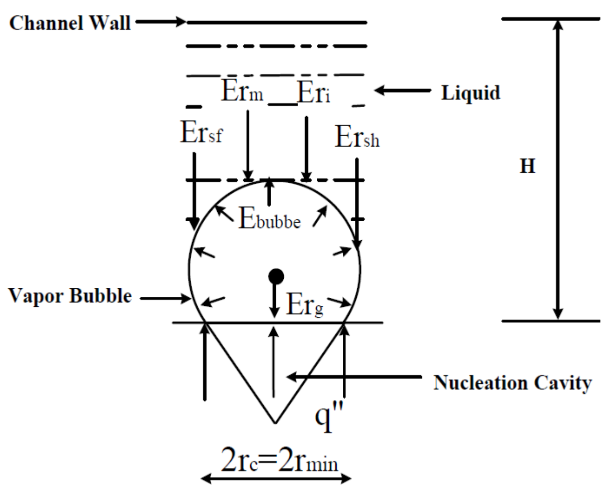

Figure 3.1 Energy distributions at nucleation cavity

As it is assumed that heat supplied at the nucleation site is divided between liquid phase and vapor phase as per instantaneous void fraction value. Thus, heat supplied at nucleation cavity can be given by Eq. (3.1).

$$\text{Heat supplied at the nucleation cavity} = q''(1-\varepsilon_i)A_c + q''\varepsilon_i A_c \qquad (3.1)$$

Where the first term represents heat carried away by the liquid phase and the second term indicates heat taken away by the vapor phase. Heat taken away by the vapor phase is utilized in bubble growth (E_{bubble}) and overcoming resistive effects due to surface tension (Er_{sf}), inertia (Er_i), drag (Er_{sh}), gravity (Er_g) and change in momentum due to evaporation effects (Er_m). Equation (3.2) shows the energy balance equation for the vapor phase.

$$q''\varepsilon_i \cdot A_c = E_{bubble} + Er_{sf} + Er_i + Er_{sh} + Er_g + Er_m \tag{3.2}$$

The void fraction is an important parameter associated with the two phase flow. It had been extensively used in empirical models for prediction of the flow pattern transition, heat transfer and pressure drop characteristics of microchannels. The void fraction can be specified in terms of various geometric definitions: local, chordal, cross-sectional and volumetric void fraction [179]. The cross-sectional void fraction is used in current study as given by Eq. (3.3).

$$\varepsilon_i = \frac{\text{Cross section of channel accupied by the vapor bubble}}{\text{Cross section of channel}} = \frac{A_{i,c/s}}{A_{ch}} \tag{3.3}$$

Experimentally the cross sectional void fraction can be measured either directly by optical method or by an indirect method such as through measurement of electrical capacitance of the conducting liquid phase [180].

3.2.1 Energy utilization in vapor bubble

In this section energy required for bubble growth and consumed in overcoming other resistive effects are discussed. Complete derivations of these resistive effects are given in Appendix A.1.

(a) Energy required for the bubble growth (E_{bubble}):

Evaporation is an endothermic phase change process in which significant amount of heat supplied to the vapor phase is consumed during bubble growth period. Due to evaporation at the interface, vapor is added into the bubble, thus bubble volume continuously increases at the nucleation site since inception until its departure. The energy required for evaporation at the liquid-vapor interface is given by Eq. (3.4).

$$E_{bubble} = \rho_v h_{fg} \frac{dV_i}{dt} \tag{3.4}$$

(b) Energy required to overcome the surface tension effect at interface (Er_{sf}):

Surface free energy at the interface continuously increases with time due to increase in surface area of the bubble during growth period. Surface tension can be expressed in terms of the Gibb's energy and surface area utilizing Eq. (3.5) [181, 182].

$$\sigma = \frac{dG}{dA_{i,s}} \tag{3.5}$$

Rearranging Eq. (3.5) gives the surface energy required to maintain the interface. It is shown in final form by Eq. (3.6).

$$Er_{sf} = \sigma \frac{dA_{i,s}}{dt} \tag{3.6}$$

(c) Energy required to overcome the inertia effect (Er_i):

Inertia force acting over the bubble is given by Eq. (3.7) following [99, 100, 171].

$$F_i = \frac{G^2}{\rho_l} A_{i,c/s} \tag{3.7}$$

Energy required to overcome the inertia effect is calculated by multiplying the inertia force with bubble growth rate as shown in Eq. (3.8).

$$Er_i = F_i \times \dot{\text{growth rate}} = \rho_l A_{i,c/s} v^2 \frac{dr}{dt} = \frac{G^2}{\rho_l} A_{i,c/s} \frac{dr}{dt} \tag{3.8}$$

(d) Energy required to overcome the drag effect (Er_{sh}):

Flowing fluid exerts the drag force on the bubble. Only half portion of vapor bubble is directly exposed to the flowing fluid and it experiences the drag force. Effect of the drag force on downstream direction is neglected due to the formation of eddies, which creates flow separation in downward direction. The drag force acting over the bubble is given by Eq. (3.9) following [99, 100].

$$F_{sh} = \mu \frac{G}{2\rho_l r} \times \frac{A_{i,s}}{2} \tag{3.9}$$

Energy required to overcome the drag effect is calculated by multiplying the drag force with bubble growth rate as shown in Eq. (3.10).

$$Er_{sh} = F_{sh} \times growth\,rate = \mu \frac{G}{2\rho_l r} \times \frac{A_{i,s}}{2} \times \frac{dr}{dt} \tag{3.10}$$

(e) Energy required to overcome the gravity (buoyancy) effect (Er_g):

The effect of gravity (buoyancy) is due to density difference between liquid and vapor phase. Energy required to overcome the gravity (buoyancy) effect is given by Eq. (3.11).

$$Er_g = g\left(\rho_l - \rho_v\right) \cdot a \frac{dV_i}{dt} \tag{3.11}$$

(f) Energy required to overcome the force due change in evaporation momentum (Er_m):

Evaporation at the interface results in a force due to change in momentum as vapor leaves the interface [97-100]. The force due to change in momentum due to evaporation is given by Eq. (3.12).

$$F_m = \frac{q''}{h_{fg}} \times A_{i,s} \times \frac{q''}{h_{fg}\rho_v} \tag{3.12}$$

Thus, energy required to overcome this effect is computed by multiplying the force due to change in evaporation momentum with bubble growth rate as shown in Eq. (3.13).

$$Er_m = \frac{q''}{h_{fg}} \times A_{i,s} \times \frac{q''}{h_{fg}\rho_v} \times \frac{dr}{dt} \tag{3.13}$$

The instantaneous volume (V_i), surface area ($A_{i,s}$), cross sectional area ($A_{i,c/s}$) and centroid (a) of the bubble are derived in terms of contact angle and bubble radius. Complete derivations of V_i, $A_{i,s}$, $A_{i,c/s}$, and a are provided in Appendix A.2. The shape of the bubble is assumed as a truncated sphere as shown in Fig. 3.2.

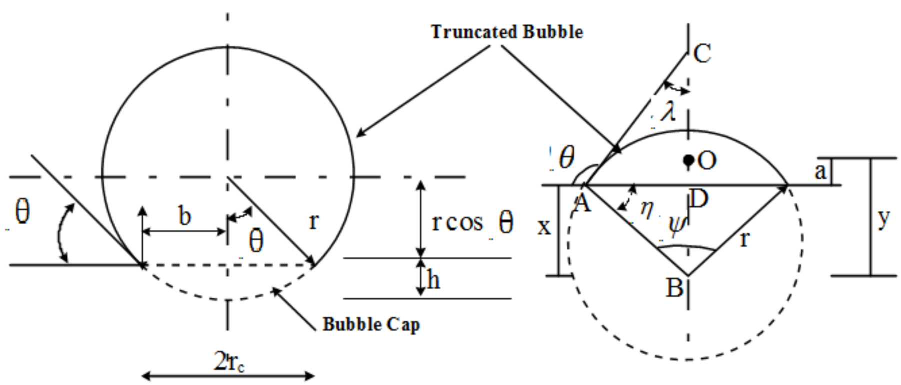

Figure 3.2 Diagram of truncated bubble and centroid of the bubble

Instantaneous volume, surface area and cross sectional area of the bubble are given by Eq. (3.14), Eq. (3.15) and Eq. (3.16), respectively.

$$V_i = \frac{\pi}{3} \cdot r^3 \alpha \tag{3.14}$$

$$A_{i,s} = \pi \cdot r^2 \cdot \beta \tag{3.15}$$

$$A_{i,c/s} = \frac{1}{2} \cdot r^2 \gamma \tag{3.16}$$

Where, α, γ and β are given by Eq. (3.17-3.19).

$$\alpha = \left[4 - 0.5\left\{ 3(1-\cos\theta)\sin^2\theta + (1-\cos\theta)^3 \right\} \right] \tag{3.17}$$

$$\beta = \left[4 - \left\{ \sin^2\theta + (1-\cos\theta)^2 \right\} \right] \tag{3.18}$$

$$\gamma = \left[2\pi - \frac{2\pi\theta}{180} + \sin 2\theta \right] \tag{3.19}$$

The location of the centroid of the bubble is shown in Fig. 3.2 at point 'o'. The distance between centroid of the bubble and plate is given by Eq. (3.20).

$$a = y - x = r \left[\frac{4\sin^3\left(\frac{\psi}{2}\right)}{3(\psi - \sin\psi)} - \sin\left(90 - \frac{\psi}{2}\right) \right] = r\phi \tag{3.20}$$

Where, ψ and ϕ are given by Eq. (3.21-3.22).

$$\psi = 2(180 - \theta) \tag{3.21}$$

$$\phi = \left[\frac{4\sin^3\left(\frac{\psi}{2}\right)}{3(\psi - \sin\psi)} - \sin\left(90 - \frac{\psi}{2}\right) \right] \tag{3.22}$$

Substituting Eq. (3.3, 3.4, 3.6, 3.8, 3.10, 3.11, and 3.13 – 3.16) into the Eq. (3.2), the bubble growth rate is given by Eq. (3.23).

$$q'' \frac{A_c}{A_{ch}} \frac{\gamma}{2} r^2 = r^2 \frac{dr}{dt} \left[\pi \cdot \alpha \cdot \rho_v h_{fg} + \frac{G^2}{2\rho_l}\gamma + \left(\frac{q''}{h_{fg}} \right)^2 \frac{\pi \cdot \beta}{\rho_v} \right]$$
$$+ r \cdot \frac{dr}{dt} \left[\sigma \cdot (2 \cdot \pi \cdot \beta) + + \mu \frac{G}{4 \cdot \rho_l} \pi \cdot \beta \right] + r^3 \frac{dr}{dt} \left[g(\rho_l - \rho_v) \frac{\pi \cdot \alpha \cdot \phi}{2} \right] \tag{3.23}$$

Integrating Eq. (3.23), we get general bubble growth equation in terms of heat supplied, mass flux, thermal properties of the flowing fluid and channel geometry, Eq. (3.24).

$$q''\frac{A_c}{A_{ch}}\frac{\gamma}{2}t=\left[g\left(\rho_l-\rho_v\right)\frac{\pi\cdot\alpha\cdot\phi}{2}\right]\cdot r^2+\left[\sigma\cdot\left(2\cdot\pi\cdot\beta\right)+\frac{\mu\cdot G}{4\cdot\rho_l}\pi\cdot\beta\right]\ln(r)$$
$$+\left[\pi\cdot\alpha\cdot\rho_v h_{fg}+\frac{G^2}{\rho_l}\frac{\gamma}{2}+\left(\frac{q''}{h_{fg}}\right)^2\frac{\pi\cdot\beta}{\rho_v}\right]\cdot r+C \tag{3.24}$$

Bubble growth at nucleation site is finally calculated by solving Eq. (3.24) at given operating conditions (G, q''), channel geometry (A_{ch}), and thermal properties of working fluid (h_{fg}, μ, ρ_l, ρ_v,) at different time intervals (from experimental observations) by Secant method [183].

Integration constant (C) is calculated by applying boundary condition; $t = t_{FV} = 0; r = r_c = r_{min}$ and given by Eq. (3.25). As the bubble becomes visible at nucleation site, when it reaches up to cavity mouth, the minimum visible bubble radius is assumed as nucleation cavity radius and is given by Eq. (3.25). Stepwise derivation of Eq. (3.24) is provided into Appendix A.3.

$$C=-\left[g\left(\rho_l-\rho_v\right)\cdot\frac{\pi\cdot\alpha\cdot\varphi}{2}\right]\cdot r_{\min}^2-\left[\frac{\mu\cdot G}{\rho_l}\frac{\pi\cdot\beta}{4}+2\pi\cdot\rho\cdot\beta\right]\cdot\ln(r_{\min})$$
$$-\left[\pi\cdot\alpha\cdot\rho_v h_{fg}+\frac{G^2}{\rho_l}\frac{\gamma}{2}+\left(\frac{q''}{h_{fg}}\right)^2\frac{\pi\cdot\beta}{\rho_v}\right]\cdot r_{\min} \tag{3.25}$$

Contact angle at the time of bubble inception is assumed as (θ_{incep} = 90) following [81,184]. During the process of bubble growth at nucleation cavity, contact angle decreases with increase in bubble radius. However, no effort has been made in previous works relating variation of the contact angle during the bubble growth with fluid property [185] and the time lapsed after inception. An empirical relation (Eq. 3.26) has been developed in order to find out contact angle variation during the bubble growth in terms of surface tension (σ) and time (t), following experimental work of [81].

$$\theta = \theta_{incep} - 13.794\ln(t) - 2.31\ln(\sigma) \tag{3.26}$$

Where, θ is in degree, t is in ms and σ is in N/m.

3.3 Results and discussion

Few experimental works are available in open literature on bubble growth at the nucleation site for microchannels [38, 39, 81, 186]. Figure 3.3 shows comparison of the proposed model with Lui et al. [81] experimental and Zhuan and Wang [103] numerical work. Results show good agreement between bubble diameter predicted by the model and experimental data. The mean absolute percentage error (MAPE) of Zhuan and Wang [103] numerical study is around 7%, whereas MAPE of current model is around 14%.

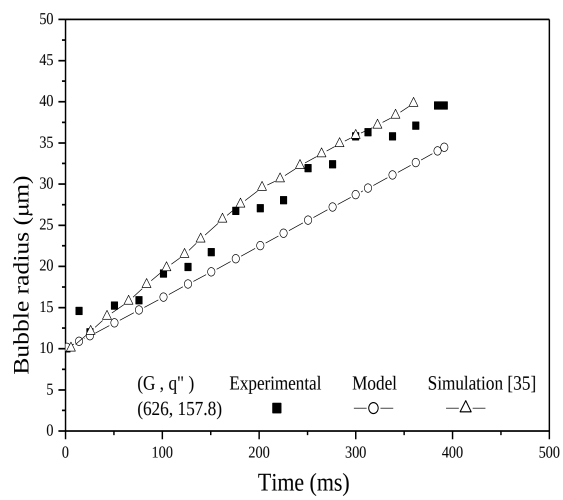

Figure 3.3 Comparison of present model with Lui et al. [81]

In order to find out the influence of energy consumed in bubble growth and different resistive effects on growth process, their variations during entire bubble growth period since inception until departure need to be investigated. Figure 3.4 shows variations of the energy consumed in growing bubble and resistive effects during bubble growth period. Evaporation at an interface (E_{bubble}) consumes largest proportionate of energy [187] and remaining energy is utilized in resistive effects i.e. surface tension, inertia, drag, gravity (buoyancy) and change in momentum due to evaporation. Among resistive effects, the surface tension is most detrimental to bubble growth. Moreover, as expected, the magnitude of all these resistive effects increases during bubble growth period.

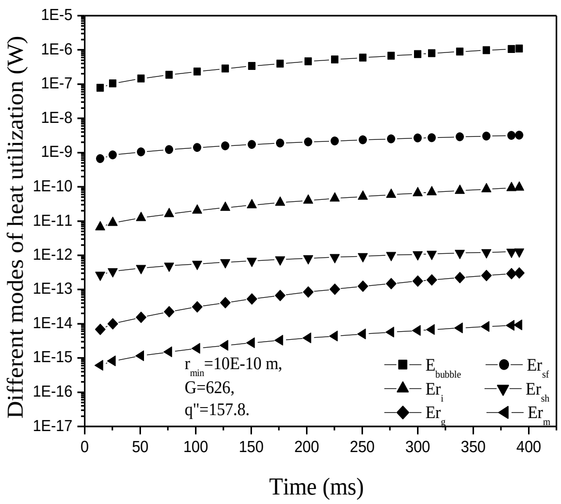

Figure 3.4 Variation of energy utilization in various effects during bubble growth

The present model is also compared with experimental work of [38, 39, 186]. Figure (3.5 – 3.7) show the results of comparative analysis between current model and experimental results of [38, 39, 186] respectively.

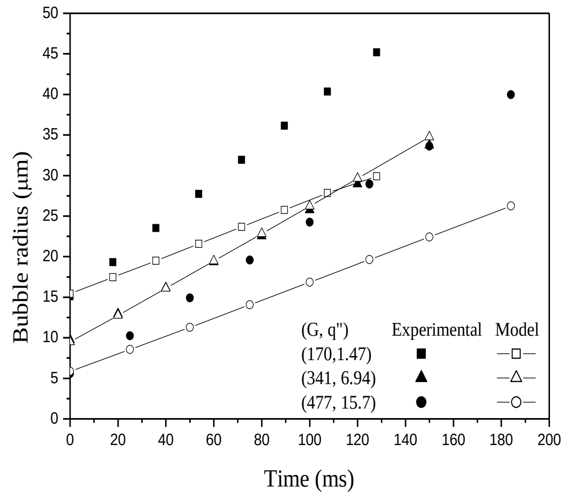

(a)

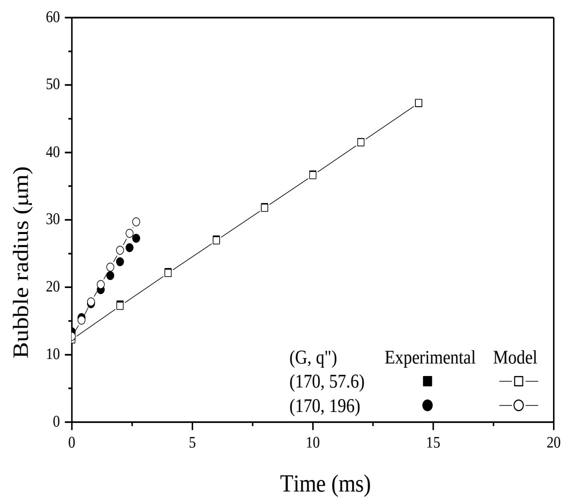

(b)

Figure 3.5 (a), (b) Comparison of present model with Lee et al. [38]

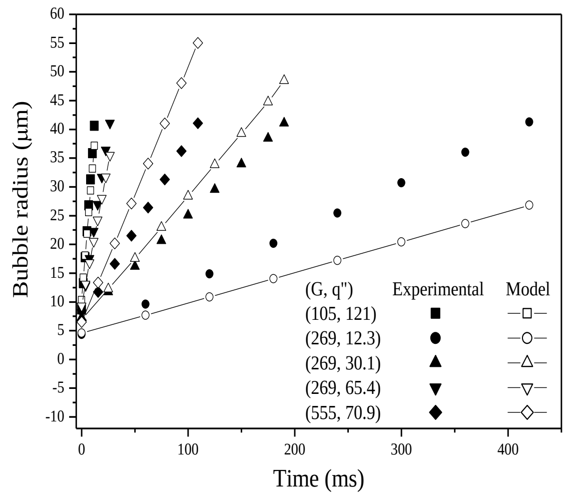

Figure 3.6 Comparison of present model with Li et al. [39]

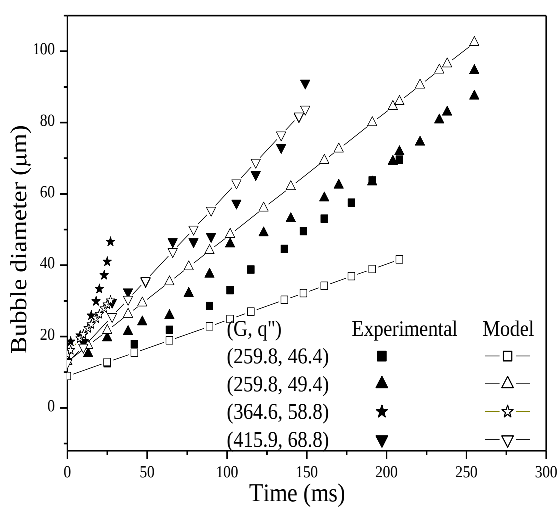

Figure. 3.7 Comparison of present model with Meder [186]

MAPE between value predicted by the model and experimental data is calculated by Eq. (3.27).

$$\mathrm{MAPE}(\%) = \frac{\sum_{1}^{N} \left| \frac{r_{meas} - r_{pred}}{r_{meas}} \right|}{N} \times 100 \tag{3.27}$$

Table 3.1 gives summary of the MAPE between predicted data and the experimental data at different heat flux and mass flux conditions. From Table 3.1, it can be observed that the current model over predicts in certain cases and also under predicts in certain cases.

Table 3.1

Summary of MAPE between experimental data and present model

Author	G (kg/m^2s)	q" (kW/m^2)	MAPE %	Remark
Liu et al [81]	626	157.8	14	Under prediction
Li et al [39]	105	121	0.1	Negligible
	269	12.3	25.8	Under prediction
	269	30.1	10.8	Over prediction
	269	65.4	5.5	Negligible
	555	70.6	23	Over prediction
Lee et al [38]	170	1.47	20.8	Under prediction
	170	57.6	0.7	Negligible
	170	196	3.5	Negligible
	341	6.94	0.6	Negligible
	477	15.7	24.3	Under prediction
Meder [186]	259.8	46.7	25	Under prediction
	259.8	49.4	16.4	Over prediction
	364.6	58.8	14.7	Under prediction
	415.9	66.8	1.1	Negligible

Over prediction can be attributed to associated heat losses occurring from the test section and possible condensation at the top portion of vapor bubble during subcooled boiling [188], which suppresses actual size of vapor bubble. Whereas, under prediction may be due to the merging of small vapor bubbles generated in close neighborhood of the bubble under consideration. In certain observations MAPE is greater than 20%. This may be due to presence of unsteady growth force, which arises due to fluctuation in local flow field [189].

From Table 3.1, it is also observed that at constant heat flux, bubble growth rate decreases with increase in mass flux. As mass flux increases at constant heat flux, energy consumed in overcoming the inertia and the drag resistive effects also increase. Hence, bubble grows slowly and associated waiting time would increase. On the other hand bubble growth increases with increase in heat flux at constant mass flux and associated waiting time would reduce. This may be accredited to the enhancement in evaporation rate at high heat flux.

3.4 Waiting Time

When bubble nucleates at the nucleation cavity, it takes time to grow. Waiting time is very important phenomena as far flow boiling is concern. This gives information that how frequently next bubble is generated from the active nucleation site. Basu et al. [188, 190] and Yeoh et al. [191] defined waiting time (t_w) as the time period between bubble departure and next bubble inception at a given nucleation site (small circular cavity). Figure 3.8 represents the waiting time and growth time of the vapor bubble nucleated at nucleation site [192]. Bubble is incepted at point '*O*' and grows till point '*P*'. At '*P'*, bubble departed from the nucleation site. There is no bubble for duration between point '*Q*' and point '*R*'. At point '*R*', new bubble starts growing at nucleation site. Time interval between 'O' and 'Q' represent bubble growth period (t_g) at nucleation site and time interval between point '*Q*' and point '*R*' represents waiting time (t_w).

Bubble waiting time along with growth time is helpful in determining the bubble release frequency ($1/(t_w+t_g)$) of the active nucleation site [192, 193]. Information of the bubble release frequency is important variable in predicting the nucleate boiling heat flux [193, 194].

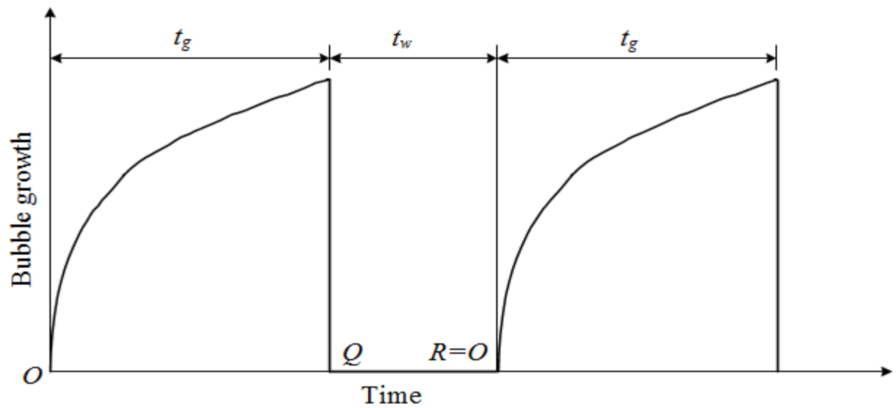

Figure 3.8 A schematic showing bubble growth and waiting time [192]

Shape and size of the nucleation cavity is dependent on surface roughness, which eventually depends on the type of manufacturing process used for fabrication purpose. In actual, nucleation site may be approximated as inverted cone as reported by Lui et al. [81], Lee et al. [178], Fazel and Shafaee [195], Li and Cheng [196] and Kandlikar [132].

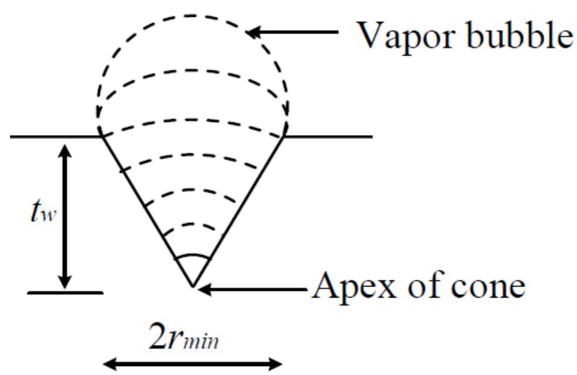

Figure 3.9 Stages of bubble nucleation process

Very first point where the bubble can incept in case temperature reaches to the saturation temperature is apex of the inverted cone, Fig. 3.9. Thus, vapor bubble is more likely to initiate at the apex of cavity ($r = 0$) and grows inside the cavity [197]. When bubble reaches at the cavity mouth ($r = r_{min}$), it can be visualized through high speed photography. To obtain waiting time, it is assumed that bubble grows inside the cavity in similar manner as it grows outside the cavity. Thus, slope of the bubble growth line will remain constant even in the period since inception to the first visualization at a given nucleation site and is given by Eq. (3.28).

$$\left.\frac{dr}{dt}\right|_{r=r_{\min}} = \frac{q'' \frac{A_c}{A_{ch}} \frac{\gamma}{2}}{\left[\pi \cdot \alpha \cdot \rho_v h_{fg} + \frac{G^2}{2\rho_l}\gamma + \left(\frac{q''}{h_{fg}}\right)^2 \frac{\pi \cdot \beta}{\rho_v}\right] + \left[\sigma \cdot (2 \cdot \pi \cdot \beta) + \mu \frac{G}{4 \cdot \rho_l} \pi \cdot \beta\right] \frac{1}{r_{\min}} + \left[g\left(\rho_l - \rho_v\right) \frac{\pi \cdot \alpha \cdot \varphi}{2}\right] \cdot r_{\min}} \tag{3.28}$$

This slope is applied between conditions; (1) $t = 0; r = 0$, and (2) $t = t_w; r = r_{min}$. Eventually, the waiting time can be obtained by Eq. (3.29).

$$t_w = \frac{r_{\min}}{\left.\frac{dr}{dt}\right|_{r=r_{\min}}} \tag{3.29}$$

Experimental waiting time is obtained by extrapolating experimental data up to $r = 0$. Table 3.2 shows the summery of waiting time calculated through experimental data and by current proposed model. From Table 3.2, it is validated that at constant heat flux, waiting time value increases with increase in mass flux. Whereas, waiting time value decreases with increase in heat flux. Expected reason for these is already explained in previous section.

Table 3.2

Summary of waiting time calculation

Author	G	q"	waiting time	
			Model	Experimental
	(kg/m^{2}s)	(kW/m^2)	ms	ms
Liu et al [81]	626	157.8	161.7	151.3
Li et al [39]	105	121	4.5	3.83
	269	12.3	88	49
	269	30.1	32.1	41.54
	269	65.4	9.21	6.17
	555	70.6	14.6	22.28
Lee et al [38]	170	1.47	132	64.3
	170	57.6	5	5.23
	170	196	2	2.6
	341	6.94	57.6	60.87
	477	15.7	52.84	29.73
Meder [186]	259.8	46.7	58.1	15.95
	259.8	49.4	37.6	35.7
	364.6	58.8	29.9	43
	415.9	66.8	27.4	28.29

3.5 Non dimensional Group

Since the boiling process is very complex, it is very difficult to model every phenomena theoretically associated with boiling process such as heat transfer characteristics, pressure drop characteristics and critical heat flux. These phenomena can be better understood through various non dimensional numbers that can be derived from the various governing effects involved into the boiling process. These numbers are generally the ratio of the two governing effects. The bubble growth model involve various terms which describe the energy required for bubble growth and overcoming the various resistive effects. These energy terms can be utilized to identify the non dimensional group during bubble growth at nucleation site in microchannel which can be helpful in providing more insight of flow boiling phenomena in microchannel. Hence, effort has been made to extend the bubble growth model to develop the non dimensional energy ratio. Fig. 3.4 shows the variation of E_{bubble}, Er_{sf}, Er_i, Er_{sh}, Er_g and Er_m. It can be observed that the energy required to overcome resistive effect of evaporation momentum is negligible out of these. Hence, this effect has not been considered in current non-dimensional study. Following that, E_{bubble}, Er_{sf}, Er_i, Er_{sh}, and Er_g are remaining influencing parameters in Eq. 3.2. During current analysis, energy required to overcome the surface tension effect has been taken as reference as it plays important role in bubble growth and departure both in microchannels. Four dimensionless energy ratio terms have been formed as: E_1, E_2, E_3 and E_4 as shown by Eq. (3.30 – 3.33).

$$E_1 = E_{bubble} / Er_{sf} = \frac{\rho_v h_{fg}}{2\sigma} r \frac{\alpha}{\beta} \tag{3.30}$$

$$E_2 = Er_i / Er_{sf} = \frac{r\, G^2}{\rho_l \sigma} \left(\frac{\gamma}{4\pi\beta} \right) = We \left(\frac{\gamma}{4\pi\beta} \right) \tag{3.31}$$

$$E_3 = Er_{sh} / Er_{sf} = \frac{\mu\, G}{8\rho_l \sigma} = \frac{Ca}{8} \tag{3.32}$$

$$E_4 = Er_g / Er_{sf} = \frac{g\left(\rho_l - \rho_g\right)}{2\sigma} r^2 \left(\frac{\phi\alpha}{\beta} \right) = \frac{Bo}{2} \left(\frac{\phi\alpha}{\beta} \right) \tag{3.33}$$

Where, $We\left(= \frac{r\, G^2}{\rho_l \sigma} \right)$ is Weber number, $Ca\left(= \frac{\mu\, G}{\rho_l \sigma} \right)$ is Capillary number, $Bo\left(= \frac{g\left(\rho_l - \rho_g\right)}{\sigma} r^2 \right)$ is Bond number. E_1 is the ratio of the energy required for bubble growth to the energy required to overcome the surface tension effect. E_2 is the ratio of the energy required to overcome the inertia effect to the surface tension effect. It finally appears in terms of the Weber number. E_3 is the ratio of energy required to overcome drag effect and surface tension effect. E_3 is function of the capillary number. E_4 is the ratio of the energy required to overcome the gravity (buoyancy) effect to the surface tension effect. It appears in terms of the Bond number.

Many researchers had carried out experimental studies of bubble growth at nucleation site [81 38, 39, 182] in microchannels. But, they had not observed inertia controlled region and diffusion controlled region distinctly in their experimental studies. They reported that bubble grows at nucleation site in linear manner. A very few experimental studies [86, 87] were found in the open literature, which clearly indentified these regions separately during bubble growth at nucleation site in microchannel.

Following Bogojevic et al. [86] study, it is observed that period of the inertia controlled region is very short as compared to thermal diffusion controlled region. This could be a possible reason that in earlier studies this region was not given major attention or may be due to limitation of high speed photography. The above mentioned non-dimensional groups are plotted following instantaneous values of bubble radius (since inception till departure) as reported in experimental work of Bogojevic et al. [86]. Fig.3.10 – 3.13 shows the variation of E_1, E_2, E_3 and E_4 during the entire bubble life. Note that bubble growth approximately above 225 ms is not of our interest as bubble interface enters in boundary layer of the adjacent wall. It is clear from these figures that E_1 and E_2 play important role in bubble growth at nucleation site. E_3 does not change with time during entire bubble growth at nucleation site as shown in Fig. 3.12. The effect of E_4 is almost negligible. Hence, gravitation force does not play any significant role. Variation of E_1 and E_2 show that they can be utilized to distinguish the inertia controlled and thermal diffusion controlled region. E_2 appears in terms of the *We*, which is useful in defining the dominance of the surface tension and flow inertia on flow patterns in microchannel [98].

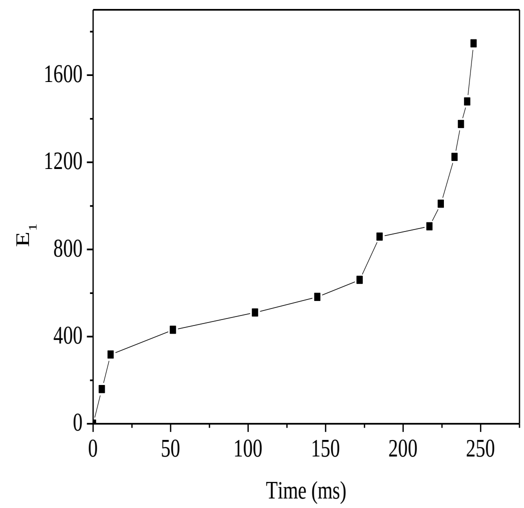

Figure 3.10 Variation of the E_1 with time

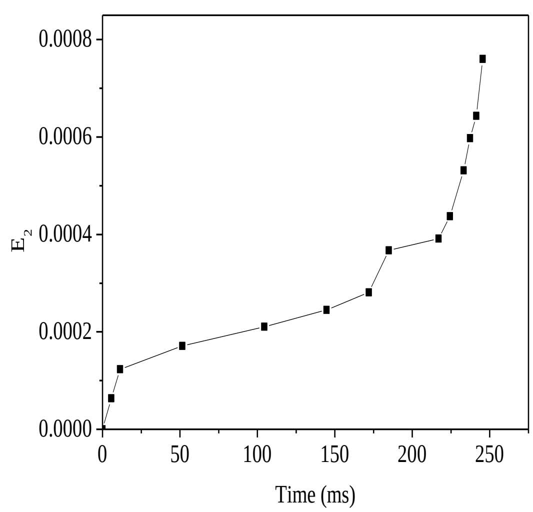

Figure 3.11 Variation of the E_2 with time

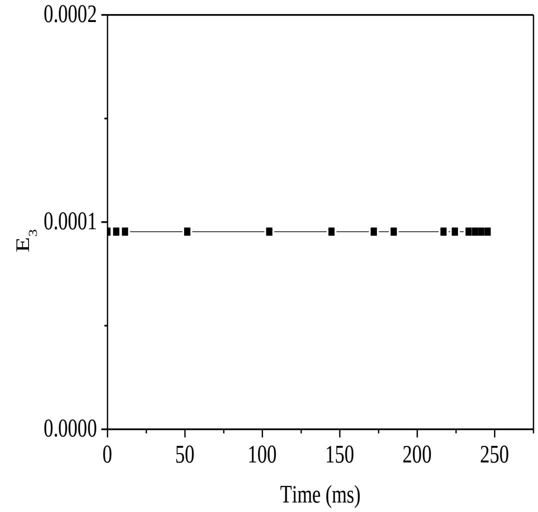

Figure 3.12 Variation of the E_3 with time

Thus, E_1 is most meaningful for differentiating inertia controlled region and diffusion controlled region. It consists of the surface tension term, which is dominating in early stage of the bubble growth and latent heat of the evaporation, which plays important role in later stage of the bubble growth.

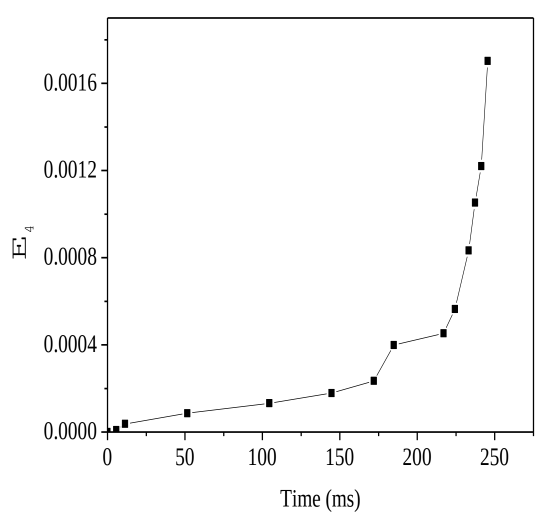

Figure 3.13 Variation of the E_4 with time

Initially the value of E_1 increases very rapidly and attains value of around 400 within a short time (around 25 ms). In this region bubble size is very small thus surface tension effect plays an important role. Later, the slope of the curve reduces as the bubble size increases. In this region, evaporation is mainly responsible for further growth of bubble as surface tension effects turns weaker. Thus, bubble growth in this region is governed by the thermal diffusion taking place at the liquid vapor interface. Hence, variation of E_1 can be used successfully for easily recognizing inertia controlled region and diffusion controlled regions. Transition of inertia to thermal diffusion is found to occur in the range of E_1 from 1300 to 2400 under different operating conditions [87]. Thus, more efforts are required to generalize the inertia controlled region in terms of operating conditions.

From the Fig. 3.10 it is clear that rate of bubble growth is much higher in inertia controlled region than thermal diffusion controlled region. Hence, it implies that rate of the heat transfer from the surface is much higher to fluid in the inertia controlled region than the thermal diffusion controlled region. If the bubble can be departed before it enters into thermal diffusion controlled region, higher heat transfer rate can be achieved.

3.6 Impact of non dimensional numbers on critical heat flux

Intrinsic relationship between bubble dynamics and associated two phase flow regimes is not well understood at micro level. Two phase flow starts with bubble formation at active nucleation sites on heated surface. Unusually in case of microchannel; single bubble may grow to the size of channel and completely blocks the flow. The above is in contradiction with boiling on conventional scale channel. Considerable attention had been put in past to visualize isolated bubble growth pattern in case of microchannels.

Flow blocking by the individual channel has dramatic influence on two phase flow behavior of microchannels. It induces temperature and velocity fluctuations apart of fueling various instabilities. It is more like the critical heat flux condition and actually activates it. Critical heat flux; which decides the upper thermal limit of performance of microchannel heat sink under given operating conditions requires special attention. The effort has been made to relate the influence of non-dimensional energy ratio on critical heat flux condition. Following are the expected impacts of the non-dimensional numbers on critical heat flux.

E_1 indicates the ratio of energy that is utilized in the bubble growth process (which finally stores inside vapor bubble) to the energy required in overcoming resistive surface tension effect. Larger value of E_1 implies either vapor bubble posses large energy or effect of resistive surface tension effect is weak. Under both circumstances, bubble behavior is entirely different. If E_1 is large due to high value of h_{fg} (low evaporation rate) or ρ_v (formation of denser bubble) under both conditions bubble growth rate reduces; otherwise bubble growth rate is fast but bubble is not stable (thinner bubble) thus collapses easily. Side effects of flow blocking transmit frequently in fluids with low value of E_1. And, the fluid suffers from the early occurrence of CHF condition in comparison to the fluid with high value of E_1.

E_2 represents the ratio of energy required to overcome inertia effect to the surface tension effect acting upon the vapor bubble. Both of these two effects have negative influence on bubble growth rates. High value of the inertia effect helps in early detachment of vapor bubble from nucleation site thus helps in avoiding flow blockage condition as required for stable flow boiling condition. The effect of surface tension effect is already discussed, weak surface tension effect helps in rapid growth of bubble but it destabilizes vapor bubble by formation of thinner vapor bubble. Thus, ideally fluid should have high inertia effect. If the vapor bubble continue to stick nucleation site then high value of surface tension is beneficial otherwise low value of surface tension is helpful as it helps in easy collapsing of vapor bubble. As surface tension plays more vital role in boiling process at microscale, the value of E_2 should be small in order to have stable boiling process. Small value of E_2 can help in avoiding early occurrence of CHF condition in microchannel. Similarly, E_3 is the ratio of energy required to overcome viscous effect to the surface tension effect acting upon the vapor bubble. Viscous force increase helps in detachment vapor bubble from the nucleation site, frequent removal of vapor bubble from nucleation site stabilizes the boiling process and helps in avoiding flow blocking, which ultimately delays CHF condition.

E_4 represents the ratio of energy required to overcome resultant gravitational effect to the surface tension effect acting upon the vapor bubble. The resultant gravitational force acting on the vapor bubble tries to pull up vapor bubble out of nucleation site, which is required condition for stable boiling process. Thus, value of E_4 should be higher to avoid early occurrence of the CHF condition. However, many past researchers [96, 98] had quoted that effect of buoyancy force can be neglected for the microchannels.

From above discussion, it is clear that critical heat flux is strongly influenced by the bubble dynamics of individual bubble in case of microchannel.

3.6 Conclusion

Simplified mathematical model has been developed to predict the bubble growth at nucleation site following assumption that heat supplied at the nucleation site is divided between liquid phase and vapor phase as per instantaneous void fraction value. Heat consumed by the vapor phase is utilized in overcoming resistive effects and growth of vapor bubble. New empirical relation is developed to obtain contact angle in terms of time and surface tension during the growth period.

1. It is found that bubble growth is influenced by heat flux, mass flux, thermophysical properties of the liquid and channel geometry.

2. Presented model shows good agreement with the past experimental studies available with maximum MAPE of 25%.
3. Waiting time phenomena is discussed and current model is utilized to predict waiting time. Predicted waiting time is also found close to experimental waiting time. It is observed that the waiting time increases with increase in mass flux and decreases with increase in heat flux.
4. Bubble growth model is extended for developing non dimensional energy ratio. The new non dimensional energy ratio number E_1 is proposed to differentiate inertia controlled region and thermal diffusion controlled region. Eventually, possible impacts of the non-dimensional energy terms on critical heat flux are discussed.

CHAPTER 4

DEVELOPMENT OF NEW CHF CORRELATION FOR MICROCHANNEL

4.1 Introduction

Unlike conventional channels, empirical equations for microchannel are limited in number. Importantly, none of the previously proposed CHF correlations (Table 2.8) was generated to model CHF due to bubble dynamics leading to bubbles clogging the microchannel. Significant variations in CHF predictions for microchannels are observed, when they are tested against reported experimental data (discuss in result and discussion section). Detailed theoretical models based on evaporation of thin liquid film trapped between heating surface and vapor slug is lengthy and time consuming. From the previous chapter, it is concluded that non-dimensional number developed using bubble growth model can be useful in determining the critical heat flux in microchannel. Therefore, in the present chapter, an effort has been made to develop a new correlation for CHF conditions (associated with bubble growth and clogging) realized in microchannels that employ a uniform heat-flux “method of heating”. This approach is based on a non-dimensional analysis (Buckingham's Π theorem) that is coupled to an energy based bubble growth model at nucleation sites developed in chapter 3.

Bubble dynamics plays an important role in any boiling process but its importance increases many folds as channel dimension goes down from macro to micro level. At micro level individual bubble growth starts influencing many aspects of boiling such as heat transfer rate, temperature and pressure field distribution in a very unusual manner – this is due to liquid flow field’s complete confinement by individual bubbles. Many researchers have stated that this can lead to an early occurrence of CHF in case of flow boiling in a microchannel. Kenny et al. [198] write "In a microchannel system, the bubble can grow to fill the channel before detachment, leading to complete blockage and early dryout of the channels." Mukherjee and Kandlikar [199] write "The resulting reversed flow is detrimental to the heat transfer and leads to early CHF condition." Hence, for this mechanism, state of CHF in microchannel depends on bubble growth rate.

4.2 Development of new CHF model for microchannel

In chapter 3, development of energy based model for prediction of the bubble growth at nucleation site in microchannel is discussed. From this model (Eq. 3.24) it is observed that bubble growth is dependent on various parameters (ρ_l, ρ_v, σ, μ_l, g, h_{fg}, G, r_i, α, β, γ, and ϕ). Where, α, β, γ, and ϕ are non-dimensional angle parameters associated with bubble volume, surface area, cross section area and centroid of vapor bubble – and they all are functions of the equilibrium contact angle. Details of α, β, γ, and ϕ are available in Appendix 2. Gravity (g) is considered as variable as it influences buoyancy force acting on the bubble and it also facilitates representation of complete CHF correlation in terms of energy consumed in various processes [200]. In case of supplied heat flux $q" < q_{\mathrm{CHF}}$, the terminal value of instantaneous bubble radius r_i at any nucleation site is less than channel dimension. However, for $q" \geq q_{\mathrm{CHF}}$, the vapor bubble occupies entire cross section of the channel. Hence, r_i for such critical heat flux condition can be considered to be approximately equal to hydraulic radius ($r_i = r_h = D_h/2$).

Hence, for this mechanism, CHF can be given by Eq. (4.1).

$$q_{CHF} = f\left(\rho_l, \rho_v, \sigma, \mu_l, \mathrm{g}, h_{fg}, G, r_h, \alpha, \beta, \gamma, \phi\right) \quad (4.1)$$

Total number of variables (n) are thirteen including q_{CHF}. Thus, q_{CHF} is function of the twelve variables. Bubble radius (r_h), surface tension (σ), mass flux (G) and α are set as repeating variables (k = 4). Following Buckingham's Π theorem [200], the number of Π terms are nine ($n - k$ = 9) and each Π term is function of repeating variables plus one of the remaining variables. They are given by Eq. (4.2) – Eq. (4.10). Detail steps of the non dimensional analysis are provided in Appendix 4.

$$\Pi_1 = q_{CHF} r_h^{a_1} \sigma^{b_1} G^{c_1} \alpha^{d_1} \tag{4.2}$$

$$\Pi_2 = \rho_v r_h^{a_2} \sigma^{b_2} G^{c_2} \alpha^{d_2} \tag{4.3}$$

$$\Pi_3 = \rho_l r_h^{a_3} \sigma^{b_3} G^{c_3} \alpha^{d_3} \tag{4.4}$$

$$\Pi_4 = \mu_l r_h^{a_4} \sigma^{b_4} G^{c_4} \alpha^{d_4} \tag{4.5}$$

$$\Pi_5 = g r_h^{a_5} \sigma^{b_5} G^{c_5} \alpha^{d_5} \tag{4.6}$$

$$\Pi_6 = h_{fg} r_h^{a_6} \sigma^{b_6} G^{c_6} \alpha^{d_6} \tag{4.7}$$

$$\Pi_7 = \beta r_h^{a_7} \sigma^{b_7} G^{c_7} \alpha^{d_7} \tag{4.8}$$

$$\Pi_8 = \gamma r_h^{a_8} \sigma^{b_8} G^{c_8} \alpha^{d_8} \tag{4.9}$$

$$\Pi_9 = \phi r_h^{a_9} \sigma^{b_9} G^{c_9} \alpha^{d_9} \tag{4.10}$$

Principle of dimensional homogeneity is applied to find coefficients of the Eq. (4.2) – Eq. (4.10). Table 4.1 presents the value of these coefficients for each Π term.

Table 4.1

Values of coefficients a_k, b_k, c_k and d_k

Π_k	a_k	b_k	c_k	d_k
Π_1	2	–2	1	0
Π_2	−1	1	−2	0
Π_3	−1	1	−2	0
Π_4	−1	0	−1	0
Π_5	3	−2	2	0
Π_6	2	−2	2	0
Π_7	0	0	0	−1
Π_8	0	0	0	−1
Π_9	0	0	0	−1

The proposed (discussed in chapter 3) non dimensional energy ratio terms (E_1, E_2, E_3, E_4 given by Eq. (3.302) – Eq. (3.33)) and analyzed their variation during bubble growth at nucleation site in microchannel. Following these, Π terms (except Π_1) are converted into four modified Π terms in such a way so that each modified Π term contains one non dimensional energy ratio term. Modified Π terms are given by Eq. (4.11) – Eq. (4.14).

$$\Pi_{E_1} = \frac{\Pi_2 \cdot \Pi_6}{\Pi_7} = \frac{\rho_v h_{fg}}{\sigma} r_h \frac{\alpha}{\beta} \tag{4.11}$$

$$\Pi_{E_2} = \frac{\Pi_8}{\Pi_3 \cdot \Pi_7} = \frac{G^2 r_h}{\rho_l \sigma} \frac{\gamma}{\beta} \tag{4.12}$$

$$\Pi_{E_3} = \frac{\Pi_4}{\Pi_3} = \frac{\mu_l G}{\rho_l \sigma} \tag{4.13}$$

$$\Pi_{E_4} = \left(\Pi_3 - \Pi_2\right) \cdot \Pi_5 \cdot \Pi_9 = \frac{g\left(\rho_l - \rho_v\right) r_h^{\,2}}{\sigma} \frac{\phi}{\alpha} \tag{4.14}$$

Process of confinement of cross sectional area of flow begins with partial confinement as shown in Fig. 4.1(a). It is the state at which vapor bubble size reaches up to minimum dimension of microchannel. The confinement process terminates at full confinement state, when vapor starts touching all sides of microchannel as shown in Fig. 4.1(b). The time lag between partial confinement and full confinement also influences CHF value and it depends on (W/H) ratio. Hence, $\Pi_{AR} = W/H$ has been included as non-dimensional term. Similarly, effect of inlet subcooling on CHF [165 – 167] has been taken in to account by introduction of another non dimensional term $\Pi_{sub} = T_{in}/T_{sat}$. Function correlating above seven non dimensional Π terms is given by Eq. (4.15),

$$f\left(\Pi_1, \Pi_{E_1}, \Pi_{E_2}, \Pi_{E_3}, \Pi_{E_4}, \Pi_{AR}, \Pi_{sub}\right) = 0 \tag{4.15}$$

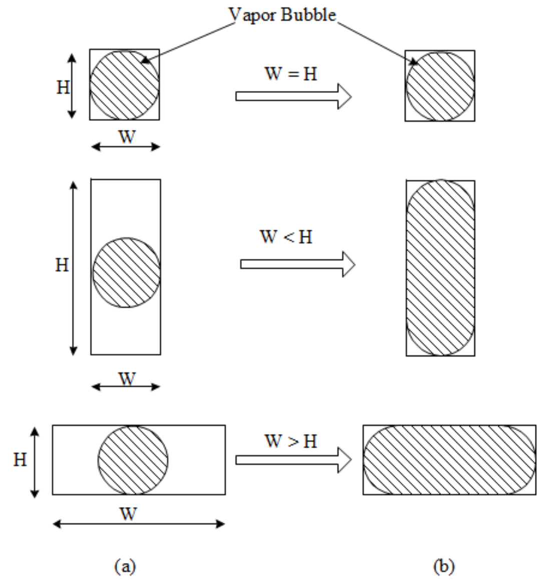

Figure 4.1 States of bubble confinement in different type of cross section: (a) partial confinement, (b) full confinement

Equation (4.15) can also be written as;

$$\frac{q_{CHF} G r_h^2}{\sigma^2} = C\left(\frac{\rho_v h_{fg}}{\sigma} r_h \frac{\alpha}{\beta}\right)^m \left(\frac{G^2 r_h}{\rho_l \sigma}\frac{\gamma}{\beta}\right)^n \left(\frac{\mu_l G}{\rho_l \sigma}\right)^o \left(\frac{g\left(\rho_l - \rho_v\right) r_h^2}{\sigma}\frac{\phi}{\alpha}\right)^p \left(\frac{W}{H}\right)^q \left(\frac{T_{in}}{T_{sat}}\right)^r \tag{4.16}$$

Full confinement is not the actual state of CHF. Bubble grows for certain duration before acquiring state of CHF. This time lag is taken care of by finding values of coefficients *m*, *n*, *o*, *p*, *q* and *r* through regression process.

Critical heat flux data are typically either based on a certain transverse base area ($q_{CHF,B}$) [35, 158, 164 – 166] below the channel(s) or on the actual total heat transfer area ($q_{CHF,W}$) [35, 41, 162 – 165, 169] of microchannel(s) as shown in Fig. 4.2. All $q_{CHF,B}$ experimental data are converted in to $q_{CHF,W}$. Top surface of microchannel is assumed perfectly insulated as it is normally covered by toughened glass for easy flow visualization purpose. Hence, relationship between $q_{CHF,W}$ and $q_{CHF,B}$ is given by Eq. (4.17).

$$q_{CHF,W} = q_{CHF,B}\frac{W+W_f}{W+2\eta H} \quad (4.17)$$

Where, η is fin efficiency and in current analysis it is assumed as 0.8.

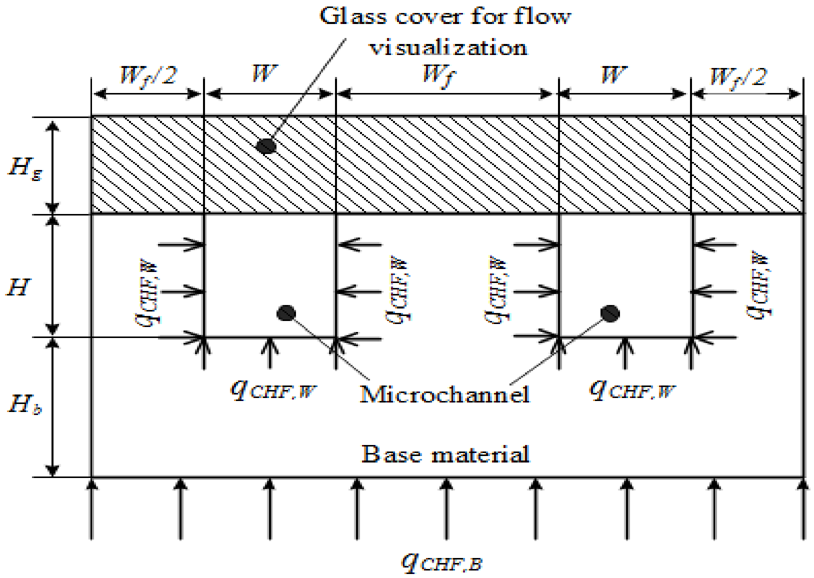

Figure 4.2 Microchannel geometry showing base and wall CHF

4.3 Results and discussion

4.3.1 CHF correlation for refrigerants

Total seven experimental studies were found in open literature which are related to CHF in microchannel and used different refrigerants as working fluids (compiled in Table 2.8). These studies covered refrigerants (R123, R134a, R245fa, R236fa), microchannel of diameters (237 µm < D_h < 1600 µm), mass flux range (84 kg/m^2 s < G < 3736 kg/m^{2}s), inlet subcooling (-1.1 to 60°C) and operating pressure (1.2 < P_{sat} < 13.2). Experimental data from most of the studies were carefully extracted from graphical illustration and, for some cases, data were directly used as they were explicitly available in tabular forms. Experimental studies of Refs. [158, 165, 166] are used in regression analysis for finding value of coefficients *m*, *n*, *o*, *p*, *q* and *r*. Regression of data has been carried out using MATLAB version 7.7.0 (R2008b) regression tool. Equation (4.18) shows the final form of CHF correlation for refrigerants.

$$q_{CHF,W} = 10^6 \left(\frac{\sigma^2}{G r_h^2}\right)\left(\frac{\rho_v h_{fg}}{\sigma} r_h \frac{\alpha}{\beta}\right)^{0.74} \left(\frac{G^2 r_h}{\rho_l \sigma} \frac{\gamma}{\beta}\right)^{-0.28} \left(\frac{\mu_l G}{\rho_l \sigma}\right)^{1.91} \left(\frac{g\left(\rho_l - \rho_v\right) r_h^2}{\sigma} \frac{\phi}{\alpha}\right)^{0.43} \left(\frac{W}{H}\right)^{-0.39} \left(\frac{T_{in}}{T_{sat}}\right)^{-1.41} \tag{4.18}$$

The range of non-dimensional parameters appearing in Eq. (4.18) are:1.8 x $10^4 \le \Pi_{E1} \le 1.5$ x 10^6, 2.4 x $10^{-1} \le \Pi_{E2} \le 3.5$ x 10^2, 1.7 x $10^{-3} \le \Pi_{E3} \le 7.4$ x 10^{-2}, 3.6 x $10^{-3} \le \Pi_{E4} \le 2.6$ x 10^{-1}, 1.1 x $10^{-1} \le W/H \le 6.7$, and 8.3 x $10^{-1} \le T_{in}/T_{sat} \le 1$.

Validity of the newly proposed empirical relation has been checked by comparing it with experimental work of Refs. [158, 162 – 167]. Figures 4.3 – 4.9 show results of comparative analysis between previously proposed equations and current work.

The mean absolute percentage error (MAPE) has been calculated by using Eq. (4.19).

$$\text{MAPE (\%)} = \frac{\sum_{1}^{N} \left| \frac{q''_{CHF,\exp} - q''_{CHF,pred}}{q''_{CHF,\exp}} \right|}{N} \times 100 \tag{4.19}$$

Table 4.2 presents the summary of MAPE in prediction of CHF using present work and existing correlations. In order to compare actual predicting capability of past correlations [35, 162, 171, 100] (developed with fin efficiency of 100%) with present work, CHF prediction through their models are first converted into wall CHF with 80% fin efficiency as given by Eq. (4.20). Then, MAPE of their correlations have been estimated.

$$q_{CHF,\mathrm{W}_{80\%}} = q_{CHF,\mathrm{W}_{100\%}} \left(\frac{W+2H}{W+1.8H}\right) \tag{4.20}$$

It is observed that unlike earlier correlations, proposed correlation shows good agreement with most of the experimental observations. This may be due to the fact that in earlier correlations effect of influencing variables (inertia, surface tension, drag, gravity and evaporation momentum) were presented through combined non-dimensional parameters that did not fully represent independent effects of key thermophysical properties. Figure 4.10 show comparison of complete set of CHF predictions with experimental value obtained for refrigerants.

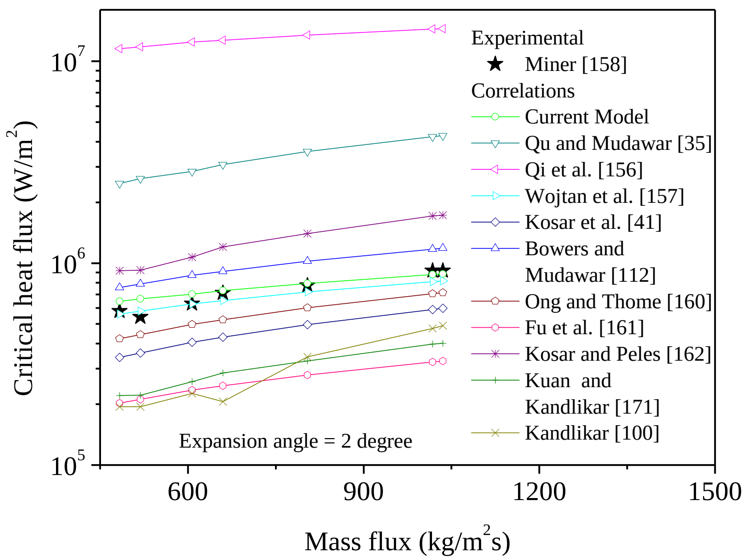

Figure 4.3 Comparison of proposed model with earlier models using experimental data of Miner [158]

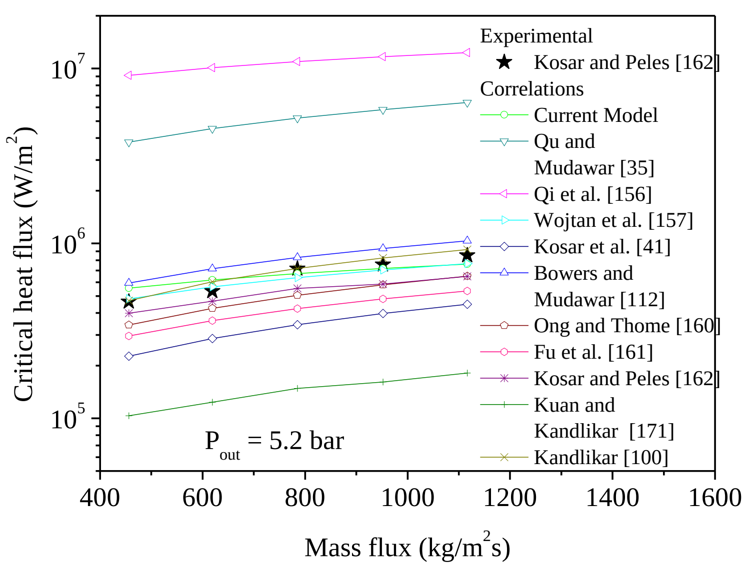

Figure 4.4 Comparison of proposed model with earlier models using experimental data of Kosar and Peles [162]

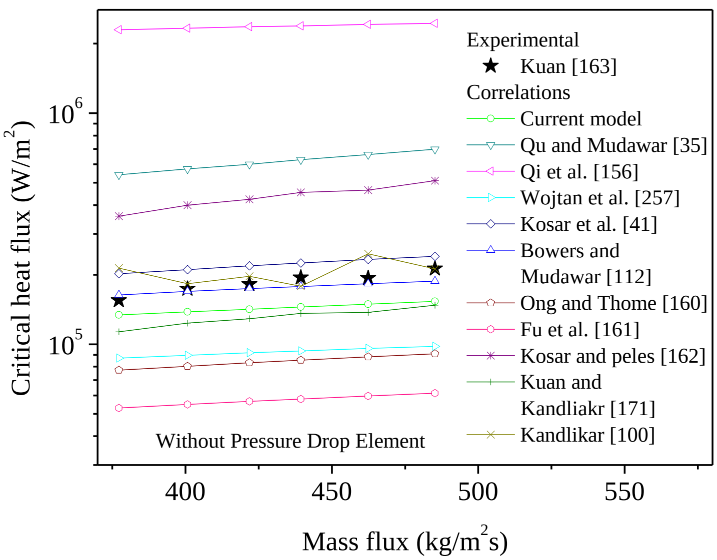

Figure 4.5 Comparison of proposed model with earlier models using experimental data of Kuan [163]

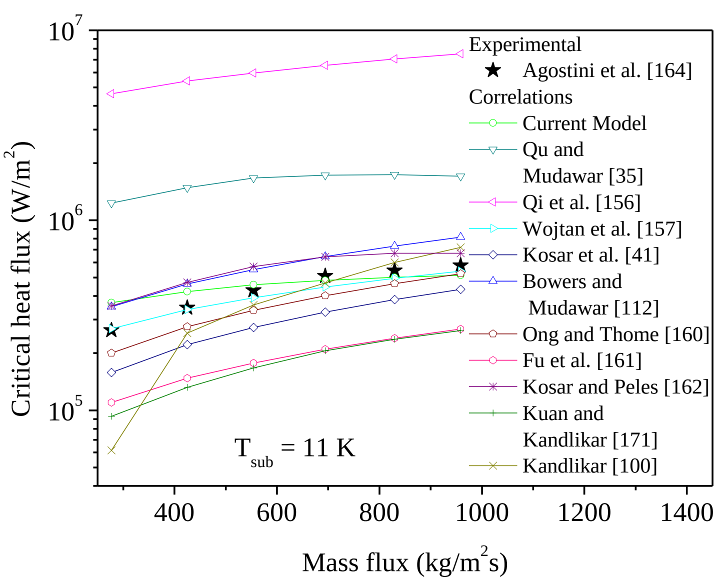

Figure 4.6 Comparison of proposed model with earlier models using experimental data of Agostini et al. [164]

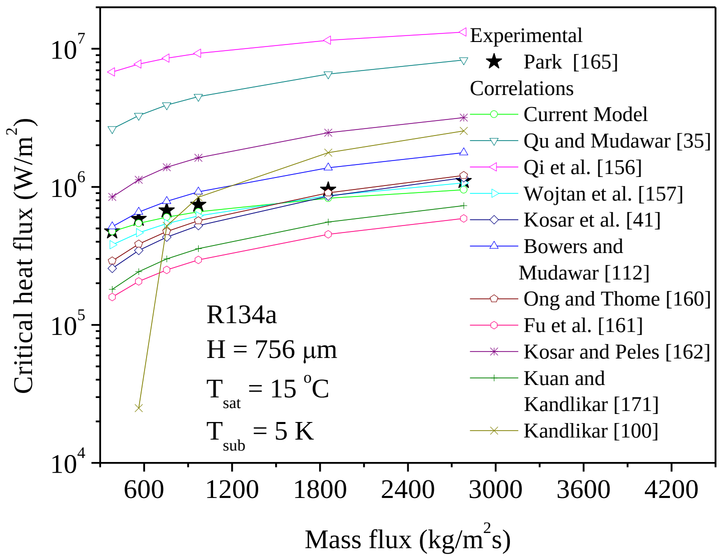

Figure 4.7 Comparison of proposed model with earlier models using experimental data of Park [165]

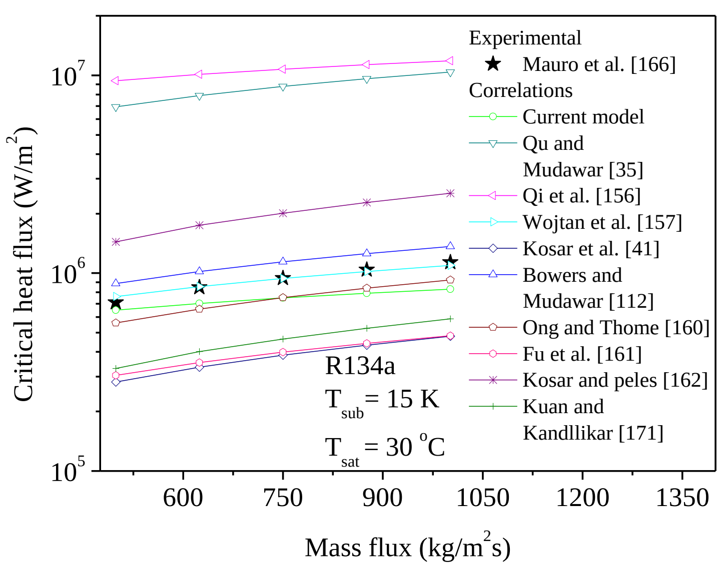

Figure 4.8 Comparison of proposed model with earlier models using experimental data of Mauro et al. [166]

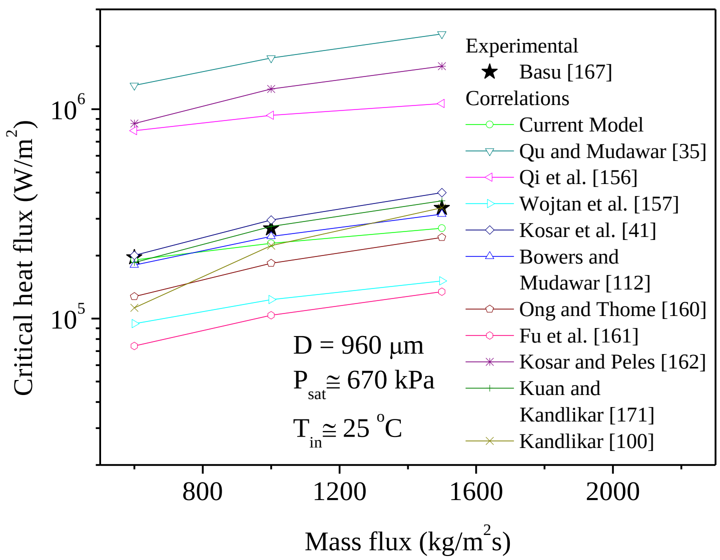

Figure 4.9 Comparison of proposed model with earlier models using experimental data of Basu [167]

Besides, current study (MAPE 21% with 77% data within 30% error band), correlation of Ong and Thome [160] also showed good agreement (MAPE 23% with 74% data within 30% error band) with the available experimental CHF dataset.

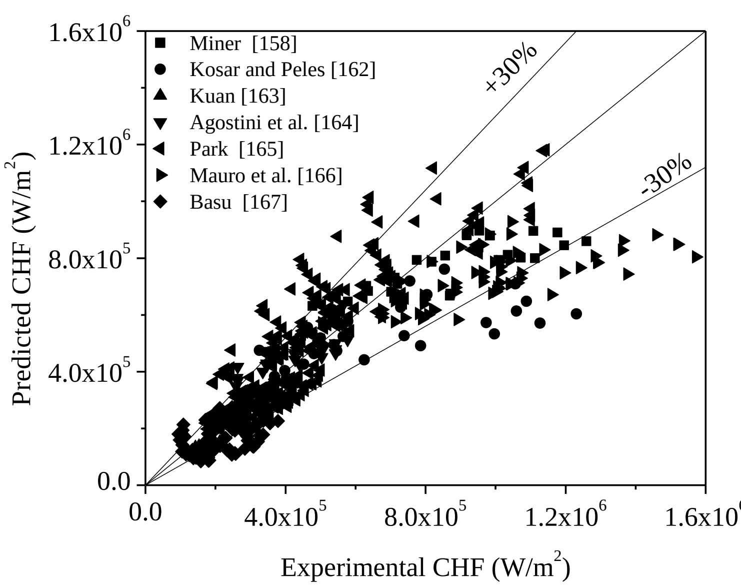

Figure 4.10 Comparison of the experimental CHF and predicted CHF data for refrigerants

Table 4.2

Summary of mean average percentage error (MAPE)

Authors	No. of points U/A	Qu and Mudawar [35]	Qi et al. [156]	Wojtan et al. [157]	Kosar et al. [41]	Bower and Mudawar [112]	Ong and Thome [160]	Fu et al. [161]	Kosar and Peles [162]	Kuan and Kandlikar [171]	Kandlikar [100]	Current model
Miner [158]	26/26	354.6	1571	13.3	35.6	28.7	23.9	61.7	83.2	57.0	50.7	14.9
Kosar and Peles [162]	30/30	445.6	1776	21.3	48.4	32.5	29.9	35.7	15.8	73.9	25.0	20.5
Kuan [163]	8/8	244.8	1260	47.3	24.9	7.9	52.4	67.6	135.6	28.0	30.1	18.5
Agostini et al. [164]	25/25	282.8	1342	7.0	33.8	32.5	18.6	57.1	25.0	59.2	23.3	16.2
Park [165]	323/323	487.9	1204	37.7	47.3	51.2	20.7	57.7	55.1[a,1]	69.1	50.5[b,3]	18.0
Mauro et al. [166]	66/66	636.7	986	9.2	62.9	14.2	22.2	61.1	116.3	53.5	N.A.[b]	24.7
Basu [167] *1	80/111	845.6	265.7	47.5	16.8	11.9	26.6	59.0	232.0[a,2]	22.9	34.5	31.3

Footnote: N.A. Not Applicable, Superscripts: (a cases: CHF –ve), (b cases: x > 1), (1, 2, 3) (13, 29, 52), **1 D = 510µm, (readings left)*

4.3.2 CHF correlation for water

Initially Eq. (4.18) was also checked for CHF data of microchannel using water as working fluid. It is found that CHF condition for water can not be predicted accurately using same value of coefficients – as for refrigerants. This is possibly due to large variations in enthalpy of evaporation and other thermophysical properties that lead to non-dimensional numbers which are well out of the admissible range for Eq. (4.18). Analyzing the thermo-physical properties of water and refrigerants, it is found that, unlike refrigerants, effect of gravity to surface tension (Π_{E4}) on the vapor bubble for the water case can be neglected. Under typical operating conditions considered here, influence of this parameter for the water case is found to be around thirty five times lower than for cases involving refrigerants. Hence, influence of Π_{E4} for the water case has been neglected. Unlike refrigerants, water experimental studies had been carried out for a smaller limited range of mass flux, and there is smaller available data set. For the large mass flux range, from 2000 – 9000 kg/m^{2}s, no experimental data is available in open literature. Hence, experimental readings of all available relevant cases Refs. [35, 41, 163, 168 – 170] have been utilized for finding the values of coefficients *m*, *n*, *o*, *q* and *r*. Current experimental readings cover hydraulic diameter range (133 µm < D_h <1168 µm), mass flux range from (40 kg/m^2 s < G < 1600 kg/m^{2}s), inlet subcooling range of (2 – 132 °C) and operating pressure (0.253 < P_{sat} < 10.47). CHF correlation for the water is given by Eq. (4.21).

$$q_{CHF,W} = 10^6 \left(\frac{\sigma^2}{G r_h^2}\right) \left(\frac{\rho_v h_{fg}}{\sigma} r_h \frac{\alpha}{\beta}\right)^{1.71} \left(\frac{G^2 r_h}{\rho_l \sigma} \frac{\gamma}{\beta}\right)^{-0.92} \left(\frac{\mu_l G}{\rho_l \sigma}\right)^{3.35} \left(\frac{W}{H}\right)^{-0.12} \left(\frac{T_{in}}{T_{sat}}\right)^{-1.61} \tag{4.21}$$

The range of non-dimensional parameters appearing in Eq. (4.21) are: 0.9 x $10^3 \leq \Pi_{E1} \leq 1.6$ x 10^5, 6 x $10^{-3} \leq \Pi_{E2} \leq 2.8$ x 10^1 and 2 x $10^{-4} \leq \Pi_{E3} \leq 1$ x 10^{-2}, 2.6 x $10^{-1} \leq W/H \leq 6.7$, and 7.1 x $10^{-1} \leq T_{in}/T_{sat} \leq 1$.

Figures 4.11 – 4.16 show comparative analysis of the previously proposed correlations and current correlation for water. Summary of MAPE of current and previous correlations are reported in Table 3.3.

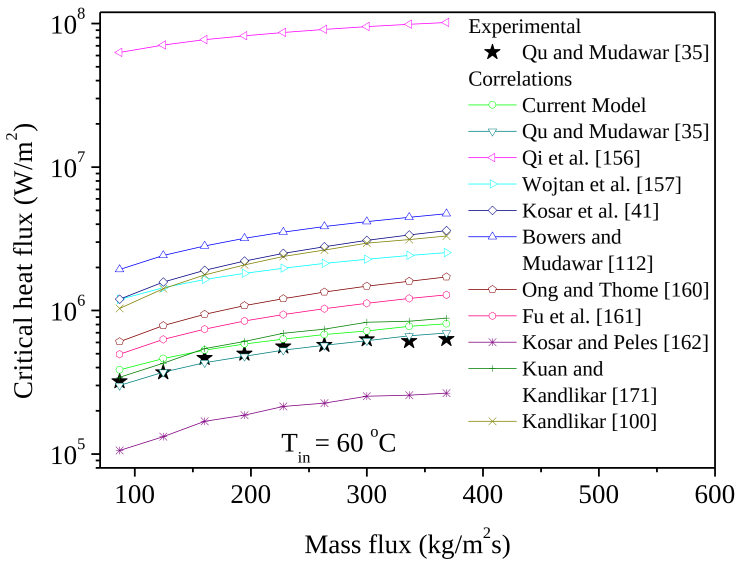

Figure 4.11 Comparison of proposed model with earlier models using experimental data of Qu and Mudawar [35]

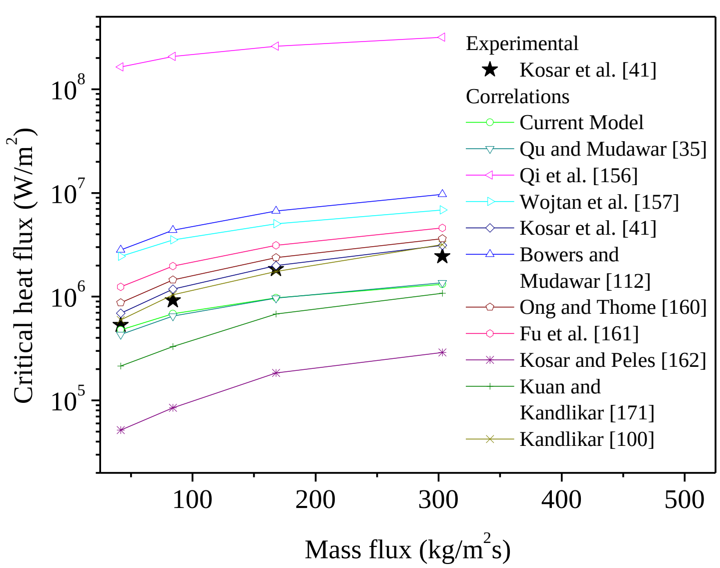

Figure 4.12 Comparison of proposed model with earlier models using experimental data of Kosar et al. [41]

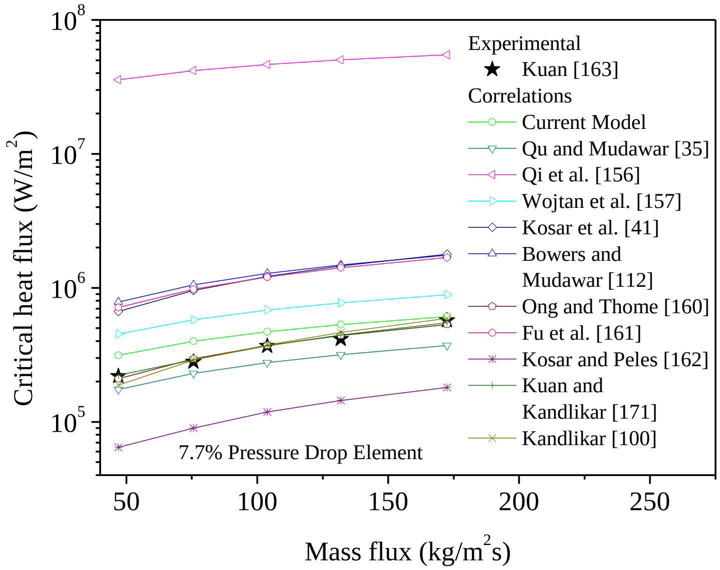

Figure 4.13 Comparison of proposed model with earlier models using experimental data of Kuan [163]

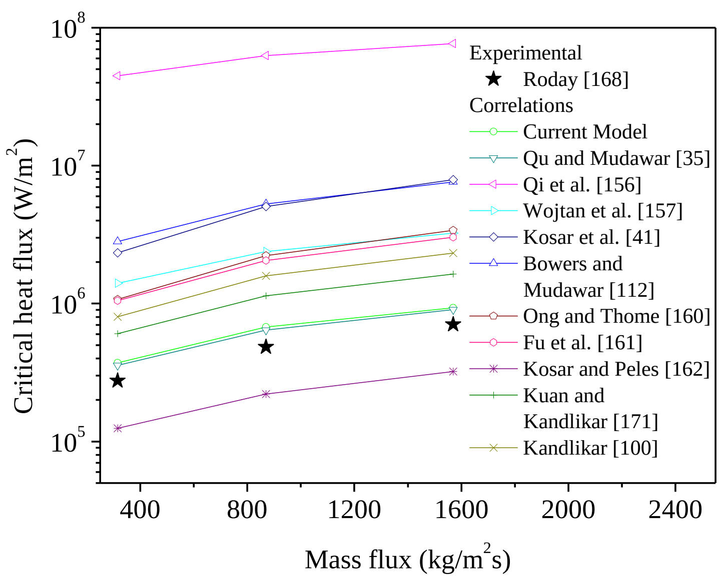

Figure 4.14 Comparison of proposed model with earlier models using experimental data of Roday [168]

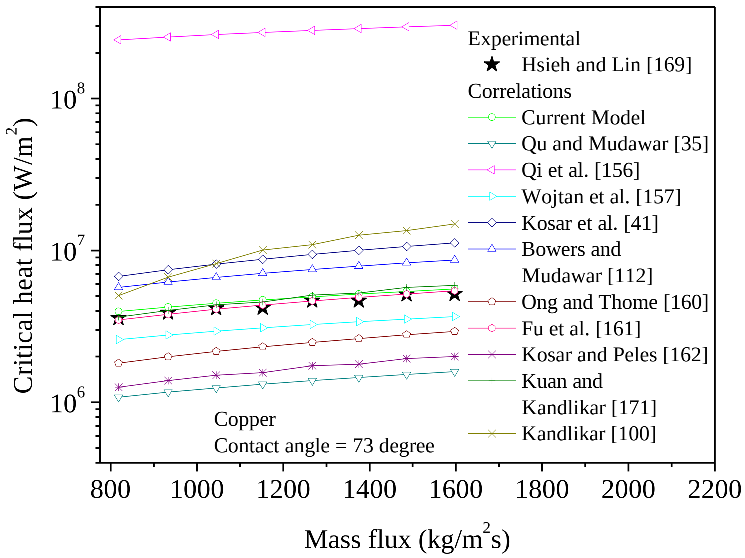

Figure 4.15 Comparison of proposed model with earlier models using experimental data of Hsieh and Lin [169]

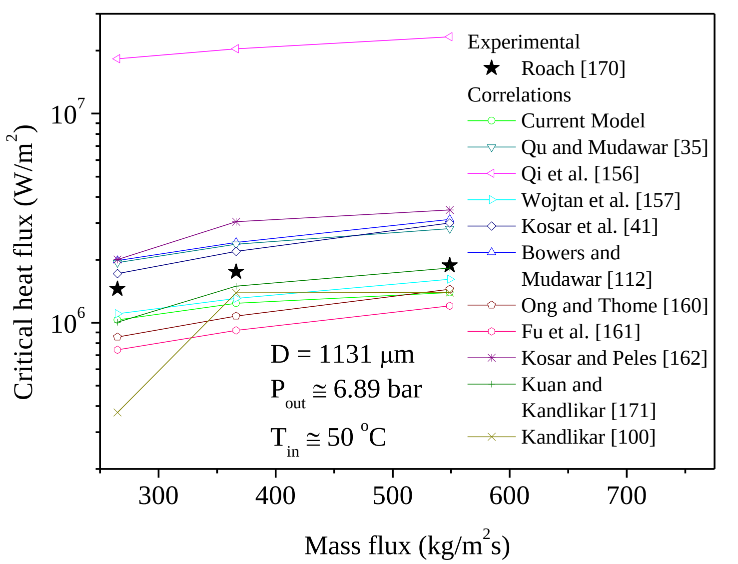

Figure 4.16 Comparison of proposed model with earlier models using experimental data of Roach et al. [170]

Prediction capability of water correlation is found to be poorer than the refrigerant. Only 60% experimental data are found to fall within error band of 30% as shown in Fig. 4.17. This may be due to effect of significant unaccounted heat loss to the atmosphere in case of water – unlike refrigerants. However, still the prediction of current correlation is better in comparison to previous existing correlations. The MAPE of current correlation for water case is found to be around 27%.

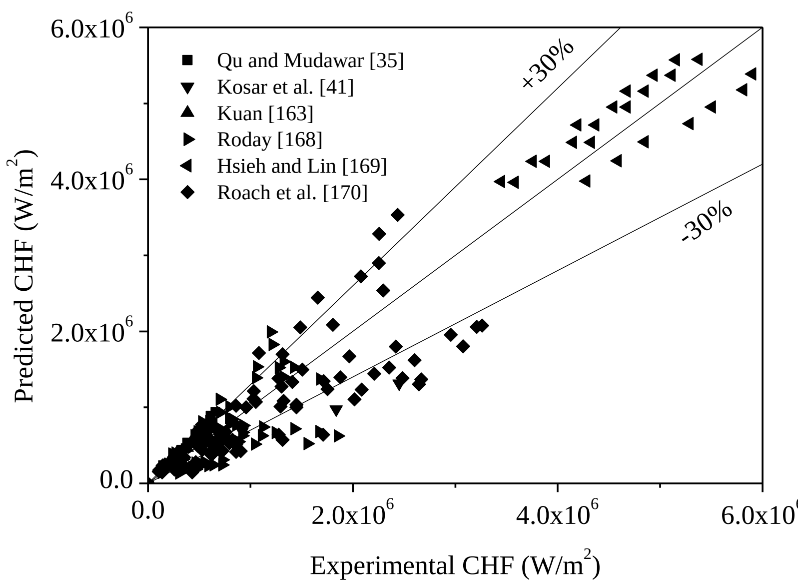

Figure 4.17 Comparison of the experimental CHF and predicted CHF data for water

Table 4.3

Summary of mean average percentage error (MAPE)

Authors	No. of points U/A	Qu and Mudawar [35]	Qi et al. [156]	Wojtan et al. [157]	Kosar et al. [41]	Bower and Mudawar [112]	Ong and Thome [[160]	Fu et al. [161]	Kosar and Peles [162]	Kuan and Kandlikar [171]	Kandlikar [100]	Current model
Qu and Mudawar [35]	18/18	5.2	16537.0	270.9	363.6	556.4	125.1	74.7	63.8	19.0	321.1	25.9
Kosar et al. [41]	4/4	37.2	19383.6	237.6	18.8	325.6	43.9	94.0	89.2	58.3	19.0	32.2
Kuan [163]	11/11	25.6	12589.3	84.5	227.5	244.9	4.5	224.5	68.1	3.1	8.54	26.0
Roday [168]	76/136	54.07	1322.7	345.6	811.4	908.9	326.3	297.4	58.4[a,1]	92.1	110.4	31.5
Hsieh and Lin [169]	24/24	71.3	5809.2	32.6	91.6	54.2	49.3	6.9	63.6	6.6	105.9[b,2]	8.8
Roach et al. [170] *1	42/72	72.3	1216.5	21.2	56.6	68.9	25.2	35.05	85.9	11.7	32.5[b,3]	31.5

Footnote: N.A. Not Applicable, Superscripts: (a cases: CHF –ve), (b cases: x > 1), (1, 2, 3) (22, 2, 7), **1 D =1448 µm (readings left)*

4.4 Limitations of current model

Current model has been developed based on the assumption that instability due to bubble confinement stimulates the condition of CHF in microchannel. Proposed correlations strongly justified experimental observations of parallel microchannel heat sink; whereas MAPE is found to be on slightly higher side (~32%) for single microchannel (circular tube) experimental cases [167, 168, 170]. Current limitation is in line with the finding of past researchers. Bergles and Kandlikar [131] noted that CHF in parallel microchannel is due to the result of excursive instability rather than conventional dryout mechanism. Influence of confinement on CHF is expected to decrease with increase in channel diameter and mass flux. Therefore, proposed correlations showed large deviation from experimental values obtained at high mass flux (G) values in microchannels [201, 202]. Similarly, unlike the past correlations of [160] and [100] , which capably estimated CHF conditions for both mini and microchannel flows, large deviation of around 80% is found when proposed correlation for water is tested against experimental values for minichannels [203, 204]. However, as key non-dimensional numbers remain approximately the same, the reported limitations can be minimized by separate implementations of this scheme for data covering high mass flux flows in micro- and minichannels.

4.5 Conclusion

In the current study, new semi-empirical CHF model for microchannel has been developed. This assumes vapour bubble blockage mechanism of CHF and associated experimental data set. A non dimensional analysis and energy based bubble growth model at nucleation site are used to develop the models.

1. Two separate CHF correlations have been proposed to estimate CHF values for refrigerants and water. The correlation for refrigerants show good agreement with almost all experimental studies and predicts 77% data within error band of 30%.

2. Whereas, correlation for water predicts only 60% of available data within error band of 30%. The MAPE of refrigerant and water are 21% and 27% respectively.
3. It is also found that influence of energy ratio term Π_{E4} (gravity to surface tension) on water CHF condition can be neglected.
4. Superior prediction ability of current CHF model can be attributed to its dependency on all independent parameters relevant to bubble dynamics. Proposed model can help in advancing current state of art of CHF studies pertaining to microchannel strictly.

CHAPTER 5

EXPERIMENTATION ON HEAT TRANSFER AND PRESSURE DROP CHARACTERISTICS OF OPEN MICROCHANNEL AND ITS PERFORMANCE AUGMENTATION

5.1 Introduction

Use of flow boiling in microchannel heat sink meets high heat dissipation requirements compared to single phase flow. However, flow boiling in microchannels is prone to high pressure drop and subjected to the flow instabilities like parallel channel instability [109], pressure fluctuation [205], vapor blocking [128] and flow reversal [35, 131, 132] which leads to CHF [35, 131, 206]. Hence, researchers are engaged in an effective implementation of single phase flow with enhanced heat transfer techniques to tackle with high heat dissipation problem. Generally, this technique involves modifications in microchannel geometry like wavy microchannel [115], double-layer wavy microchannel [207], diverging microchannel [120, 143], converging-diverging microchannels [208] etc. Steinke and Kandlikar [29] speculated that single phase flow in microchannel with enhancement techniques can compete with flow boiling in microchannel. Also, an attempt has been made for heat transfer enhancement using nano fluid as working fluid [210, 211]. However, Wang et al. [212, 213] concluded that use of nano fluid does not always offer superior heat transfer performance over water.

Kandlikar et al. [214] and Kalani and Kandlikar [215] studied flow boiling in open type microchannel heat sink. Kandlikar et al. [214] observed that open type microchannel heat sink helps in reducing the flow reversal. They further observed that heat transfer performance is influenced by depth of the gap. Kalani and Kandlikar [215] observed tremendous reduction in the pressure drop in open type microchannel heat sink than plain microchannel heat sink. From the open literature, it is observed that single phase flow with open type microchannel heat sink has not been studied. Recently, Yadav et al. [216] carried out numerical simulation of single phase flow in microchannel with fins inside the microchannel. Three configurations of extended fins in microchannel (upstream finned microchannel, downstream finned microchannel and complete finned microchannel) are compared with plain rectangular microchannel. They concluded that introduction of the fins in all three configuration helps in enhancing the thermal performance of the microchannel compared to plain microchannel. Further, they observed that overall performance of the upstream finned microchannel is better than downstream finned microchannel and complete finned microchannel. This is attributed to the higher heat transfer potential due large temperature difference between inlet temperature and wall temperature in upstream part of the microchannel than downstream part. However, no experimental evidences have been found in the open literature which addresses single phase flow in microchannel heat sink having fins. Hence, in this chapter, attempt has been made to perform experiments with open type microchannel heat sink and its performance augmentation using fins. For this purpose, two configuration of the microchannel heat sink are fabricated; (1) microchannels without fins (2) microchannels with fins. The development of the experimental set up and performance comparison of these configurations is discussed in this chapter.

5.2 Experimental set up

Fig. 5.1 shows the schematic diagram of the open loop experimental setup used in order to study open type microchannel heat sink. Actual apparatus is shown in the photograph in Fig 5.2. Experimental set up is developed keeping in mind the interchangeability of the microchannel heat sink. Water is stored and supplied from the inlet tank. Micro annular gear pump is used to circulate the water through filter. The speed of the pump is controlled, to achieve different flow rates, via variable speed gear pump drive. Flow rate is measured using mass flow meter which is installed after pump. Subsequently, water is preheated in preheater to achieve required constant inlet temperature, measured at outlet of the preheater, throughout the experimentation. Flow passage between preheater and test section is insulated in order to reduce heat loss to environment. Inlet and outlet fluid temperatures, using K type thermocouples, are measured at inlet and outlet plenum of the microchannel heat sink. Four K type thermocouples are placed at the bottom of the microchannel heat sink to measure the base temperature. Five cartridge heaters are used to heat test section and its power is controlled, to facilitate different heat flux conditions, with help of the auto transformer. Inlet and outlet pressure is measured with help of the pressure transducer. The signals of the thermocouples, pressure transducers and mass flow meter are collected with help of high speed data acquisition system. Details of the equipments used in the current experimentation are discussed in following section.

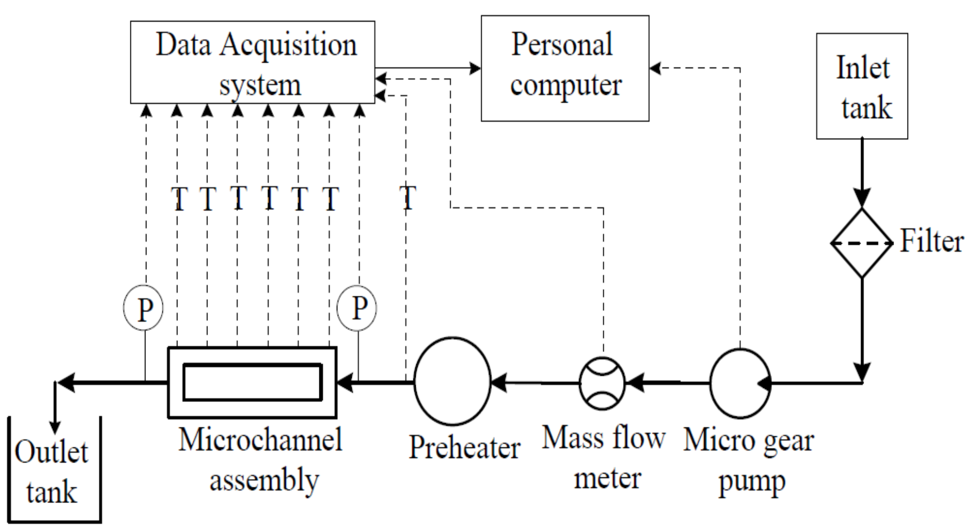

Figure 5.1 Experimental set up

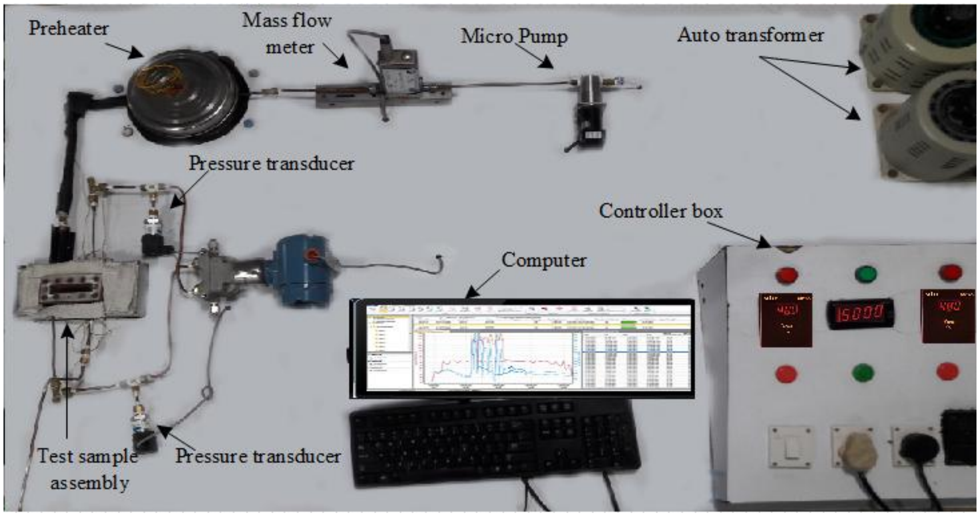

Figure 5.2 Photographic view of experimental set up

5.2.1 Equipments detail

Following is the details of the equipments used while performing the experiments. These equipments are presented in sequence as per their use in the set up.

Inlet tank: Inlet tank is made of the stainless steel having storage capacity of 50 liter of the water. This tank is placed before the filter.

Filter: Inline filter is used which prevent any solid particle present in flowing fluid from blocking the microchannels. The filter (Cole-Parmer) is housed in a transparent casing that can help to visualized degradation of the filter cartridge. The cartridge, which is easily replaceable and readily available, is 10 inch in length with diameter of 2.5 inch. The pore size of the cartridge is 10 μm.

Pump: A positive displacement, micro-gear pump drives the flow through the loop. The gear pump (mzr-7205, HNP mycrosystem) delivers flow from 0.047 to 288 ml/min at a maximum pressure of 32 bars. This type of pump is chosen to give a constant flow rate at the test section inlet regardless of the pressure drop occurring in it. The micropump is selected because of its accuracy of flow rates, ability to dispense small volumes, and its small footprint.

Flow meter: Flow is measured with help of coriolis mass flow meter (M14-AGD-22-0-S, BRONKHORST CORI-Tech). This flow meter is capable to measure flow rate between 10 ml/min to 500 ml/min and placed in between pump and preheater. Care has been taken while installing the mass flow meter that the inlet length (=0.05**Re**Diameter of inlet pipe) should be sufficient to insured hydraulically developed flow enters the flow meter. The flow meter is calibrated and it has an accuracy of less than 2% over entire range of the flow rate (discussed in Appendix C.1).

Preheater: Liquid enters the microchannel heat sink through preheater. The preheater is used to maintain inlet fluid temperature near ≈ 30 °C. The coil is formed using cooper tube of 5 mm outer and 3 mm inner diameter and immersed into the oil tank. The required temperature of the inlet fluid to microchannel is measured at outlet of the preheater ($T_{in,\ elbow}$). The power of the preheater is controlled through PID controller.

Pressure transducer: Two pressure transducers are used to measure inlet and outlet pressure across microchannels. These are OMICRON (U3221-6-001BC) made having range of ±0.5 bar with an accuracy of ±0.1%.

Thermocouples: K type thermocouples are used for all temperature measurements. The thermocouple wire has diameter of the 100 micron. The beads of the thermocouples are formed using bead making machine at the Raja Ramanna Centre for Advanced Technology (Indore, Madhya Pradesh, India). Thermocouples are calibrated and found an accuracy of ±0.59 °C (discussed in Appendix C.2).

Data acquisition system: Agilent (34792A) made data acquisition system is used to collect information of the thermocouples, pressure transducers and mass flow meter readings. This data logger is coupled with personal computer to record and store the information.

Heaters: Five cartridge heaters are used having capacity of 250W each. The diameter and length of the heater are 10 mm and 50 mm, respectively.

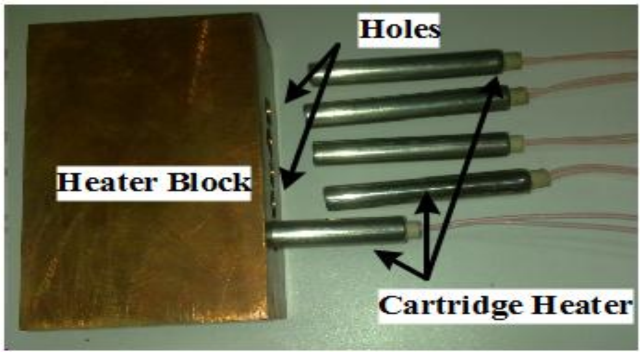

Figure 5.3 Heater block with cartridge heaters

These heaters are inserted into the copper block as shown in Fig. 5.3 which acts as heat source during the experimentation.

Glass: Top surface of the microchannel heat sink is covered with transparent glass for flow visualization purpose. In current study, heat resistance glass (≈1000 °C) is used to cover the top surface. The glass has length of 105 mm, width of 55 mm and thickness of 10 mm. The glass has 12 holes of 6 mm diameter which are used for tightening purpose.

5.2.2. Test section

Two configurations of the microchannel heat sink are fabricated. One is with fins fabricated inside microchannels along half length and other configuration is without fins. Figure 5.4 shows the microchannel test sample. Each microchannel heat sink has 16 microchannels. Microchannel heat sink consists of inlet and outlet plenum. Microchannels are fabricated in between inlet and outlet plenum. Both plenums are rectangular in shape having width of 13 mm, length of 10 mm and 6.5 mm in depth. Each plenum has two holes, one acts as port to facilitate flow of the flowing fluid having 5 mm diameter through which 3 mm internal diameter tube is inserted. Other hole is for the temperature and pressure measurements having diameter of 3 mm through which 2 mm internal diameter tube is inserted. The thermocouple is inserted through tube and also connection is given to the pressure transducer. Four holes of 2 mm diameter are drilled from the bottom of microchannel heat sink as well as from the side. The length of these holes is such that the side hole opens at base of the bottom hole and vice versa. The side and bottom holes are at distance of 10 mm from the inlet of the microchannels and 10 mm apart along the length.

In both samples, microchannels are 50 mm long and their dimensions are given in Table 5.1. A 100 µm diameter circular fins are fabricated in half length of the microchannels. The first fin is 2 mm away from the inlet of the microchannel and distance between two fins is 4mm. There are seven fins in each microchannel, thus total number of fins are 112. Figure 5.5 shows schematic of both configurations, with and without fin microchannel heat sink.

Table 5.1

Geometrical parameters of the test section

Geometry	**N**	**W_c (µm)**	**W_w (µm)**	**H_c (µm)**	**L_c (mm)**	**D_h (µm)**	**No.of fins (N_f)**	**D_f (µm)**	**H_f (µm)**
Without fins	16	314	289	295	50	304	0	-	-
With fins	16	320	274	310	50	315	112	100	310

5.2.3 Microchannel assembly

Copper substrate over which microchannels are fabricated, have ten threaded holes (five on either side of microchannel along the length) as shown in Fig. 5.4. A glass cover is placed over the microchannel heat sink and is fastened with 10 bolts.

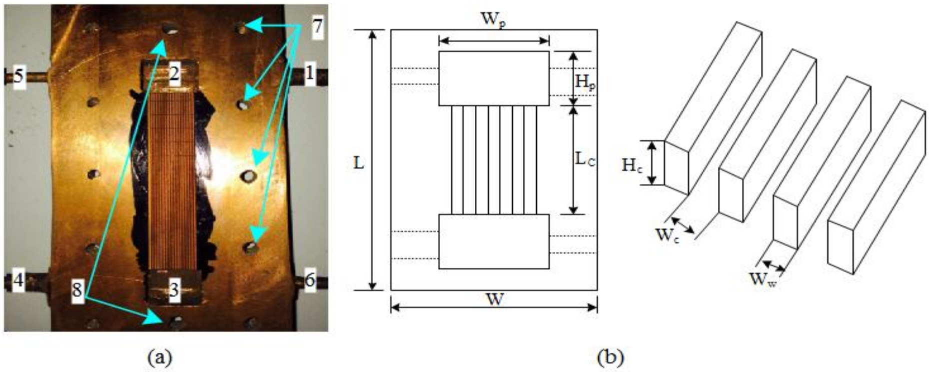

Figure 5.4 Actual photograph of the test sample. (1) Inlet port, (2) Inlet plenum, (3) Outlet plenum, (4) Outlet port, (5) Inlet temperature and pressure port, (6) Outlet temperature and pressure port, (7) Holes for fastening glass, (8) Holes for fastening sample with heater block

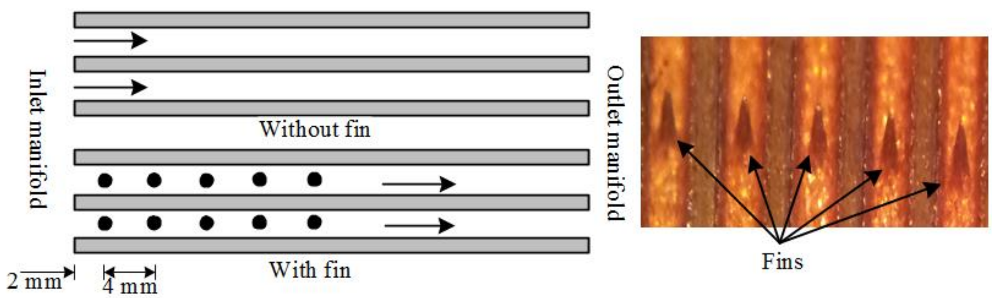

Figure 5.5 Schematic of microchannel heat sink with and without fins

Thin layer of adhesive is form on the heat resistance glass. This layer is 390 µm and 392 µm thick (H_g) respectively for the microchannel without fins and microchannels with fins. Portion of the adhesive layer above the microchannels is removed to achieve gap above microchannels. An assembly of microchannel heat sink with glass is placed over the top of heater block (heat source). Microchannel heat sink with glass cover holds against heat source through two bolts. In order to have proper thermal contact between microchannel heat sink and heater block, silicone based thermal paste is applied at its junction. Complete parts of the assembly of the microchannel heat sink are shown in Fig. 5.6. Figure 5.7 (a) and (b) shows the sectional view of the open type and closed type microchannel heat sink and glass assembly.

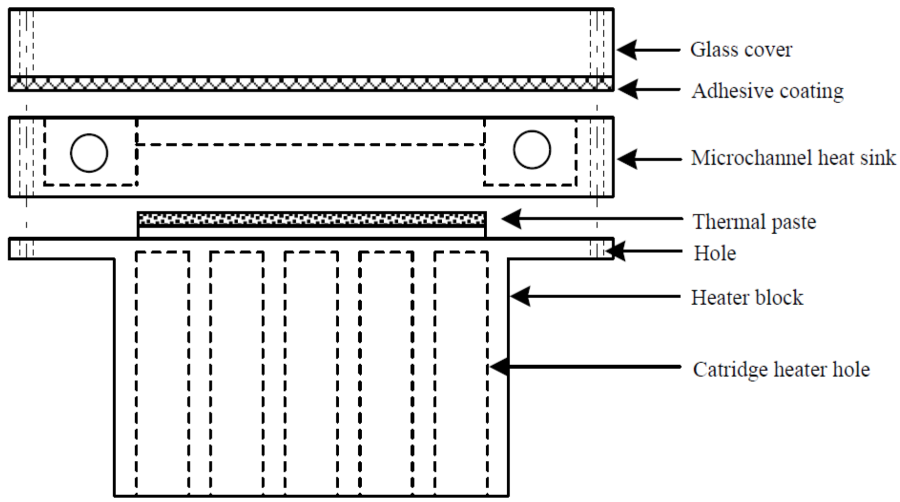

Figure 5.6 Complete assembly of the microchannel heat sink

Such geometry of the microchannel heat sink is called as open type microchannel heat sink [214, 215]. Considering the gap, hydraulic diameter of the microchannel heat sink without fins and with fins are 711.9 μm and 711.6 μm respectively. The values of the confinement number for current experimental observations are found to vary between 3.72 to 3.79 for both configurations, which satisfies the criteria of the microchannel. This assembly is placed into the box which is filled with insulation to reduce heat loss to the environment and only top portion of the microchannel heat sink is exposed to the atmospheric environment.

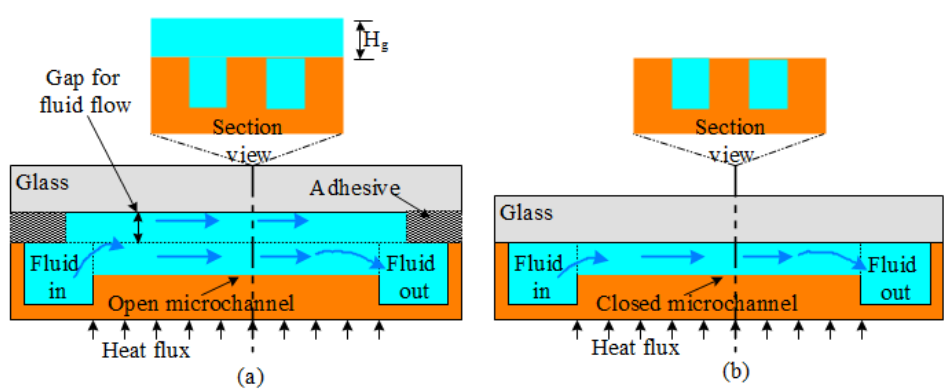

Figure 5.7 Open and closed type microchannel heat sink

5.2.4 Problems associated with experiments and their solution

5.2.4.1 Side flow

Initially, microchannels were fabricated at the top flat surface and glass was tightened over it. But, this assembly had problem of the side leakage. In next stage, side portion of the microchannels in rectangular shape were machined to depth of 1.5 mm. In this modification, steps were formed such that microchannels appear on the top of steps as shown in Fig. 5.8 (a). The silicone sheet is used as gasket around the step. The problem of the side leakage was overcome but problem of the side flow over step was faced as shown in Fig. 5.8 (b).

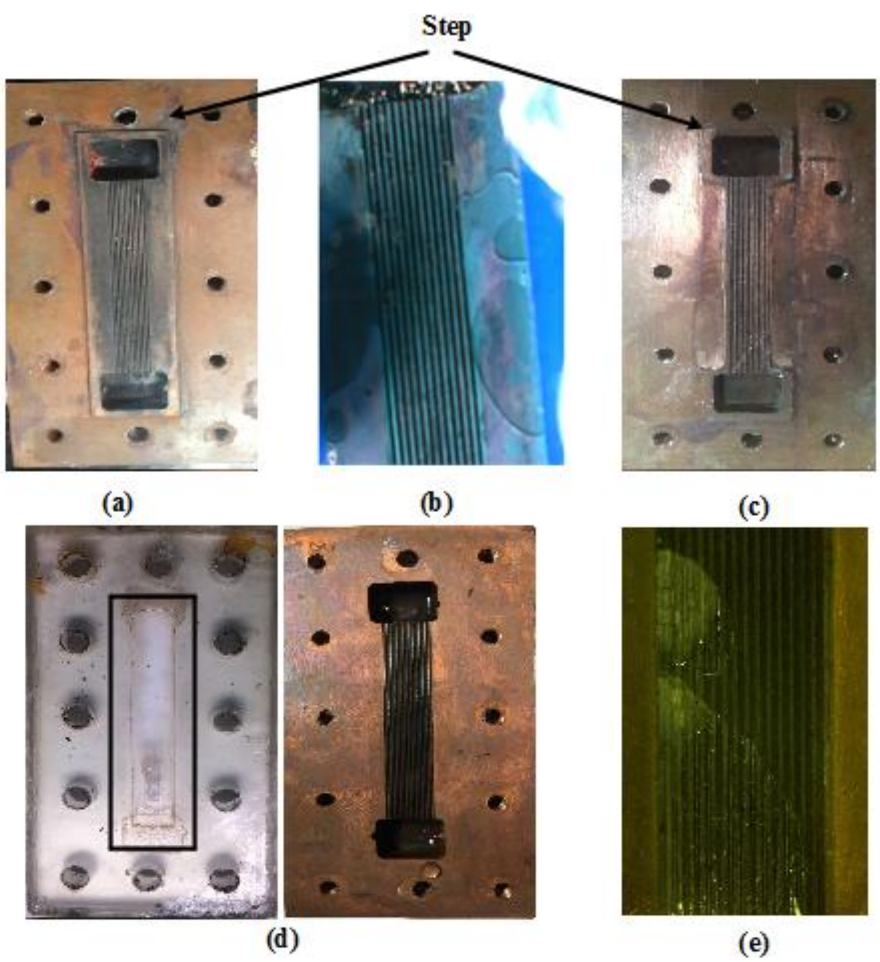

Figure 5.8 Modifications in the test sample

There was liquid flow from the side portion of the step along with microchannel. To resolve this issue, additional material from steps fabricated in the previous stage is removed such that step is around 2 mm away from the microchannels and plenums as well as from the plenums as shown in Fig. 5.8 (c). At this stage even, side flow issue could not be resolved completely. There was flow of the liquid over side portion of 2 mm. In order to mitigate this issue completely, step fabricated in second stage was machined and microchannels were fabricated over flat surface as done in the first stage. The thin film of the adhesive was formed over heat resistance glass and portion of this film which appears over the microchannels was removed. The modification of the sample and glass made in this stage is shown in Fig. 5.8 (d). This modification helps in removing the side flow issue completely. There is flow of fluid through and above microchannels as shown in Fig. 5.8 (e).

5.2.4.2 Inlet and outlet temperature measurement

Inlet and outlet temperature of the fluid is measured at inlet and outlet plenum respectively. K type thermocouples are inserted in the plenum through holes drilled into inlet and outlet plenum. These thermocouples tips are placed at approximately center of the plenum. Initially, length of the bared surface of the thermocouples and the temperature captured by them were closer to bottom wall temperature. This may be due to the touching of the microchannel heat sink wall by the bare surface of thermocouple as shown in Fig. 5.9 (a). Hence, the length of the bare surface of thermocouple is reduced to remove this problem as shown in Fig. 5.9 (b).

5.2.4.3 Base temperature measurement

Four thermocouples are placed at the bottom of the test sample to measure the base temperature. Initially, slots were manufactured as shown in Fig. 5.10 (a) to locate the thermocouple but it was difficult to hold their tip at proper location. Thus, thermocouples were not shown correct temperature of the base. In next step, 2 mm holes are drilled from bottom side of samples as shown in Fig. 5.10 (a).

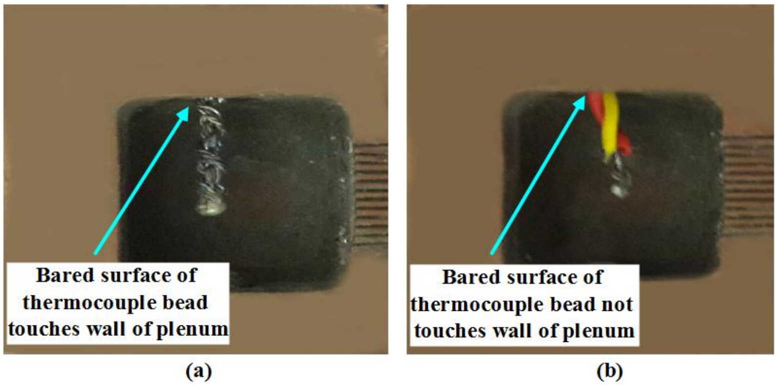

Figure 5.9 Position of the thermocouple in plenum

But, similar problem of holding the tips was faced as faced in previous step. In order to mitigate this issue, 2 mm side holes (as shown in Fig. 5.10 (b)) were drilled to insert the thermocouple. The length of these holes is such that the side hole opens at base of the bottom hole and vice versa. For proper holding of the tip, thermocouples are inserted through side holes, cotton is filled and pressed tightly into the bottom holes. This arrangement helps in holding the thermocouples properly to its position and giving accurate reading of the base temperature.

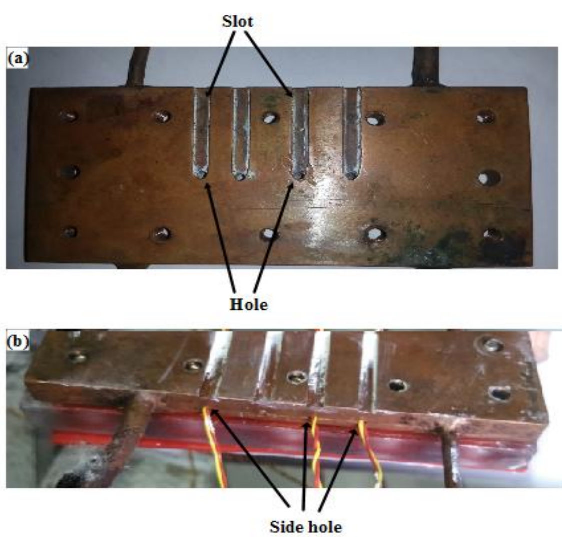

Figure 5.10 Position of the thermocouple inserted in to side wall

5.2.5 Experimental procedure

Before initiating the experiments, inlet tank is filled with water, all electric connections are checked properly and power supply of set up is switched on. Following experimental procedure is followed in current experimentation:

1. Initially pump is activated and required flow rate is set.
2. Inlet temperature (≈30°C) of the flowing fluid for set flow rate is adjusted by controlling the power of the preheater.
3. The power supply of the cartridge heaters is switched ON and required voltage value is set after inlet temperature is stabilized.
4. Around 20 – 22 minutes are required to reach steady state in each run. The temperatures, pressures and mass flow meter information is logged at interval of 10 seconds and averaged of the last 2 min in each run is used for calculation purpose.
5. The heat flux is then increased by increasing the voltage supplied to the heater. Then procedure 4 is repeated.
6. Next flow rate is applied and procedure 2 – 5 is repeated.

After finishing set off experiments, heater supply is shut down and allows water flow to cool test sample. After achieving temperature close to atmosphere, pump is stopped and power supply of complete set up is switched off. Total five different voltage settings are applied to cartridge heater for single flow rate and five flow rates are studied in current analysis. Detailed information of the voltage settings and flow rates conditions used in current study are presented in Table 5.2. This combination of the mass flow rate and applied voltage gives mass flux range (G) 157 – 754 kg/m^{2}s, Reynolds number (Re) 149 – 854, effective heat flux ($q''_{eff,ht}$) 6.12 – 246 kW/m^2.

Table 5.2

Details of mass flow rates and applied voltage

Sr. No.	Mass flow rate (ml/min)	Voltage (V)
1	50	25, 45, 50, 65, 75
2	100	25, 50, 65, 75, 100
3	150	25, 50, 75, 100, 125
4	200	25, 50, 75, 100, 125
5	250	25, 50, 75, 100, 125

5.2.6 Data reduction

Following data reduction process is adopted for an analysis. Heat carried away by water i.e. sensible heat is calculated by Eq. (5.1) given below,

$$q_{eff} = \dot{m} C_p \left(T_{out} - T_{in} \right) \tag{5.1}$$

Where, $\dot{m}$ is mass flow rate of the liquid, T_{in} and T_{out} indicates liquid temperature at inlet and outlet of the microchannels and C_p is specific heat of liquid. Thermophysical properties of the water are taken at mean bulk temperature of the fluid that is average of the inlet and the outlet temperatures and is given by Eq. (5.2).

$$T_{bulk} = \frac{T_{out} + T_{in}}{2} \tag{5.2}$$

An effective heat flux is determined by Eq. (5.3) based on base area.

$$q''_{eff,b} = \frac{q_{eff}}{A_b} \tag{5.3}$$

Where, A_b is footprint area of the copper block on which microchannels are fabricated and given by Eq. (5.4).

$$A_b = W_g L = \left[N\, \mathrm{W_C} + (N-1)\, \mathrm{W_w} \right] L \tag{5.4}$$

Similarly, effective heat flux is calculated (Eq. (5.5) based on actual area of microchannel in contact with fluid.

$$q''_{eff,ht} = \frac{q_{eff}}{A_{ht}} \tag{5.5}$$

Where, A_{ht} is actual heat transfer area of the microchannels and given by Eq. (5.6).

$$A_{ht} = N(W_C + 2H_C)L + (N-1)W_w L - N_f A_{c/s,f} + \eta_f N_f A_{s,f} \tag{5.6}$$

Where, N_f, $A_{c/s,f}$ (=$\pi/4D_f^2$), $A_{s,f}$ (=$\pi D_f H_f$) and η_f are number of fins, cross section area of fin, surface of fin and fin efficiency. For microchannel without fins, N_f is zero.

Average single phase heat transfer coefficient is determined based on actual heat transfer area as given by Eq. (5.7),

$$h_{sp} = \frac{q''_{eff,ht}}{\left(T_w - T_{bulk}\right)} \tag{5.7}$$

Where, T_w is measured from the thermocouple placed at bottom of microchannel as follows. Four thermocouples are placed at the bottom microchannel at distance of b (b =1.72 mm and 1.14 mm for microchannel without fins and microchannel with fins, respectively) as shown in Fig 5.11.

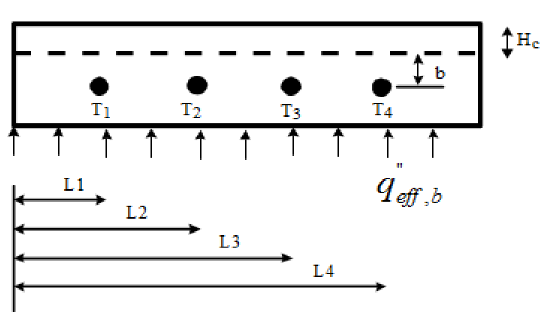

Figure 5.11 Thermocouple position

Considering the one dimensional heat conduction, T_w is measured using Eq. (5.8).

$$T_w = T_{ave} - \frac{q''_{eff,b} \cdot b}{k} \tag{5.8}$$

Where, T_{ave} is average temperature of the four thermocouples, $T_{ave} = \left(T_1 + T_2 + T_3 + T_4\right)/4$, k is thermal conductivity of the copper.

As fins are fabricated inside the microchannel, it is important to calculate the fin efficiency and it is given by Eq. (5.9).

$$\eta_f = \frac{\tanh(mH_f)}{mH_f} \tag{5.9}$$

Where m is fin parameter and given by Eq. (5.10).

$$m = \sqrt{\frac{h_{sp}(\pi D_f)}{k_c A_{c/s,f}}} \tag{5.10}$$

Eqs. (5.7 and 5.9) are solved by iterative method for h_{sp} and η_f. Fin efficiency is varies between 96.5% – 98.4% depending upon operating conditions.

The average Nusselt number (N_u) is calculated based on the average heat transfer coefficient as given by Eq. (5.11).

$$Nu = \frac{h_{sp} D_h}{k_f} \tag{5.11}$$

Where k_f is the liquid thermal conductivity correspond to bulk temperature and D_h is hydraulic diameter and given by Eq. (5.12).

$$D_h = \frac{4A_{c/s}}{P} = \frac{4\left(NW_c H_c + H_g W_g\right)}{N(W_c + 2H_c) + (N-1)W_w + 2H_g + W_g} \tag{5.12}$$

Mass flux (G) is calculated by Eq. (5.13).

$$G = \frac{\dot{m}}{NA_{ch}} \tag{5.13}$$

Where, A_{ch} is microchannel cross section ($NW_c H_c + W_g H_g$).

The Reynolds number is expressed as follows:

$$\mathrm{Re} = \frac{GD_h}{\mu} \tag{5.14}$$

Where, μ dynamic viscosity of the fluid corresponds to bulk temperature. Uncertainties associated with different variables parameter (calculations are presented in Appendix C.3) are presented in Table 5.3.

Table 5.3

Uncertainties in estimated parameter

S No.	Measurement	Uncertainty
1	Gap width (W_g)	2.8%
2	Heat transfer area (A_{ht})	5.7%
3	Effective heat flux (q''_{ht})	17.2%
4	Heat transfer coefficient (h_{sp})	17.2%
5	Cross section area ($A_{c/s}$)	4.4%
6	Mass flux (G)	6.3%

5.3 Result and discussion

Before starting each of these experiments, the temperature of the incoming fluid ($T_{in,elbow}$), measured at the outlet of the preheater, is maintained constant which is 30 °C throughout the experimentation. Figure 5.12 shows the variation of this temperature for complete experimentation for different flow rate. It is observed that incoming fluid temperature is varies by ±0.2 °C.

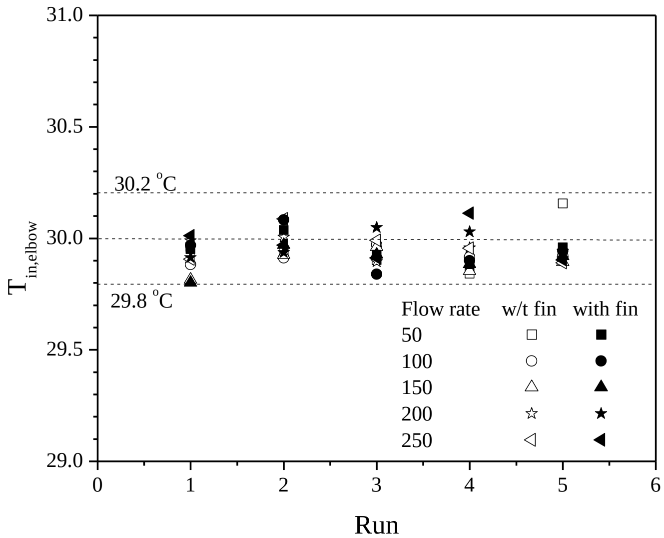

Figure 5.12 Variation of the preheater outlet temperature

5.3.1 Repeatability

Prior to starting the experiments, repeatability of the experimental setup is checked. The repeatability test has been conducted at mass flux 471 kg/m^{2}s corresponds to flow rate of 150 mlpm. Two run of the experiments have been carried out and compared to check the repeatability of the temperature and pressure readings. The temperature difference ($T_w - T_{bulk}$) and pressure drop data is shown in Fig. 5.13 and Fig. 5.14 for these two run. Temperature difference ($T_{wall} - T_{bulk}$) is found to be repeatable at deviation up to 1.1 °C for given heat flux and pressure drop is deviated between 54 to 77 Pa. The trends of temperature and pressure drop data are found repeatable.

5.3.2 Heat flux Vs temperature

Fig. 5.15 shows the variation of the effective heat flux with wall temperature for microchannels without fins. It is observed that with increase in the wall temperature, heat carried away by water increases for constant flow rate.

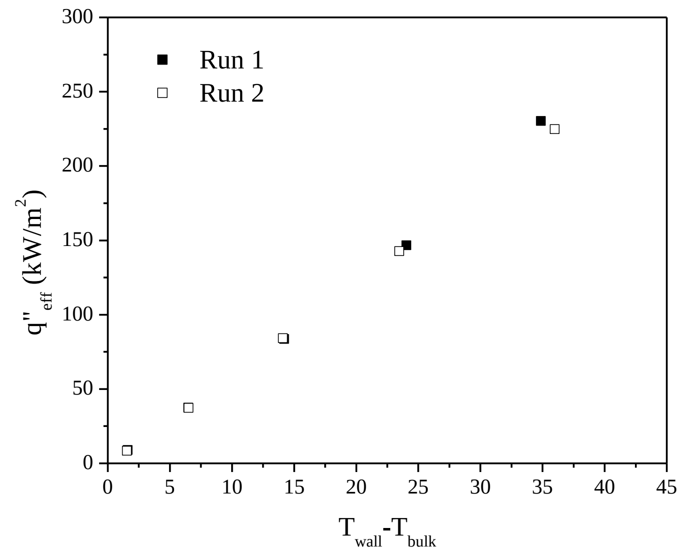

Figure 5.13 Temperature data repeatability for 471 kg/m^{2}s

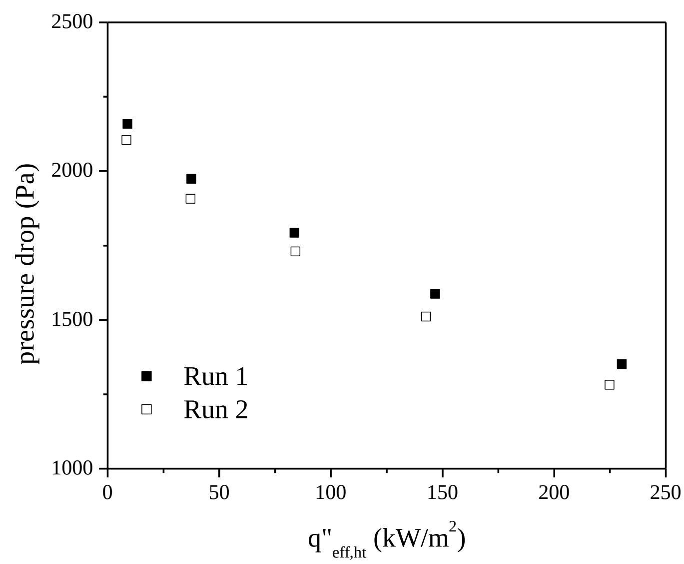

Figure 5.14 Pressure drop data repeatability for 471 kg/m^{2}s

As heat supplied at base of the microchannel heat sink increases, wall temperature increases. This results into increase in the temperature of the thermal boundary layer. Thus, thermal conductivity of the fluid present in the thermal boundary layer increases. Consequently, heat transfer rate between wetted surface and fluid increases with increase in wall temperature.

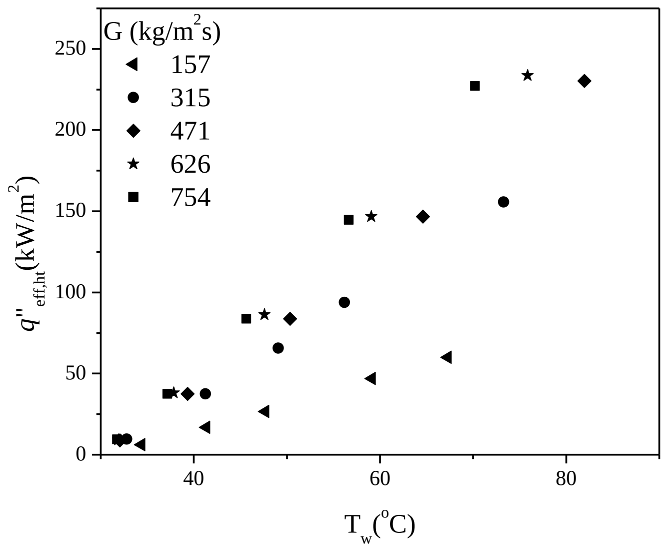

Figure 5.15 Heat flux Vs wall temperature for microchannels without fins

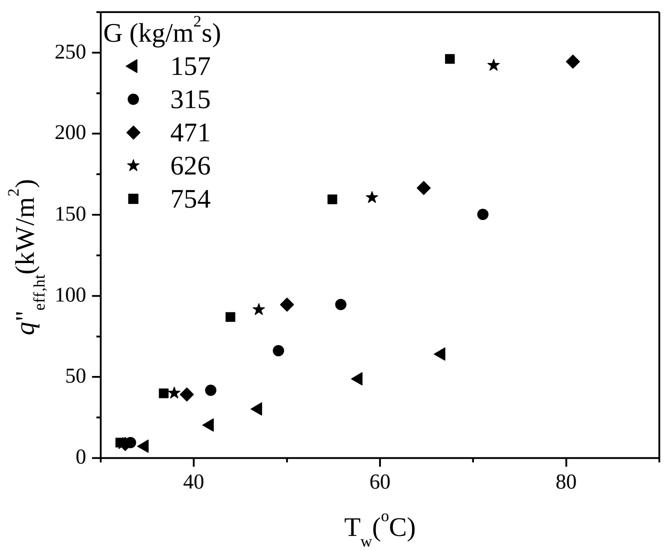

Figure 5.16 Heat flux Vs wall temperature for microchannels with fins

Further, with increase in the mass flux, heat carried by fluid increases. This is due to the fact that thermal boundary layer thickness reduces.

Similar trend is observed for the microchannel with fins as shown in the Fig. 5.16. However, there is slight increase in the effective heat flux in case of the microchannels with fins compared to microchannels without fins. By comparing both configurations, it is observed that effective heat flux in case of the microchannels with fins is around 9% higher than microchannels without fins. This is attributed to the presence of the fins (discuss in section 5.3.4).

5.3.3 Pressure drop comparison

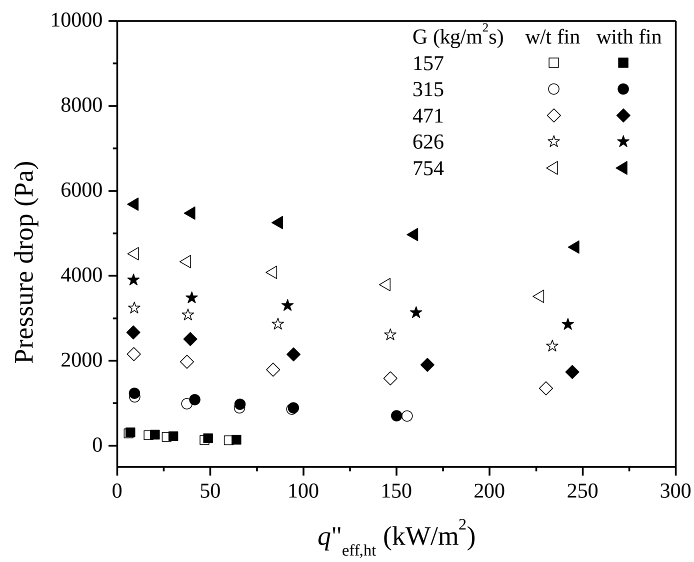

Figure 5.17 Comparison of pressure drop between without fin and with fin microchannel

Figure 5.17 shows the comparison of the pressure drop for both configurations. It is observed that pressure drop decreases as effective heat flux increases for given mass flux. Fluid temperature increases with increase in the heat flux and results into reduction in the liquid viscosity. Consequently, friction inside the fluid as well as between fluid and microchannels wall reduces. Thus, velocity of the flowing fluid increases along the channel. This increase in the velocity is presented through the increase in the Reynolds number as shown in Fig. 5.18. Thus, an overall impact of the increasing heat flux is reduction in the pressure drop for constant flow rate. For lower mass flux G = 157 kg/m^{2}s and microchannels without fins, the pressure drop reduces from 285 Pa corresponds to 6.11 kW/m^2 to 125 Pa correspond to 59.95 kW/m^2. Similarly, for microchannels with fins reduction in pressure drop is from 310 Pa for heat flux 7.18 kW/m^2 to 135 Pa for heat flux 64 kW/m^2. The trend of the pressure drop reduction is in line with previous experimental studies [85]. From Fig. 5.17, it is also concluded that, pressure drop increases with increase in the flow rate at constant heat flux. With increase in the flow rate, fluid velocity increases and contributes to the additional pressure drop. For higher mass flux G = 754 kg/m^{2}s, pressure drop decreases to 3414 Pa from 4520 Pa for without fins microchannels correspond to heat flux of 9.4 kW/m^2 and 227.1 kW/m^2 respectively. However, for microchannels with fins, pressure drop falls from 5687 Pa to 4675 Pa at heat flux of 9.4 kW/m^2 and 246.0 kW/m^2 for G = 754 kg/m^{2}s.

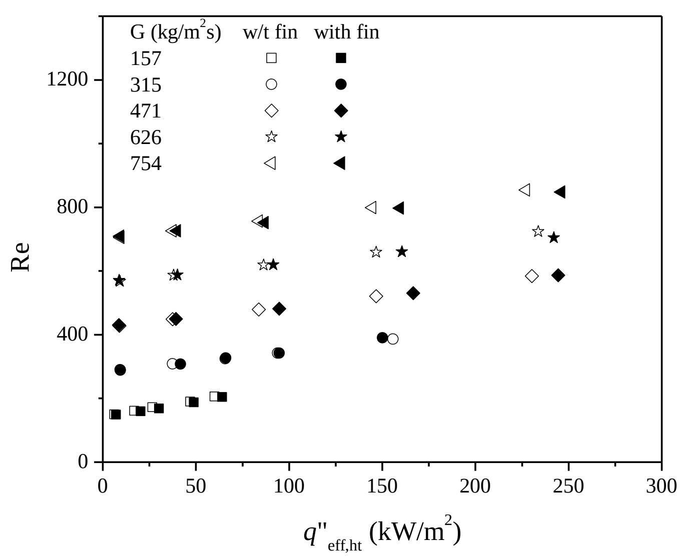

Figure 5.18 Variation of the Reynolds number with heat flux

Such lower value of the pressure drop in both configurations is attributed to the gap above the microchannel (open microchannel) which provides an easy path to flowing fluid. This is clear from the Fig. 5.17, that pressure drop for the microchannels with fins have higher than microchannels having no fins. The presence of the fins into the microchannels adds additional pressure drop because fins act as flow obstacle and retards the flow. The average percentage gain in the pressure drop penalty is 18% higher in comparison to microchannels without fins for operating conditions considered in experiments.

5.3.4 Heat transfer coefficient comparison

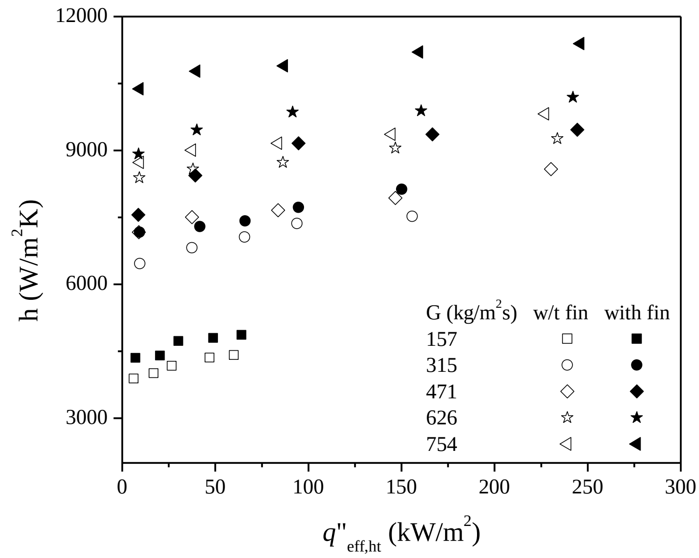

Figure 5.19 Comparison of heat transfer coefficient between without fin and with fin microchannel

Fig. 5.19 shows the comparison of the average heat transfer coefficient of microchannels with and without fins for different heat fluxes and mass fluxes conditions. In case of the microchannels without fins, it is observed that heat transfer coefficient increases almost linearly with increase in the heat flux for constant mass flux. This is attributed to the increase in the temperature of the thermal boundary layer which results into increase in exchange of the heat between liquid and surface due large temperature difference. Further, with increase in the mass flux, thermal boundary thickness reduces [217]. Heat transfer coefficient has inversely proportional relation with thickness of the thermal boundary layer. As a result heat transfer coefficient increases with increase in the mass flux.

Similar influence of heat flux and mass flux on heat transfer coefficient has been observed for microchannel with fin. However, heat transfer coefficient is higher for the microchannels with fins than that of microchannels without fins. This is attributed to the fins fabricated inside the microchannels. Fins inside the microchannels interrupt the temperature profile. As a result, thermal boundary layer breaks and is redeveloped repeatedly at leading edge of each fins. Thus flow always remains in developing stage in the region of the fins (half length of microchannel heat sink). Redevelopment of the thermal boundary layer provides better mixing of the fluid and improves heat transfer rate. Further, heat transfer rate increases due to addition of the fins surface area. The combine effect of the reestablishment of the thermal boundary layer and additional surface area makes microchannels with fins better than microchannels without fins. It is observed that for entire tests, enhancement in the heat transfer coefficient varies from minimum 7% to maximum 23% with average improvement of 15%. Thus, it is concluded that presence of the fins helps in enhancing the heat transfer performance of the microchannel heat sink.

5.3.5 Wall temperature comparison

Heat transfer performance of the microchannel heat sink is enhanced due to the presence of the fins as discussed in the above section. In addition, presence of the fins also helps in reducing the wall temperature of the microchannels. Fig. 5.20 shows the comparison of the wall temperature for microchannels with and without fins for different mass fluxes. Wall temperature increases with increase in the base heat flux almost linearly for given flow rate in both configurations. However, it is interesting to note that wall temperature is lower in case of the microchannels with fins compared to the microchannels without fins. This is attributed to enhance mixing of the fluid and additional area provided by fins. It is observed that reduction in the wall temperature is not significant at low heat flux but increases with increase in the heat flux. Similarly, increase in the mass flux results into reduction of the wall temperature. It is observed that maximum wall temperature reduction is 3.65 °C at mass flux 626 kg/m^{2}s for microchannel with fins than microchannel without fins.

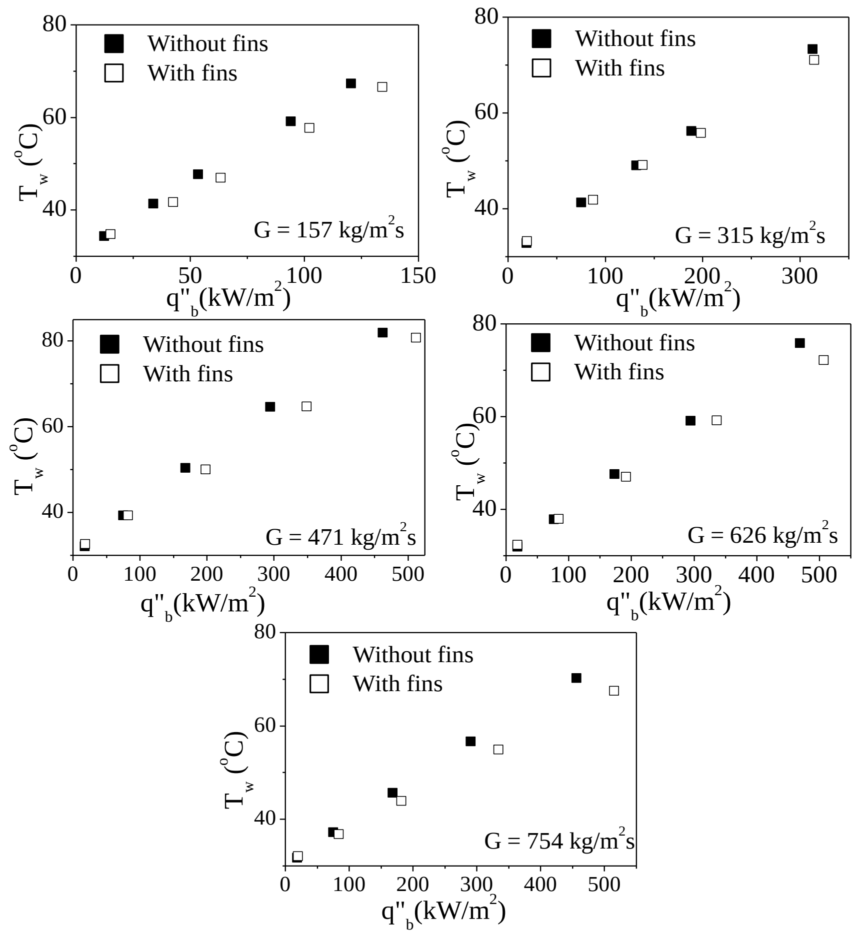

Figure 5.20 Wall temperature comparison

5.3.6 Overall thermal performance

Heat transfer enhancement and reduction in wall temperature in microchannel with fins has been observed on the expense of the pressure drop penalty. The average improvement in the heat transfer performance is 15%, on the other hand average pressure drop penalty is 18% which increases the pumping power. Hence, for the reasonable use of the microchannels with fins, it is important to consider these two parameters. These parameters are related through overall thermal performance factor (η) and given by Eq. (5.15).

$$\eta = \frac{Nu_f / Nu}{\left(\Delta P_f / \Delta P\right)^{1/3}} \tag{5.15}$$

Overall thermal performance factor helps while decision making for use of the modified microchannel from pumping power aspect. Hence, it is always desirable to have $\eta > 1$, for better deployment of the modified microchannel het sink.

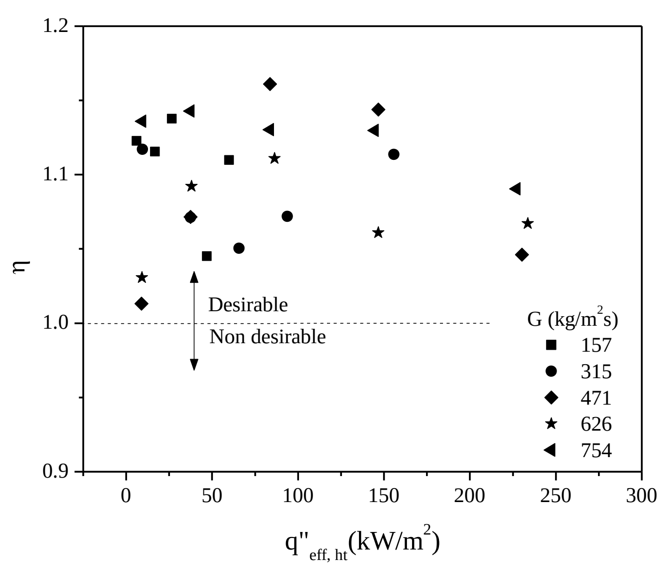

Figure 5.21 Overall thermal performance factor

Fig. 5.21 shows overall thermal performance factor for different heat fluxes and mass fluxes conditions. It is observed that thermal performance factor in all operating conditions is greater than unity. This proves that fabrications of the fins in to the microchannels are beneficial.

5.4 Comparison of open microchannel with closed microchannel

Open type of MCHSs are new addition to the area. Very limited work had been carried out yet on open type microchannels [214, 215]. Hence, it is important to compare the heat transfer and Pressure drop characteristics of closed and open type microchannels. Experimental pressure drop of open type MCHS has been compared with corresponding closed type MCHS with same dimensions. Pressure drop in closed microchannel heat sink is calculated using Eq. (5.16) [197].

$$\Delta P = \frac{\rho u_m^2}{2}\left[\left(\frac{A_c}{A_p}\right)^2 (2K_{90}) + K_c + K_e + \frac{4 f_{app} L}{D_h}\right] \tag{5.16}$$

Where, u_m is mean velocity, K_{90} is bend loss coefficient, K_c and K_e represents the contraction and expansion loss coefficient due to area change. Value of the K_{90}, K_c and K_e are considered as 1.2, 1 and 1 respectively. The value of the f_{app} (= 14.23/Re) is calculated considering fully developed flow inside the microchannel.

Figure 5.22 shows the pressure drop comparison of open type MCHS and closed type MCHS. It is clear that the open type microchannel heat sink suffers very less pressure drop penalty as compared to closed type MCHS and pressure drop penalty increases with increase in Reynolds Number. The gap above the microchannels provide the easy passage for the flowing fluid across microchannels thus they can operate at expanse of less pressure drop. It is observed that average pressure drop inside closed type MCHS heat sink is around 14 times higher compared to the open type MCHS.

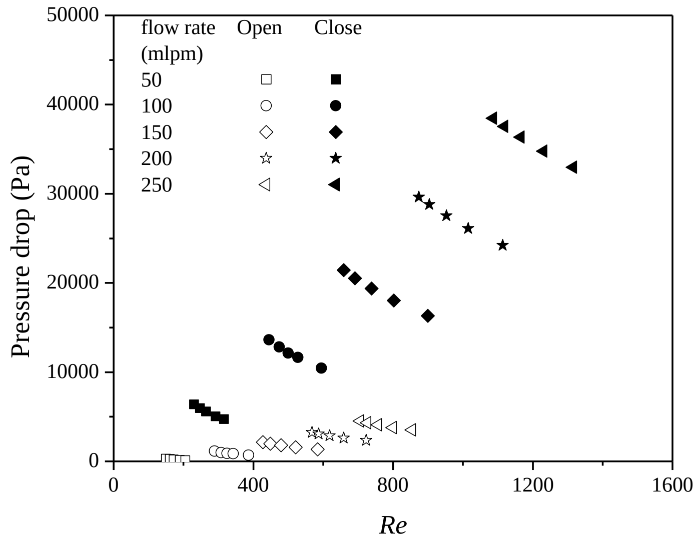

Figure 5.22 Comparison of pressure drop for open type and closed type MCHS

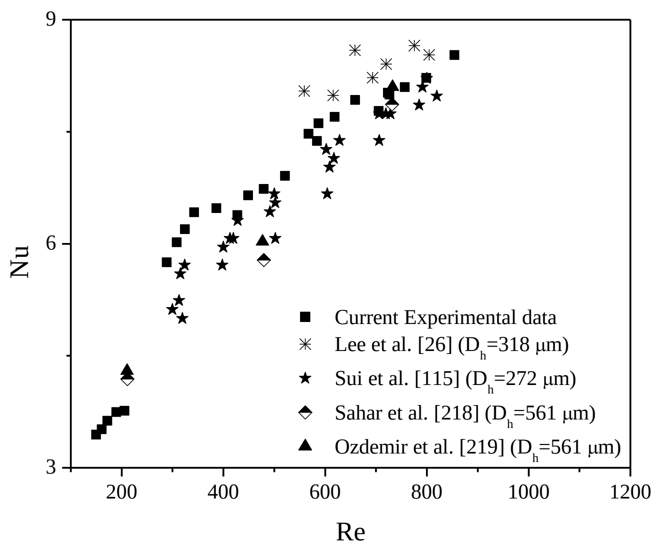

Figure 5.23 Comparison of Nusselt number for open type and closed type MCHS

Heat transfer performance of the open and closed type MCHS could not be compared as average thermophysical properties of fluid for the corresponding close MCHS are not known.

Figure 5.23 shows the experimental observation of heat transfer performance of open type MCHS and heat transfer performance of close type MCHS available from the past literature [26, 115, 218, 219], which are found close to size and operating conditions of the current study. It can be observed that heat transfer performance of open type MCHS is comparable with close type MCHS. However, more number of experimental studies are required to draw realistic comparison of pressure drop characteristics and heat transfer performance between open type MCHS and closed type MCHS.

5.5 Conclusion

Experiments of single phase liquid flowing through open type microchannel heat sink has been carried out. Two configurations of the microchannels have been tested; (1) microchannel without fins, (2) microchannels with fins. Following observations are made based on current experimentation:

1. Microchannel with fins has higher value effective heat flux and it is around 9% higher than microchannels without fins. It is attributed to the presence of the fins which helps in providing the proper mixing of liquid and additional heat transfer area.
2. It is observed that microchannels with fins has higher average pressure drop penalty of 18% compared to the microchannels without fins.
3. An average heat transfer coefficient improvement is 15% in microchannels with fins compared to microchannel without fins.

4. It is observed that maximum wall temperature reduction is 3.65 °C at mass flux 626 kg/m^2s for microchannel with fins than microchannels without fins.
5. From the current experimentation, it is recommended to use fins in the microchannels based on the overall thermal performance factor as its value is above the unity in all operating conditions tested in current study.

CHAPTER 6

OVERALL CONCLUSION AND FUTURE SCOPE

6.1 Conclusion

The main objective of the present study is to develop energy based bubble growth model for prediction of the bubble growth at nucleation site in microchannel. Further, effort has been made to extend this bubble growth model to analyze different phenomena associated with flow boiling in microchannel such waiting time, proposed non dimensional energy ratio to differentiate inertia controlled and thermal diffusion controlled region and critical heat flux (CHF). Eventually, experimentation has been carried out with single phase liquid phase flow through open microchannel heat sink. Two configuration of microchannel heat sinks are fabricated; (1) microchannels without fins, (2) microchannels with fins. The thermal performance of these two configurations has been studied.

Following are the main conclusions/outcomes of the current research work.

1. It is evident that bubble dynamics plays an important role heat transfer and pressure drop characteristics of flow boiling in microchannel. A new energy balance bubble growth model has been proposed to predict the bubble growth behavior at nucleation site in microchannel. Developed model shows good agreement with available experimental results mean percentage error of 14.4%. Proposed model is also extended for prediction of waiting time and it is found that model predicts waiting time also with good accuracy.

2. Bubble inception and growth in microchannel is very conspicuous phase in microchannels. New non-dimensional energy ratio terms based on bubble growth model at nucleation site are introduced. It

is found that E_1 (energy used in bubble growth/energy required to overcome surface tension) can be used to distinguish inertia and thermal diffusion controlled region during initial phase of bubble growth at nucleation site. The effect of these non-dimensional numbers on bubble confinement and CHF conditions are discussed.

3. Condition of CHF is the key design consideration for the systems involving heat dissipation through boiling application. Unlike the conventional channels, the CHF correlation for microchannels are limited and associated with significant errors. Combining semi-empirical approaches (combining energy balance based bubble growth model and non-dimensional analysis); New CHF correlations for refrigerants and water have been proposed. The mean errors for the refrigerant and water cases are, respectively, found to be 21% and 27% for seven and six relevant datasets. Around 77% data of the refrigerant and 60% data of water are predicted within error band of ± 30%.

4. Heat transfer and pressure drop behavior of single phase flow in open type microchannel are measured experimentally. It is found that open type microchannel provided comparable heat transfer performance but pressure drop penalty was increased by around 18%. Heat transfer performance augmentation of open type microchannel using extended surface is also carried out. Extended surface intensified heat transfer performance of open type microchannel by 15% and reduction in the wall temperature is 3.65 °C. Overall thermal performance of the extended open type microchannel is found to be above unity for all operating condition.

6.2 Future scope

Following are the suggestions for future work:

1. Bubble departure from the nucleation site plays vital role in microchannel. Current energy based bubble growth model involves various resistive effects such as surface tension, inertia, drag, gravity (buoyancy) and force due to evaporation momentum. Among these effects, some try to hold the bubble at nucleation site and some try to detach the bubble. There can be some additional effects, which are not considered in current model, can influence the bubble departure. It can be possible to obtained bubble departure diameter by carefully balancing (holding and detaching) the resistive effects and possible additional effects.

2. More rigorous experimentation needs to be carried out on open type microchannel including single phase flow and two phase boiling flow both in order to ascertain the benefits offered by them in comparison to the conventional channel. Bubble flow dynamic studies on open type microchannel can be another interesting area, which can be carried out. It would also be interesting to explore, how these type of microchannel facilitates in improving CHF condition associated with conventional channels.

APPENDIX

Appendix A

A.1 Various effects

Energy required in overcoming inertia effect:

Mass flow rate is, $\dot{m} = \rho_l A_{i,c/s} v$ (A.1)

Where, *v* is liquid mean velocity (m/s).

$$F_i = \dot{m} v = \rho_l A_{i,c/s} v^2 \qquad \text{(A.2)}$$

Energy required to overcoming inertia:

$$Er_i = F_i \times \text{growth rate} = \dot{m} v \times \text{growth rate} = \rho_l A_{i,c/s} v^2 \frac{dr}{dt} \qquad \text{(A.3)}$$

$$Er_i = \frac{G^2}{\rho_l} \frac{\gamma}{2} r^2 \frac{dr}{dt} \qquad \text{(A.4)}$$

Energy required in overcoming drag effect:

Drag force is defined in term of shear stress. Shear stress is given by (from Newton low of viscosity)

$$\tau = \mu \frac{dv}{dy} = \mu \frac{v}{2r} \qquad \text{(A.5)}$$

Drag Force $F_{sh} = \tau \times \frac{A_{i,s}}{2}$ (A.6)

Energy required to overcoming drag effect:

$$Er_{sh} = F_{sh} \times \text{growth rate} = \tau \times \frac{A_{i,s}}{2} \times \frac{dr}{dt} \qquad \text{(A.7)}$$

$$Er_{sh} = \mu \frac{G}{4 \cdot \rho_l} \times \pi \cdot \beta \times r \frac{dr}{dt} \qquad \text{(A.8)}$$

Energy required in overcoming the surface tension effect at interface:

Gibbs free surface energy $dG = \sigma \cdot dA_{i,s}$ (A.9)

Energy required to overcoming surface tension: $Er_{sf} = \sigma \cdot \frac{dA_{i,s}}{dt}$ (A.10)

$$Er_{sf} = \sigma \cdot (2 \cdot \pi \cdot \beta) \cdot r \frac{dr}{dt} \quad (A.11)$$

Energy required in overcoming gravitational effect:

Gravitational energy $Er_g = (\rho_l - \rho_v) \cdot g \cdot a \frac{dV_i}{dt}$ (A.12)

$$Er_g = \pi (\rho_l - \rho_v) \cdot g \cdot \alpha \cdot \phi \, r^3 \frac{dr}{dt} \quad (A.13)$$

Energy required in overcoming the force due change in evaporation momentum:

Force due change in momentum due to evaporation is given as

$Fem = evaporation$ mass flow rate $\times$ vapor velocity relative to vapor interface

$$Fem = \frac{q''}{h_{fg}} \times A_{i,s} \times \frac{q''}{h_{fg} \rho_v} \quad (A.14)$$

Energy required in overcoming this effect $Er_m = Fem \times \frac{dr}{dt}$ (A.15)

$$Er_m = \left(\frac{q''}{h_{fg}} \right)^2 \frac{\pi \cdot r^2 \cdot \beta}{\rho_v} \frac{dr}{dt} \quad (A.16)$$

A.2 Bubble geometry

Bubble volume:

Geometry of the truncated bubble is shown in Fig. A.1 and Fig. A.2.

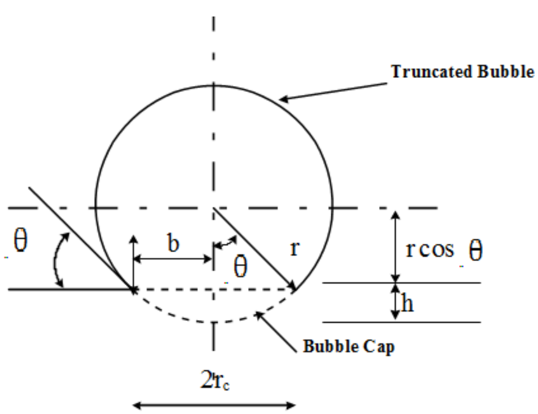

Figure A.1 Truncated bubble

Volume of spherical bubble $= \frac{4}{3}\pi \cdot r^3$ (A.17)

Volume of spherical cap $= \frac{3h}{6}\left(3b^2 + h^2\right)$ (A.18)

Where, $b = r\sin\theta$ and $h = r(1-\cos\theta)$.

Volume of the truncated bubble = Volume of spherical bubble - Volume of spherical cap

Therefore, Volume of the truncated bubble $= \frac{4}{3}\pi \cdot r^3 - \frac{3h}{6}\left(3b^2 + h^2\right)$ (A.19)

Volume of the truncated bubble

$$= \pi \cdot r^3\left[4 - 0.5\left\{3(1-\cos\theta)\sin^2\theta + (1-\cos\theta)^3\right\}\right] \quad \text{(A.19)}$$

Where, $\alpha = \left[4 - 0.5\left\{3(1-\cos\theta)\sin^2\theta + (1-\cos\theta)^3\right\}\right]$ (A.20)

Bubble surface area:

Surface area of spherical bubble $= 4\pi \cdot r^2$ (A.21)

Surface area of the spherical cap $= \pi\left(b^2 + h^2\right)$ (A.22)

Surface area of the truncated bubble = Surface area of spherical bubble- Surface area of the spherical cap

Surface area of truncated bubble $= 4\pi \cdot r^2 - \pi\left(a^2 + h^2\right)$ (A.23)

Surface area of truncated bubble $= \pi \cdot r^2\left[4 - \left\{\sin^2\theta + (1-\cos\theta)^2\right\}\right]$ (A.24)

Surface area of truncated bubble, $A_{i,s} = \pi \cdot r^2 \cdot \beta$ (A.25)

Where, $\beta = \left[4 - \left\{\sin^2\theta + (1-\cos\theta)^2\right\}\right]$ (A.26)

Bubble cross sectional area:

C/s area of spherical bubble $= \pi \cdot r^2$ (A.27)

C/s area of spherical cap $= \frac{1}{2} \cdot r^2\left[\frac{2\pi\theta}{180} - \sin 2\theta\right]$ (A.28)

C/s area of truncated bubble = C/s area of spherical bubble- C/s area of spherical cap

Therefore, C/s area of truncated bubble $= \pi \cdot r^2 - \frac{1}{2} \cdot r^2\left[\frac{2\pi\theta}{180} - \sin 2\theta\right]$ (A.29)

Therefore, C/s of truncated bubble $=\frac{1}{2}r^2\left[2\pi-\frac{2\pi\theta}{180}+\sin 2\theta\right]$ (A.30)

C/s area of truncated bubble, $A_{i,c/s}=\frac{1}{2}\cdot r^2\gamma$ (A.31)

where, $\gamma=\left[2\pi-\frac{2\pi\theta}{180}+\sin 2\theta\right]$ (A.32)

Bubble centroid:

Form Triangle ABC, summation of angle is, $180=90+\frac{\psi}{2}+\lambda$ (A.33)

From triangle ACD, summation of angle is,

$180=(180-\theta)+90+\lambda$ (A.34)

Form Eq. (A.33) and Eq. (A.34), $\psi=2(180-\theta)$

Similarly, form triangle ABD, summation of angle is,

$180=\frac{\psi}{2}+90+\eta$ (A.35)

Therefore, $\eta=90-\frac{\psi}{2}$ (A.36)

From triangle ABD, BD = $x=r\sin\eta$ (A.37)

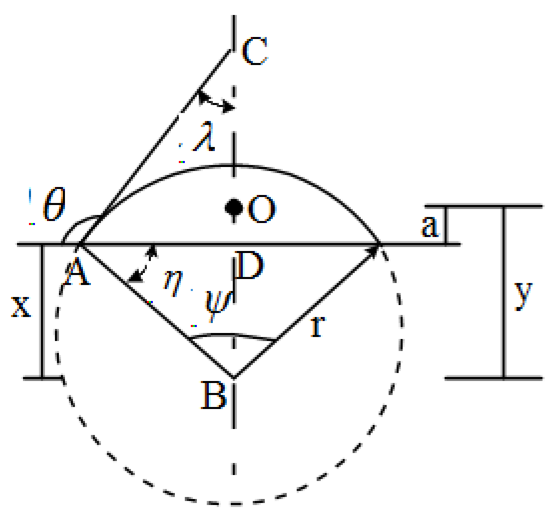

Figure A.2 Centroid of bubble

Centroid of the spherical bubble is $y=\frac{4r\sin^3\left(\frac{\psi}{2}\right)}{3\left(\beta-\sin\psi\right)}$ (A.38)

Centroid of the truncated bubble is DO, $a=y-x$ (A.39)

$$a = y - x = r\left[\frac{4\sin^3\left(\frac{\psi}{2}\right)}{3(\psi - \sin\psi)} - \sin\left(90 - \frac{\psi}{2}\right)\right] = r\varphi \tag{A.40}$$

Where, $$\varphi = \left[\frac{4\sin^3\left(\frac{\psi}{2}\right)}{3(\psi - \sin\psi)} - \sin\left(90 - \frac{\psi}{2}\right)\right] \tag{A.41}$$

A.3 Derivation of the bubble growth model

$$q''\varepsilon \cdot A_c = E_{bubble} + Er_{sf} + Er_i + Er_{sh} + Er_g + Er_m \tag{A.42}$$

Substituting, E_{bubble}, Er_{sf}, Er_i, Er_{sh}, Er_g and Er_m in Eq. (A.42), we get;

$$\begin{aligned} q''\varepsilon \cdot A_c &= \rho_v h_{fg}\frac{dV_i}{dt} + \sigma\cdot(2\cdot\pi\cdot\beta)\cdot r\frac{dr}{dt} \\ &+ \frac{G^2}{2\rho_l}\gamma\cdot r^2\frac{dr}{dt} + \mu\frac{G}{4\cdot\rho_l}\pi\cdot r\cdot\beta\cdot\frac{dr}{dt} \\ &+ g(\rho_l - \rho_v)\cdot a\frac{dV}{dt} + \left(\frac{q''}{h_{fg}}\right)^2\frac{\pi\cdot r^2\cdot\beta}{\rho_v}\frac{dr}{dt} \end{aligned} \tag{A.43}$$

Upon simplification we get;

$$\begin{aligned} q''\frac{A_c}{A_{ch}}\frac{\gamma}{2}dt &= \pi\cdot\alpha\cdot\rho_v h_{fg}dr + \sigma\cdot(2\cdot\pi\cdot\beta)\cdot\frac{1}{r}dr \\ &+ \frac{G^2}{2\rho_l}\gamma\cdot dr + \mu\frac{G}{4\cdot\rho_l}\pi\cdot\beta\frac{1}{r}\cdot dr \\ &+ g(\rho_l - \rho_v)\cdot\pi\cdot\alpha\cdot\varphi\cdot r dr + \left(\frac{q''}{h_{fg}}\right)^2\frac{\pi\cdot\beta}{\rho_v}dr \end{aligned} \tag{A.44}$$

On integrating above equation we get;

$$\begin{aligned} q''\frac{A_c}{A_{ch}}\frac{\gamma}{2}t &= \left[g(\rho_l - \rho_v)\frac{\pi\cdot\alpha\cdot\varphi}{2}\right]\cdot r^2 \\ &+ \left[\sigma\cdot(2\cdot\pi\cdot\beta) + \frac{\mu\cdot G}{4\cdot\rho_l}\pi\cdot\beta\right]\ln(r) \\ &+ \left[\pi\cdot\alpha\cdot\rho_v h_{fg} + \frac{G^2}{\rho_l}\frac{\gamma}{2} + \left(\frac{q''}{h_{fg}}\right)^2\frac{\pi\cdot\beta}{\rho_v}\right]\cdot r + C \end{aligned} \tag{A.45}$$

The bubble becomes visible at nucleation site, when it reaches up to cavity mouth. Therefore, it is assumed that minimum visible bubble radius is equal to nucleation cavity radius.

Boundary condition; $t=t_{FV}=0; r=r_c=r_{min}$

$$
\begin{aligned}
C = &-\left[g(\rho_l-\rho_v)\frac{\pi\cdot\alpha\cdot\varphi}{2}\right]\cdot r_{\min}^2 \\
&-\left[\sigma\cdot(2\cdot\pi\cdot\beta)+\frac{\mu\cdot G}{4\cdot\rho_l}\pi\cdot\beta\right]\ln\left(r_{\min}\right) \\
&-\left[\pi\cdot\alpha\cdot\rho_v h_{fg}+\frac{G^2}{\rho_l}\frac{\gamma}{2}+\left(\frac{q''}{h_{fg}}\right)^2\frac{\pi\cdot\beta}{\rho_v}\right]\cdot r_{\min}
\end{aligned}
\tag{A.46}
$$

Substituting value of the constant, which in terms of the r_{min}, we get final form of the bubble growth model;

$$
\begin{aligned}
&\left[g(\rho_l-\rho_v)\frac{\pi\cdot\alpha\cdot\varphi}{2}\right]\cdot r^2 +\left[\sigma\cdot(2\cdot\pi\cdot\beta)+\frac{\mu\cdot G}{4\cdot\rho_l}\pi\cdot\beta\right]\ln(r) \\
&+\left[\pi\cdot\alpha\cdot\rho_v h_{fg}+\frac{G^2}{\rho_l}\frac{\gamma}{2}+\left(\frac{q''}{h_{fg}}\right)^2\frac{\pi\cdot\beta}{\rho_v}\right]\cdot r - q''\,\frac{A_c}{A_{ch}}\,\frac{\gamma}{2}t \\
&-\left[g(\rho_l-\rho_v)\frac{\pi\cdot\alpha}{2}\right]\cdot r_{\min}^2 -\left[\sigma\cdot(2\cdot\pi\cdot\beta)+\frac{\mu\cdot G}{4\cdot\rho_l}\pi\cdot\beta\right]\ln\left(r_{\min}\right) \\
&-\left[\pi\cdot\alpha\cdot\rho_v h_{fg}+\frac{G^2}{\rho_l}\frac{\gamma}{2}+\left(\frac{q''}{h_{fg}}\right)^2\frac{\pi\cdot\beta}{\rho_v}\right]\cdot r_{\min} = 0
\end{aligned}
\tag{A.47}
$$

Appendix B

CHF can be given by Eq. (D2).

$$q_{CHF} = f\left(\rho_l, \rho_v, \sigma, \mu_l, \mathrm{g}, h_{fg}, G, r_h, \alpha, \beta, \gamma, \phi\right) \tag{B.1}$$

Total number of variable = n = 13

Repeating variables = k = 4 (i.e. r_h, σ, G, α)

This variable are r_h, σ, G, α. Thus, Number of π terms are = $n - k$ = 13 – 4 = 9

Table B.1 represent the dimensions of the each variable considered into the analysis

Table B.1

Variables and their dimensions

Sr. No.	**variable**	**unit**	**Dimension**
1	Critical heat flux	*W/m²*	$M^1L^0T^{-3}\theta^0$
2	Liquid density	*Kg/m³*	$M^1L^{-3}T^0\theta^0$
3	Vapor density	*Kg/m³*	$M^1L^{-3}T^0\theta^0$
4	Surface tension	*N/m*	$M^1L^0T^{-2}\theta^0$
5	Liquid viscosity	*Pa-s*	$M^1L^{-1}T^{-1}\theta^0$
6	Gravity	*m/s²*	$M^0L^1T^{-2}\theta^0$
7	Latent heat of vaporization	*J/kg*	$M^0L^2T^{-2}\theta^0$
8	Mass flux	*Kg/m²s*	$M^1L^{-2}T^{-1}\theta^0$
9	Bubble radius	*m*	$M^0L^1T^0\theta^0$
10	Parameter due to bubble volume	*radian*	$M^0L^0T^0\theta^1$
11	Parameter due to bubble surface area	*radian*	$M^0L^0T^0\theta^1$
12	Parameter due to bubble cross sectional area	*radian*	
13	Parameter due to bubble centroid	*radian*	$M^0L^0T^0\theta^1$

First Π is given as:

$$\Pi_1 = q_{CHF} r_h^{a_1} \sigma^{b_1} G^{c_1} \alpha^{d_1} \tag{B.2}$$

Since this combination is to be dimensionless, it follows that

$$\begin{aligned}\left[M^0 L^0 T^0 \theta^0\right] = \left[M^1 L^0 T^{-3} \theta^0\right]\left[M^0 L^1 T^0 \theta^0\right]^{a_1}\left[M^1 L^0 T^{-2} \theta^0\right]^{b_1} \\ \left[M^1 L^{-2} T^{-1} \theta^0\right]^{c_1}\left[M^0 L^0 T^0 \theta^1\right]^{d_1}\end{aligned} \tag{B.3}$$

The exponents a_1, b_1, $c_1$and d_1 must be determined such that the resulting exponent for each of the basic dimensions–M, L, T and θ –must be zero (so that the resulting combination is dimensionless).

Thus, we can write

For M: $0=1+0+b_1+c_1+0$

For L: $0=1+a_1+0-2c_1+0$

For T: $0= -3+0-2b_1- c_1+0$

For θ: $0=0+0+0+0+d_1$

The solution of this system of algebraic equations gives the desired values for coefficients a_1, b_1, c_1 and d_1. It follows that a_1=2, b_1= –2, c_1=1 and d_1=0, therefore,

$$\Pi_1 = \frac{q_{CHF} r_h^2 G}{\sigma^2} \tag{B.4}$$

The process is now repeated for the remaining non repeating variables. All these Π terms are presented in Table B.2.

Table B.2

Final forms of Π terms

Expression for π term	Value of coefficients	Final form of π term
$\Pi_2 = \rho_v r_h^{a_2} \sigma^{b_2} G^{c_2} \alpha^{d_2}$	a_2= –1, b_2= 1, c_2= –2, d_2=0	$\Pi_2 = \frac{\rho_v \sigma}{r_h G^2}$
$\Pi_3 = \rho_l r_h^{a_3} \sigma^{b_3} G^{c_3} \alpha^{d_3}$	a_3= –1, b_2= 1, c_1= –2, d_1=0	$\Pi_3 = \frac{\rho_l \sigma}{r_h G^2}$
$\Pi_4 = \mu_l r_h^{a_4} \sigma^{b_4} G^{c_4} \alpha^{d_4}$	a_4= –1, b_4= 0, c_4= –1, d_4=0	$\Pi_4 = \frac{\mu_l}{r_h G}$
$\Pi_5 = g r_h^{a_5} \sigma^{b_5} G^{c_5} \alpha^{d_5}$	a_5= 3, b_5= –2, c_5= 2, d_5=0	$\Pi_5 = \frac{g r_h^3 G^2}{\sigma^2}$
$\Pi_6 = h_{fg} r_h^{a_6} \sigma^{b_6} G^{c_6} \alpha^{d_6}$	a_6= 2, b_6= –2, c_6= 2, d_6=0	$\Pi_6 = \frac{h_{fg} r_h^2 G^2}{\sigma^2}$
$\Pi_7 = \beta r_h^{a_7} \sigma^{b_7} G^{c_7} \alpha^{d_7}$	a_7= 0, b_7= 0, c_7= 0, d_7=0	$\Pi_7 = \frac{\beta}{\alpha}$
$\Pi_8 = \gamma r_h^{a_8} \sigma^{b_8} G^{c_8} \alpha^{d_8}$	a_8= 0, b_8= 0, c_8= 0, d_8=0	$\Pi_8 = \frac{\gamma}{\alpha}$
$\Pi_9 = \phi r_h^{a_9} \sigma^{b_9} G^{c_9} \alpha^{d_9}$	a_9= 0, b_9= 0, c_9= 0, d_9=0	$\Pi_9 = \frac{\phi}{\alpha}$

Appendix C

C.1 Thermocouple calibration

Pt 100 probe of the Test-480 instrument and thermostatic bath are used for calibrating the thermocouples. Pt 100 probe has an accuracy of the ±0.15°C having measuring range of -100 °C to 400°C. All thermocouples and pt 100 probe are immersed into a thermostatic bath at same level as shown in Fig. C.1.

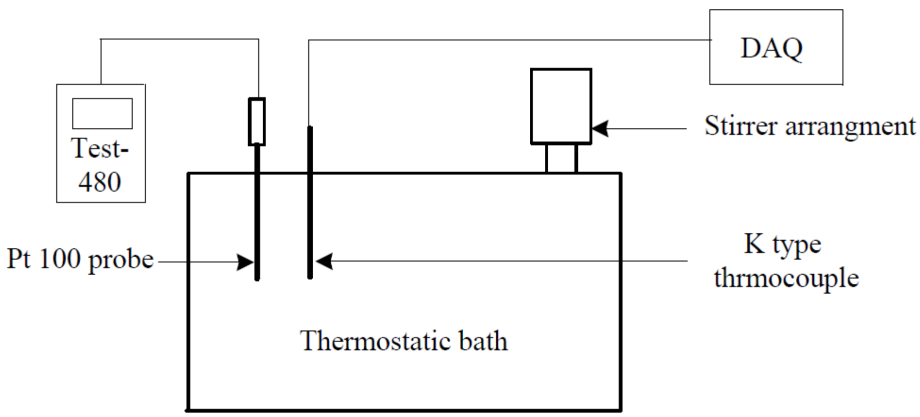

Figure C.1Schematic of thermocouple calibration

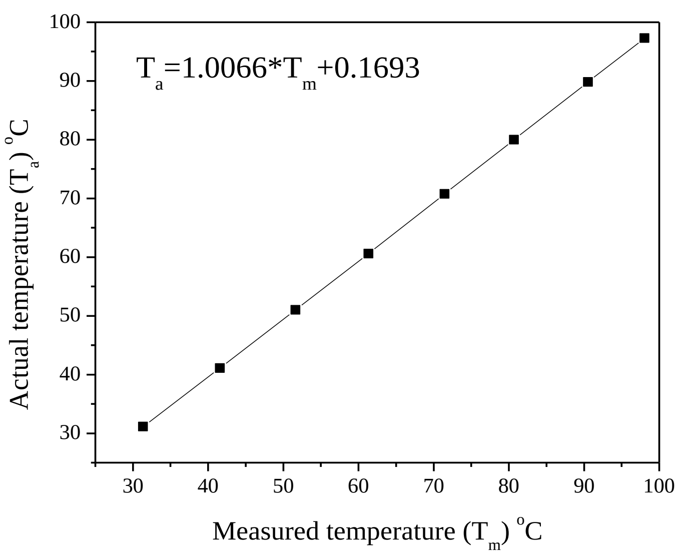

Figure C.2 Thermocouple calibration

Pt 100 probe is connected to the Test-480 instrument and all thermocouples are connected to the data acquisition system. The temperature of the thermostatic bath was increased in step of 10°C. The values of the probe and thermocouples were recorded for different temperatures setting after reaching steady state. The actual temperature as indicated by the Pt 100 (T_a) and the measured temperature (T_m) were plotted as shown in Fig. C.2. Thermocouples are found accurate to ±0.59 °C with accuracy of ±0.9%.

C.2 Mass flow meter calibration

Mass flow meter is calibrated by liquid collection method. This method includes measuring flask having known volume and stop watch which is used for measuring the time for prescribe time. Initial pump is set to the defined flow rate (50, 100, 150,200, 250 mlpm) through the control drive. The fluid is collected for interval of 10 min for every flow rate.

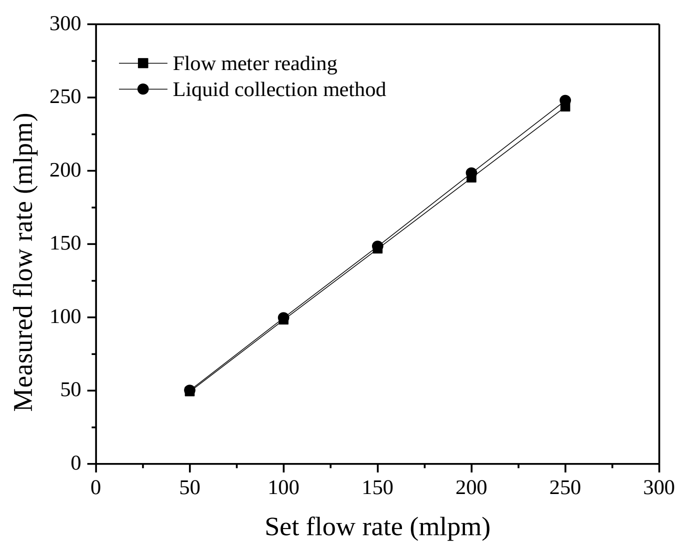

Figure C.3 Mass flow meter calibration

This collected volume of the fluid is measure through the measuring flask. At same time, signal from the mass flow meter is recorded with help of data acquisition system. Finally, flow rate obtained from the liquid collection method and signal received from the mass flow meter are compared. This comparison is presented in Fig. C.3. It is observed that mass flow meter has accuracy less than 2%.

C.3 Error analysis

The uncertainty in the estimated or calculated quantity was estimated based on the uncertainties in the primary measured quantities. Method of the uncertainties has been explained below [220]. If the estimated quantity R is a function of independent primary measurements x_1, x_2, x_3, …… x_n, which can be represented as

$$E = f(x_1, x_2, ...x_n) \tag{C.1}$$

If δR is the uncertainty in the estimated quantity R and δx_1, δx_2, δx_3, …….. δx_n are the uncertainties in the independent measured variables, then δ_E can be calculated as

$$\delta R = \sqrt{\left[\left(\frac{\partial R}{\partial x_1}\delta x_1\right)^2 + \left(\frac{\partial R}{\partial x_2}\delta x_2\right)^2 + ... + \left(\frac{\partial R}{\partial x_n}\delta x_n\right)^2\right]} \tag{C.2}$$

Temperature, pressure, mass of hydrogen absorbed/desorbed, hydrogen storage capacity and reacted fraction were measured/estimated during the PCI and kinetics measurements.

Measured Quantities

The accuracy of the various measured quantities such as microchannel dimensions, temperature measurement and mass flow rate are presented in Table C.1.

Table C.1

Uncertainty in measured quantity

S No.	Measurement	Device	Accuracy
1	Microchannel width (W_c)	Micrometer	±5%
2	Microchannel height (H_c)	Micrometer	±11.5%
3	Wall width (W_w)	Micrometer	±2%
4	Length (L)	Vernier caliper	±0.04%
5	Gap Height (H_g)	Micro screw gauge	±2.5%
6	Temperatures (T)	Thermocouple	±0.09%
7	Mass flow rate ($\dot{m}$)	Coriolis mass flow meter	±2%

Estimated Quantities

In this section, sample calculation of the effective heat carried away by the water is presented.

Heat carried away by the water $q_{eff} = \dot{m}C_p\left(T_{out} - T_{in}\right)$ (C.3)

Heat carried away by the water is function of the mass flow rate, specific heat, inlet temperature and outlet temperature. Thus, as per Eq. (C.2), q_{eff} has to differentiate partially with mass flow rate, inlet temperature and outlet temperature as shown by Eq. (C.4). For calculation purpose: $\dot{m}$ = 0.0008240 Kg/sec, T_{in} = 31.48 °C, T_{out} = 33.15 °C, C_p = 4179.7 J/kg°C.

Thus, with mass flow rate;

$$\delta q_{eff} = \sqrt{\left[\left(\frac{\partial q_{eff}}{\partial \dot{m}}\delta \dot{m}\right)^2 + \left(\frac{\partial q_{eff}}{\partial T_{out}}\delta T_{out}\right)^2 + \left(\frac{\partial q_{eff}}{\partial T_{in}}\delta T_{in}\right)^2\right]} \qquad \text{(C.4)}$$

Where, $\frac{\partial q_{eff}}{\partial \dot{m}} = C_p\left(T_{out} - T_{in}\right)$ = 4179.7 X (33.15-31.48) = 6980.1 (C.5)

$$\frac{\partial q_{eff}}{\partial T_{out}} = \dot{m}C_p = 0.000824 \text{ X } 4179.7 = 3.44 \qquad \text{(C.6)}$$

$$\frac{\partial q_{eff}}{\partial T_{in}} = -\dot{m}C_p = 0.000824 \text{ X } 4179.7 = -3.44 \qquad \text{(C.7)}$$

$$\delta\dot{m} = Error\ (\dot{m}) \text{ X } measured\ value\ (\dot{m}) = 0.02 \text{ X } 0.000824 = 1.65\text{e-}5 \text{ kg/sec} \qquad \text{(C.8)}$$

$$\delta T_{out} = Error\ \left(T_{out}\right) \text{ X } measured\ value\ \left(T_{out}\right) = 0.009 \text{ X } 33.16 = 0.298\ °\text{C} \qquad \text{(C.9)}$$

$$\delta T_{in} = Error\ \left(T_{in}\right) \text{ X } measured\ value\ \left(T_{in}\right) = 0.009 \text{ X } 31.48 = 0.283\ °\text{C} \qquad \text{(C.10)}$$

Thus,

δq_{eff} = ((6980.1 X 1.65e-5)^2 + (3.44 X 0.298)^2 + (-3.44 X 0.283)^2)$^{0.5}$

δq_{eff} = 1.41 W or 0.024%.

Similarly, uncertainty for other estimated parameter is calculated and presented into Table C.2.

Table C.2

Uncertainty in estimated quantity

S No.	Measurement	Equation	Uncertainty
1	Gap width (W_g)	$W_g = N\,W_C + (N-1)\,W_w$	2.8%
2	Heat transfer area (A_{ht})	$A_{ht} = N(W_C + 2H_C)L + (N-1)W_w L$	5.7%
3	Effective heat flux (q''_{ht})	$q''_{eff,ht} = \dfrac{q_{eff}}{A_{ht}}$	17.2%
4	Heat transfer coefficient (h_{sp})	$h_{sp} = \dfrac{q''_{eff,ht}}{\left(T_w - T_{bulk}\right)}$	17.2%
5	Cross section area ($A_{c/s}$)	$A_{c/s} = NW_c H_c + H_g W_g$	4.4%
6	Mass flux (G)	$G = \dfrac{\dot{m}}{NA_{ch}}$	6.3%

C.4 Readings

Table C.3

Microchannels without fins

G	q"$_b$	q"$_{ht}$	T_{in}	T_{out}	T_w	ΔP
kg/m^2 S	W/m^2	W/m^2	°C	°C	°C	Pa
160.0	12.3	6.1	31.5	33.2	34.4	285.7
159.6	33.8	16.8	33.6	38.2	41.3	245.6
159.6	53.5	26.7	35.7	43.0	47.7	201.3
158.5	94.2	46.9	38.7	51.6	59.1	132.4
158.9	120.4	60.0	41.4	57.9	67.3	125.3
317.5	19.1	9.5	30.2	31.6	32.8	1144.2
317.0	75.3	37.5	31.5	36.7	41.3	986.0
315.5	132.0	65.7	32.4	41.5	49.1	885.6
316.4	188.5	93.8	33.1	46.1	56.2	859.4
315.6	312.8	155.7	35.6	57.1	73.3	699.0
474.4	17.9	8.9	30.0	30.9	32.1	2158.5
473.7	75.2	37.5	31.1	34.6	39.3	1973.9
473.5	168.1	83.7	32.3	40.0	50.3	1792.6
472.6	294.7	146.7	33.8	47.4	64.6	1587.4
471.4	462.6	230.3	36.4	57.7	82.0	1351.4
629.3	18.4	9.2	30.2	30.8	31.9	3236.1
629.1	76.4	38.0	30.8	33.4	37.9	3073.4
628.4	173.4	86.3	31.7	37.7	47.6	2858.4
627.6	294.6	146.7	32.9	43.1	59.1	2605.2
627.0	469.3	233.7	34.9	51.2	75.9	2340.4
784.2	18.9	9.4	30.1	30.6	31.7	4520.3
783.8	75.2	37.4	30.7	32.8	37.2	4330.2
783.5	168.2	83.7	31.4	36.1	45.7	4080.2
782.7	290.6	144.7	32.5	40.6	56.7	3789.9
781.7	456.2	227.1	33.8	46.5	70.2	3514.2

Table C.4

Microchannels with fins

G	**q"$_b$**	**q"$_{ht}$**	**T$_{in}$**	**T$_{out}$**	**T$_w$**	**ΔP**
kg/m^2 S	**W/m^2**	**W/m^2**	**°C**	**°C**	**°C**	**Pa**
158.1	15.0	7.2	31.6	33.7	34.7	310.6
158.0	42.5	20.3	33.0	38.7	41.7	258.4
157.9	63.4	30.2	34.5	43.1	46.9	220.8
157.8	102.3	48.8	37.9	51.7	57.7	171.6
157.5	134.2	64.1	40.8	59.0	66.6	135.6
314.4	19.6	9.4	30.9	32.2	33.2	1228.4
314.0	87.5	41.8	31.6	37.5	41.8	1081.7
313.1	138.4	66.0	33.1	42.5	49.1	973.4
312.6	198.3	94.6	33.5	47.0	55.8	887.2
312.3	314.5	150.1	36.9	58.4	71.1	700.6
469.8	18.2	8.7	30.8	31.6	32.6	2665.9
469.5	82.2	39.2	31.5	35.2	39.2	2509.6
468.9	198.3	94.6	32.4	41.4	50.0	2149.7
468.0	348.9	166.5	34.2	50.1	64.7	1906.3
466.9	512.1	244.4	36.3	59.6	80.7	1738.7
624.3	18.5	8.8	30.8	31.4	32.4	3899.8
624.0	83.9	40.0	31.1	34.0	37.9	3477.7
623.4	191.8	91.5	31.9	38.5	47.0	3300.9
622.6	336.4	160.6	32.8	44.3	59.2	3129.8
621.9	507.3	242.1	33.4	50.7	72.2	2853.0
778.6	19.7	9.4	30.7	31.2	32.1	5687.2
778.3	83.5	39.9	30.9	33.2	36.8	5472.1
777.8	182.1	86.9	31.3	36.3	43.9	5249.3
777.0	334.2	159.5	32.2	41.4	54.9	4971.0
776.0	515.4	246.0	33.0	47.2	67.5	4675.4

REFERENCES

1. Moore G.E. (1965), Cramming More components onto integrated circuits, Electronics, 38, 114-117.
2. Ali R. (2010), Phase change phenomena during fluid flow in microchannels, Ph.D. Thesis, Royal Institute of Technology, Stockholm, Sweden.
3. Pop E., Goodson K.E. (2006), Thermal phenomena in nanoscale transistors, ASME J Ele Packag, 128, 102-108.
4. Phillips R. J. (1988), Microchannels heat sinks, Lincoln Lab J, 1, 31–47.
5. Lee J., Mudawar I. (2008), Fluid flow and heat transfer characteristics of low temperature two-phase microchannel heat sink-part 1: experimental methods and flow visualization results, Int J Heat Mass Transf, 51, 4315–4326.
6. Boyd R.D. (1985), Subcooled flow boiling critical heat flux and its application to fusion energy components. part 1. a review of fundamentals of chf and related data base, Fusion Tech, 7, 7–30.
7. Lee J., Mudawar I. (2009), Low-temperature two-phase microchannel cooling for high-heat-flux thermal management of defence electronics, IEEE Tran Compon Packag Tech, 32, 453-465.
8. Zhang L. (2002), Phase change phenomena in silicon microchannel heat sink for ic chip cooling, PhD Thesis, Department of Mechanical Engineering,. Stanford University.
9. http://en.wikipedia.org/wiki/Computer_cooling
10. http://www.mkicorp.com/a-t-heatpipes.asp
11. Garner S. D. (1996), Heat pipes for electronics cooling applications, Ele Cooling, 2(3). Available at: https://www.electronics-cooling.com/1996/09/heat-pipes-for-electronics-cooling-applications/

12. Brunschwiler T., Rohuizen H., Fabbri M., Kloter U., Michel B., Bezama R. J., Natarajan G., (2006) Direct liquid jet impingement cooling with micron-sized nozzle array and distributed return architecture, ITHERM, San Diego, CA, USA.
13. Colgan E.G., Furman B., Gaynes M., LaBianca N., Magerlein J.H., Polastre R., Bezama R., Marstonand K., Schimidt R. (2007), High performance and subambient silicon microchannel cooling, ASME J Heat Transf, 129, 1046-1051.
14. Mudawar I. (2011), Two-phase microchannel heat sinks: theory, applications, and limitations, AMSE J Ele Packag, 133, DOI: 10.1115/1.4005300
15. Kandlikar S.G. (2005), High flux heat removal with microchannels—a roadmap of challenges and opportunities, Heat Transf Engg, 26, 5–14.
16. http://www.research.ibm.com/articles/superMUC.shtml.
17. Tuckerman D.B., Pease R.F.W. (1981), High-performance heat sinking for VLSI, IEEE Ele Devi Lett, 2, 126-129.
18. Keyes R.W. (1984), Heat transfer in forced convection through fins, IEEE Trans Ele Devi, 311, 1218-1221
19. Missaggia I.J., Walpole J.N., Liau Z.L., Phillips R.J. (1989), Microchannel heat sinks for two-dimensional high-power-density diode laser arrays, IEEE J Quantum Ele, 25 1988-1992.
20. Kandlikar S.G., Grande W.J., (2002) Evolution of microchannel flow passages—Thermohydraulic performance and fabrication technology, ASME International Mechanical Engineering Congress & Exposition, November 17-22 New Orleans, Louisiana, 2002.
21. Kandlikar S.G., Grande W.J. (2003), Evolution of microchannel flow passage thermohydraulic performance and fabrication technology, Heat Transf Engg, 24, 3–17.

22. Mehendale S.S., Jacobi A.M., Shah R.K.(200), Fluid flow and heat transfer at micro- and meso-scales with applications to heat exchanger design, Appl Mech Rev, 53, 175–193.
23. Cornwell K., P Kew.A. (1993), Boiling in small parallel channels, Energy Efficiency in Process Technology, Elseviers, Chap. 7, 624–638.
24. Kew P., Cornwell K. (1997), Correlation for prediction of boiling heat transfer in small diameter channel, J Therm Engg, 17, 705-715.
25. Papautsky I., Brazzle J., Swerdlow H., Frazier A.B. (1998), A low-temperature IC compatible process for fabricating surface-micromachined metallic microchannels, J Microelectromechanical Sys, 7, 267-273.
26. Lee P.S., Garimella S.V., Liu D. (2005), Investigation of heat transfer in rectangular microchannels, Int J Heat Mass Transf, 48, 1688–1704.
27. Wu H.Y., Cheng P. (2005), Condensation flow pattern in silicon microchannels, Int J Heat mass Transf, 48, 2186-2197.
28. Mei F., Parida P.R., Jiang J., Meng W.J., Ekkad S.V.(2008), Fabrication, assembly, and testing of Cu- and Al- based microchannel heat exchanger, J microelectromechanical sys, 17, 869-881.
29. Wu J., Shi M., Chen Y., Li X. (2010), Visualization study of steam condensation in wide rectangular silicon microchannels, Int J Therm Sci, 49, 922-930.
30. Chen T., Garimella S.V. (2011), Local heat transfer distribution and effect of instabilities during flow boiling in a silicon microchannel heat sink, Int J Heat Mass Transf, 54, 3179-3190.
31. Lee J.Y., Kim M.H., Kaviany M., Son S.Y. (2011), Bubble nucleation in microchannel flow boiling using single artificial cavity, Int J Heat Mass Transf, 54, 5139–5148.

32. Hwang D.J., Choi T.Y., Grigoropoulos C.P. (2004), Liquid assisted femtosecond laser drilling of straight and three-dimensional micro-channels in glass, Appl Phys A, 79 605–612.
33. Peng X.F., Wang B.X. (1993), Forced convection and flow boiling heat transfer for liquid flowing through microchannels, Int J Heat transf, 36, 3421-3427.
34. Qu W., Mudawar I. (2003), Flow boiling heat transfer in two-phase micro-channel heat sinks—I. Experimental investigation and assessment of correlation methods, Int J Heat Mass Transf, 46, 2755–2771.
35. Qu W., Mudawar I. (2004), Measurement and correlation of critical heat flux in two-phase micro-channel heat sinks, Int J Heat Mass Transf, 47, 2045–2059.
36. Steinke M.E., Kandlikar S.G. (2004), An experimental investigation of flow boiling characteristics of water in parallel microchannels, ASME J Heat Transf, 126, 518-526.
37. Coleman J.W., Krause P.E. (2004), Two phase pressure losses of R134a in microchannel tube headers with large free flow area ratios, Exp Therm Fluid Sci, 28, 123–130.
38. Lee P.C., Tseng F.G., Pan C. (2004), Bubble dynamics in microchannels. Part I: Single microchannel, Int J Heat Mass Transf, 47, 5575–5589.
39. Li H.Y., Tseng F.G., Pan C. (2004), Bubble dynamics in microchannels. Part II: Two parallel microchannels, Int J Heat Mass Transf, 47, 5591–5601.
40. Lee J., Mudawar I. (2005), Two-phase flow in high-heat-flux micro-channel heat sink for refrigeration cooling applications: Part I—Pressure drop characteristics, Int J Heat Mass Transf, 48, 928–940.

41. Kosar A., Kuo C.J., Peles Y. (2005), Boiling heat transfer in rectangular microchannels with reentrant cavities, Int J Heat Mass Transf, 48, 4867–4886.
42. Ling Z. Y., Ding J. N., Yang J. C., Liu Y., Fan Z., Yang P., Zhuang Z. W., (2006) Experimental study of flow characteristics of distilled water under pressure driven in microchannel, Proceedings First IEEE Int Conference on Nano/Micro Engineered and Molecular Systems, Zhuhai, China, 182-186.
43. Chen T., Garimella S.V. (2006), Measurements and high-speed visualizations of flow boiling of a dielectric fluid in a silicon microchannel heat sink, Int J Multiphase Flow, 32, 957–971.
44. Yun R., Heo J.Y., Kim Y. (2006), Evaporative heat transfer and pressure drop of R410A in microchannels, Int J Refrige, 29, 92–100.
45. Sobierska E., Kulenovic R., Mertz R., Groll M.(2006), experimental results of flow boiling of water in a vertical microchannel, Expt Therm Fluid Sci, 31, 111–119.
46. Huh C., Kim J., Kim M.H. (2007), Flow pattern transition instability during flow boiling in a single microchannel, Int J Heat Mass Transf, 50, (2007) 1049–1060.
47. Qi S.L., Zhang P., Wang R. Z., Xu L.X.(2007), Single-phase pressure drop and heat transfer characteristics of turbulent liquid nitrogen flow in micro-tubes, Int J Heat Mass Transf, 50, 1993–2001.
48. Wang G., Cheng P., Bergles A.E. (2008), Effects of inlet/outlet configurations on flow boiling instability in parallel microchannels, Int J Heat Mass Transf, 51, 2267–2281.
49. Agostini B., Revellin R., Thome J.R. (2008), Elongated bubbles in microchannels. Part I: Experimental study and modeling of elongated bubble velocity, Int J Multiphase Flow, 34, (2008) 590–601.

50. Singh S.G., Kulkarni A., Duttagupta S.P., Puranik B.P., Agrawal A. (2008), Impact of aspect ratio on flow boiling of water in rectangular microchannels, Exp Therm Fluid Sci, 33, 153–160.
51. Ergu O.B., Sara O.N., Yapici S., Arzutug M.E. (2009), Pressure drop and point mass transfer in a rectangular microchannel, Int Comm Heat Mass Transf, 36, 618–623.
52. Schilder B., Man S.Y.C., Kasagi N., Hardt S., Stephan P. (2010), Flow visualization and local measurement of forced convection heat transfer in a microtube, ASME J Heat Transf, 132, (DOI: 10.1115/1.4000046).
53. Krishnamurthy S., Peles Y. (2010), Flow boiling heat transfer on micro pin fins entrenched in a microchannel, ASME J Heat Transf, 132, (DOI: 10.1115/1.4000878).
54. Balasubramanian K., Lee P.S., Jin L.W., Chou S.K., Teo C.J., Gao S. (2011), Experimental investigations of flow boiling heat transfer and pressure drop in straight and expanding microchannels - A comparative study, Int J Therm Sci, 50, 241–2421.
55. Megahed A. (2011), Experimental investigation flow boiling characteristics in a cross-linked microchannel heat sink, Int J Multiphase Flow, 37, 380–393.
56. Barlak S., Yapici S., Sara O.N. (2011), Experimental investigation of pressure drop and friction factor for water flow in microtubes, Int J Therm Sci, 50, 361-368.
57. Edel Z.J., Mukherjee A. (2011), Experimental investigation of vapor bubble growth during flow boiling in a microchannel, Int J Multiphase Flow, 37, 1257–1265.
58. Lu C.T., Pan C. (2011), Convective boiling in a parallel microchannel heat sink with a diverging cross section and artificial nucleation sites, Exp Therm Fluid Sci, 35, 810–815.

59. Park C.Y., Jang Y., Kim B., Kim Y. (2012), Flow boiling heat transfer coefficients and pressure drop of FC-72 in microchannels, Int J Multiphase Flow, 39, 45–54.
60. Thome J. R., (2004) Engineering data book III, Wolverine Tube Inc, Lausanne, Switzerland, Chap. 12.
61. Pfahler J., Harley J., Bau H., Zemel J. (1990), Liquid transport in micron and submicron channels, SensActu, 22, 43l-434.
62. Megahed A., Hassan I. (2009), Two-phase pressure drop and flow visualization of FC-72 in a silicon microchannel heat sink, Int J Heat Fluid Flow, 30, 1171-1182.
63. Zhang P., Fu X. (2009), Two-phase flow characteristics of liquid nitrogen in vertically upward 0.5 and 1.0 mm micro-tubes: visualization studies, Cryogenics, 49, 565–575.
64. Kawahara A., Sadatomi M., Nei K., Matsuo H. (2009), Experimental study on bubble velocity, void fraction and pressure drop for gas–liquid two-phase flow in a circular microchannel, Int J Heat Fluid Flow, 30, 831–841.
65. Choi C., Kim M. (2011), Flow pattern based correlations of two-phase pressure drop in rectangular microchannels, Int J Heat Fluid Flow, 32, 1199–1207.
66. Choi C.W., Yu D.I., Kim M.H. (2011), Adiabatic two-phase flow in rectangular microchannels with different aspect ratios: part i – flow pattern, pressure drop and void Fraction, Int J Heat Mass Transf, 54, 616–624.
67. Kasza K.E., Didascalou T., Wambsganss M.W., Microscale flow visualization of nucleate boiling in small channels: Mechanisms influencing heat transfer, Proceeding International Conference on Compact Heat Exchanges for the Process Industries, New York, Begell House Inc., 343– 352.

68. Chung P.M.Y., Kawaji M. (2004), The effect of channel diameter on adiabatic two-phase flow characteristics in microchannels, Int J Multiphase Flow, 30, 735–761.
69. Lee J., Mudawar I. (2005), Two-phase flow in high-heat-flux micro-channel heat sink for refrigeration cooling applications: Part II—Heat transfer characteristics, Int J Heat Mass Transf, 48, 941–955.
70. Kashid M.N., Gerlach I., Goetz S., Franzke J., Acker J.F., Platte F., Agar D.W., Turek S. (2005), Internal circulation within the liquid slugs of liquid–liquid slug flow capillary microreactor, Ind Eng Chem Res, 44, 5003–5010.
71. Barber J., Brutin D., Sefiane K., Tadrist L. (2010), Bubble confinement in flow boiling of FC-72 in a ‘‘rectangular” microchannel of high aspect ratio, Exp Therm Fluid Sci, 34, 1375–1388.
72. David M.P., Steinbrenner J.E., Miler J., Goodson K.E. (2011), Adiabatic and diabatic two-phase venting flow in a microchannel, Int J Multiphase Flow, 37, 1135–1146.
73. Hewitt G.F., Roberts D.N. (1969), Studies of two-phase flow patterns by simultaneous X-ray and flash photography, Atomic Energy Research Establishment, Harwell, Report No. AERE-M 2159.
74. Taitel Y., Dukler A.E. (1976), A model for predicting flow regime transitions in horizontal and near horizontal gas-liquid flow, AIChE J, 22, 47–55.
75. Kattan N., Thome J.R., Favrat D. (1998), Flow boiling in horizontal tubes—Part I: Development of a diabatic two-phase flow pattern map, ASME J Heat Transf, 120, 140–147.
76. Kattan N., Thome J.R., Favrat D. (1998), Flow boiling in horizontal tubes—Part II: New heat transfer data for five refrigerants, ASME J Heat Transf, 120, 148–155.

77. Kattan N., Thome J.R., Favrat D. (1998), Flow boiling in horizontal tubes—Part III: Development of a new heat transfer model based on flow patterns, ASME J Heat Transf, 120, 156–165.
78. Triplett K.A., Ghiaasiaan S.M., Abdel-Khalik S. I., Sadowski D. L. (1999), Gas-liquid two-phase flow in microchannels part i: two-phase flow patterns, Int J Multiphase Flow, 25, 377-394.
79. Harirchian T., Garimella S.V. (2010), A comprehensive flow regime map for microchannel flow boiling with quantitative transition criteria, Int J Heat Mass Transf, 53, 2694-2702.
80. Sur A., Liu, D. (2012), Adiabatic air-water two-phase flow in circular microchannels, Int J Therm Sci, 53, 18-34.
81. Liu D., Lee P.S., Garimella S.V. (2005), Prediction of the onset of nucleate boiling in microchannels flow, Int J Heat Mass Transf, 48, 5134–5149.
82. Hsu Y.Y. (1962), On the size range of active nucleation cavities on a heating surface, ASME J Heat Transf, 84, 207-216.
83. Mukherjee A., Kandlikar S.G., Edel Z.J. (2011), Numerical study of bubble growth and wall heat transfer during flow boiling in a microchannels, Int J Heat Mass Transf, 54, 3702-3718.
84. Davis E.J., Anderson G.H. (1966), The incipience of nucleate boiling in forced convection flow, AIChE J, 12, 774–780.
85. Kandlikar S.G., Spiesman P.H. (1997), Effect of surface characteristics on flow boiling heat transfer, Paper presented at the Engineering Foundation Conference on Convective and Pool Boiling, May 18–25, Irsee, Germany.
86. Bogojevic D., Sefiane K., Duursma D., Walton A.J. (2013), Bubble dynamics and flow boiling instabilities in microchannels, Int J Heat Mass Transf, 58 663–675.

87. Yin L., Jia L., Guan P (2016), Bubble confinement and deformation during flow boiling in microchannel, Int J Heat Mass Transf, 70 47-52.
88. Lee M., Wong Y.Y., Wong M., Zohar Y. (2003), Size and shape effects on two-phase flow patterns in microchannel forced convection boiling, J Micromech Microeng, 13, 155–164.
89. Fu X., Zhang P., Huang C.J., Wang R.Z. (2010), Bubble growth, departure and the following flow pattern evolution during flow boiling in a mini-tube, Int J Heat Mass Transf, 53, 4819–4831.
90. Gedupudi S., Zu Y.Q., Karayiannis T.G., Kenning D.B.R., Yan Y.Y. (2011), Confined bubble growth during flow boiling in a mini/micro-channel of rectangular cross-section Part I: Experiments and 1-D modeling, Int J Therm Sci, 50, 250-266.
91. Yin L., Jia L., Guan P., Liu F. (2012), An experimental investigation on the confined and elongated bubbles in subcooled flow boiling in a single microchannel, J Therm Sci, 21, 549−556.
92. Tuo H., Hrnjak P. (2014), Visualization and measurement of periodic reverse flow and boiling fluctuations in a microchannel evaporator of an air-conditioning system, Int J Heat Mass Transf, 71 639–652.
93. Van Helden W.G.J.V., Van Der Geld C.W.M., Boot, P.G.M. (1995), Forces on bubbles growing and detaching in flow along a vertical wall, Int J Heat Mass Transf, 38, 2075 -2088.
94. Zeng L.Z., Klausner J.F., Bernhard D.M., Mei R. (1993), A unified model for the prediction of bubble detachment diameters in boiling systems-ii. flow boiling, Int J Heat Mass Transf, 36, 2271-2279.
95. Yeoh G.H., Tu J.Y. (2005), A unified model considering force balances for departing vapor bubbles and population balance in subcooled boiling flow, Nucl Eng Des, 235, 1251–1265.

96. Qu W., Mudawar I. (2002), Prediction and measurement of incipient boiling heat flux in micro-channel heat sinks, Int J Heat Mass Transf, 45, 3933–3945.
97. Kandlikar S.G. (2001), A Theoretical model to predict pool boiling chf incorporating effects of contact angle and orientation, ASME J Heat Transf, 123, 1071-1079.
98. Kandlikar S.G. (2004), Heat transfer mechanisms during flow boiling in microchannels, ASME J Heat Transf, 126, 8-16.
99. Kandlikar S.G. (2010), Scale effects on flow boiling heat transfer in microchannels: a fundamental perspective, Int J Therm Sci, 49, 1073-1085.
100. Kandlikar S.G. (2010), A scale analysis based theoretical force balance model for critical heat flux (CHF) during saturated flow boiling in microchannels and minichannels, ASME J Heat Transf, 132, (DOI: 10.1115/1.4001124).
101. Mukherjee A., Kandlikar S.G. (2005), Numerical simulation of growth of a vapor bubble during flow boiling of water in a microchannels, Microfluid Nanofluid, 1, 137–145.
102. Thome J.R., Dupont V., Jacobi A.M. (2004), Heat transfer model for evaporation in microchannels. part i: presentation of the model, Int J Heat Mass Transf, 47, 3375–3385.
103. Zhuan R., Wang W. (2010), Simulation on nucleate boiling in microchannel, Int J Heat Mass Transf, 53, 502–512.
104. Wang E.N., Devasenathipathy S., Li, H., Hidrovo C.H., Santiago J.G., Goodson K.E., Kenny T.W. (2006), A hybrid method for bubble geometry reconstruction in two-phase microchannels, Exp Fluids, 40, 847-858.
105. Qu W., Mudawar I. (2002), Experimental and numerical study of pressure drop and heat transfer in a single-phase micro-channel heat sink, Int J Heat Mass Transf, 45, 2549–2565.

106. Akbari M., Sinton D., Bahrami M. (2009), Pressure drop in rectangular microchannels as compared with theory based on arbitrary cross section, ASME J Fluids Engg, 131, (DOI: 10.1115/1.3077143).

107. Peiyi W., Little W.A. (1983), Measurement of friction factors for the flow of gases in very fine channels used for microminiature Joule-Thomason refrigerator, Cryogenics, 23, 73-277.

108. Lee J., Mudawar I. (2008), Fluid flow and heat transfer characteristics of low temperature two-phase micro-channel heat sinks – Part 2. Subcooled boiling pressure drop and heat transfer, Int J Heat Mass Transf, 51, 4327–4341.

109. Qu W., Mudawar I. (2003), Measurement and prediction of pressure drop in two-phase micro-channel heat sinks, Int J. Heat Mass Transf, 46, 2737–2753.

110. Lee P.S., Garimella S.V. (2008), Saturated flow boiling heat transfer and pressure drop in silicon microchannel arrays, Int J Heat Mass Transf, 51, 789–806.

111. Phan H.T., Caney N., Marty P., Colasson S., Gavillet J. (2011), Flow boiling of water in a minichannel: The effects of surface wettability on two-phase pressure drop, Appl Therm Engg, 31, 1894-1905.

112. Bowers M.B., Mudawar I. (1994), High flux boiling in low flow rate, low pressure drop mini-channel and microchannel heat sink, Int J Heat Mass Transf, 37, 331-332.

113. Wang B.X., Peng X.F. (1994), Experimental Investigation on liquid forced convection heat transfer through microchannels, Int J Heat transf, 37, 73-82.

114. Herwig H., Mahulikar S.P. (2006), Variable property effects in single-phase incompressible flows through microchannels, Int J Therm Sci, 45, 977- 981.

115. Sui Y., Lee P.S., Teo C.J. (2011), An experimental study of flow friction and heat transfer in wavy microchannels with rectangular cross section, Int J Therm Sci, 50, 2473-2482.
116. Collier J.G., Thome J.R., (1994), Convective boiling and condensation, Third ed., Oxford University Press Oxford, (ISBN 0-19-856282-9).
117. Yen T.H., Shoji M., Takemura F., Suzuki Y., Kasagi N. (2006), Visualization of convective boiling heat transfer in single microchannels with different shaped cross-sections, Int J Heat Mass Transf, 49, 3884–3894.
118. Zhuan R., Wang W. (2013), Boiling heat transfer characteristics in a microchannel array heat sink with low mass flow rate, Appl Therm Engg, 51, 65-74
119. Kosar A., Peles Y. (2007), Boiling heat transfer in a hydrofoil-based micro pin fin heat sink, Int J Heat Mass Transf, 50 1018-1034.
120. Prajapati Y.K., Pathak M., , Khan M.K. (2015), A comparative study of flow boiling heat transfer in three different configurations of microchannels, Int J Heat Mass Transf, 85, 711–722.
121. Law M.,, Lee P.S. (2015), A comparative study of experimental flow boiling heat transfer and pressure characteristics in straight- and oblique-finned microchannels, IntJ Heat Mass Transf, 85, 797–810.
122. Choo K., Kim S.J. (2011), Heat transfer and fluid flow characteristics of nonboiling two-phase flow in microchannels, ASME J Heat Transf, 133, (DOI: 10.1115/1.4004208).
123. Wang C.C., Chang W.J., Dai C.D., Lin Y.T., Yang K.S. (2012), Effect of inclination on the convective boiling performance of a microchannel heat sink using HFE-7100, Exp Therm Fluid Sci, 36, 143–148.

124. Vidmar R.J., Barker R.J. (1998), Microchannel cooling for a high-energy particle transmission window, an RF transmission window, and VLSI heat dissipation, IEEE Tran Plasma Sci, 26, 1031-1043.
125. Nacke R., Northcutt B., Mudawar I. (2011), Theory and experimental validation of cross-flow micro-channel heat exchanger module with reference to high Mach aircraft gas turbine engines, Int J Heat Mass Transf, 54 , 1224–1235
126. Koyuncuoglu A., Jafari R., Ozyurt T.O., Kulah H. (2012), Heat transfer and pressure drop experiments on CMOS compatible microchannel heat sinks for monolithic chip cooling applications, Int J Therm Sci, 56, 77-85.
127. Bertsch S.S., Groll E.A., Garimella S.V. (2009), A composite heat transfer correlation for saturated flow boiling in small channels, Int J Heat Mass Transf, 52, (2009) 2110– 2118.
128. Qi S.L., Zhang P., Wang R.Z., Xu L.X. (2007), Flow boiling of liquid nitrogen in micro-tubes: Part I – The onset of nucleate boiling, two-phase flow instability and two-phase flow pressure drop, Int J Heat Mass Transf, 50, 4999–5016.
129. Chang K.H., Pan C. (2007), Two-phase flow instability for boiling in a microchannel heat sink, Int J Heat Mass Transf, 50, 2078–2088.
130. Bogojevic D., Sefiane K. , Walton A.J., Lin H., Cummins G. (2009), Two-phase flow instabilities in a silicon microchannels heat sink, Int J Heat Fluid Flow, 30, 854–867.
131. Bergles A.E., Kandlikar S.G. (2005), On the nature of critical heat flux in microchannels, ASME J Heat Transf, 127, 101-107.
132. Kandlikar S.G. (2006), Nucleation characteristics and stability considerations during flow boiling in microchannels, Exp Therm Fluid Sci, 30, 441–447.

133. Tuo H., Hrnjak P. (2013), Periodical reverse flow and boiling fluctuations in a microchannel evaporator of an air-conditioning system, Int J Refrig, 36, 1263-1275.
134. Kuan W.K., Kandlikar S.G. (2007), Experimental study on the effect of stabilization on flow boiling heat transfer in microchannels, Heat Transf Engg, 28, 746–752.
135. Kuo C.J., Peles Y. (2008), Flow boiling instabilities in microchannels and means or mitigation by reentrant cavities, ASME J Heat Transf, 130, (DOI: 10.1115/1.2908431).
136. Xu J., Liu G., Zhang W., Li Q., Wang B. (2009), Seed bubbles stabilize flow and heat transfer in parallel microchannels, Int J Multiphase Flow, 35, 773-790.
137. Liu G., Xu J., Yang Y., Zhang W. (2010), Active control of flow and heat transfer in silicon microchannels, J Micromech Microengg, 20, 1-16.
138. Thome J.R., Dupont V., (2007) Heat transfer assembly, European Patent EP 1779052 B1.
139. Han Y., Shikazono N. (2011), Stabilization of flow boiling in a micro tube with air injection, Exp Therm Fluid Sci, 35, 1255-1264.
140. Tuo H., Hrnjak P. (2013), New approach to improve performance by venting periodic reverse vapor flow in microchannel evaporator, Int J Refrig, 36, 2187-2195.
141. Yin J.M., Bullard C.W., Hrnjak P.S. (2002), Single phase pressure drop measurements in a microchannel heat exchanger, Heat Transf Engg, 23, 1–10.
142. Tonomura O., Tanaka S., Noda M., Kano M., Hasebe S., Hashimoto I. (2004), CFD-based optimal design of manifold in plate-fin microdevices, Chem Engg J, 101 , 397–402.
143. Cho E.S., Choi J.W. , Yoon J.S., Kim M.S. (2010), Experimental study on microchannel heat sinks considering mass flow

distribution with non-uniform heat flux conditions, Int J Heat Mass Transf, 53, 2159–2168.

144. Cho E.S., Choi J.W., Yoon J.S., Kim M.S. (2010), Modeling and simulation on the mass flow distribution in microchannel heat sinks with non uniform heat flux conditions, Int J Heat Mass Transf, 53, 1341- 1348.

145. Kumaraguruparan G., Kumaran R.M., Sornakumar T., Sundararajan T. (2011), A numerical and experimental investigation of flow maldistribution in a microchannel heat Sink, Int Comm Heat Mass Transf, 38, 1349 - 1353.

146. Tuo H., Hrnjak P. (2013), Effect of the header pressure drop induced flow maldistribution on the microchannel evaporator performance, Int J Refrig, 36, 2176-2186.

147. Szczukiewicz S., Borhani N., Thome J.R. (2013), Two-phase flow operational maps for multi-microchannel evaporators, Int J Heat Fluid Flow, 42, 176-189.

148. Kakac S., Bon B.A. (2008), A review of two-phase flow dynamic instabilities in tube boiling systems, Int J Heat Mass Transf, 51, 399–433.

149. Zhang T., Tong T., Chang J.Y., Peles Y., Prasher R., Jensen M.K., Wen J.T., Phelan P. (2009), Ledinegg instability in microchannels, Int J Heat Mass Transf, 52, 5661–5674.

150. Lee J., Mudawar I. (2009), Critical heat flux for subcooled flow boiling in micro-channel heat sinks, Int J Heat Mass Transf, 52, 3341–3352.

151. Kutateladze S.S., Leontev A.I., (1966), Some applications of the asymptotic theory of the turbulent boundary layer”, Third Int Heat Trans Conference, 3, AIChE, New York, pp. 1–6.

152. Weisman J., Pei B.S. (1983), Prediction of critical heat flux in flow boiling at low qualities, Int J Heat Mass Transf, 26, 1463–1477.

153. Lee C.H., Mudawar I. (1988), A mechanistic critical heat flux model for subcooled flow boiling based on local bulk flow conditions, Int J Multiphase Flow, 14, 711–728.
154. Kivisalu M.T., Gorgitrattanagul P., Narain A. (2014), Results for high heat-flux flow realizations in innovative operations of milli-meter scale condensers and boilers, Int J Heat Mass Transf, 75, 381-398.
155. Shah M.M. (2015), Improved general correlation for chf in uniformly heated vertical annuli with upflow, Heat Trans Engg, 37, (DOI:10.1080/01457632.2015.1060765).
156. Qi S.L., Zhang P., Wang R.Z., Xu L.X. (2007), Flow boiling of liquid nitrogen in micro-tubes: part ii – heat transfer characteristics and critical heat flux, Int J Heat Mass Transf, 50, 5017–5030.
157. Wojtan L., Revellin R., Thome J.R. (2006), Investigation of saturated critical heat flux in a single, uniformly heated microchannel, Exp Therm Fluid Sci, 30, 765-774.
158. Miner M. (2013), Microchannel flow boiling enhancement via cross-sectional expansion, Ph. D. Thesis, Arizona State University, Tempe, United States.
159. Katto Y. (1978), A generalized correlation of critical heat flux for the forced convection boiling in vertical uniformly heated round tubes, Int J Heat Mass Transf, 21, 1527-1542.
160. Ong C.L., Thome J.R. (2011), Macro-to-microchannel transition in two-phase flow: part 2 – flow boiling heat transfer and critical heat flux, Exp Therm Fluid Sci, 35, 873–886.
161. Fu B.R., Lee C.Y., Pan C. (2013), The effect of aspect ratio on flow boiling heat transfer of hfe-7100 in a microchannel heat sink, Int J Heat Mass Transf, 58, 53–61.
162. Kosar A., Peles Y. (2007), Critical heat flux of r-123 in silicon-based microchannels, ASME J Heat Transf, 129, (DOI: 10.1115/1.2712852).

163. Kuan W.K. (2006), Experimental study of flow boiling heat transfer and critical heat flux in microchannels, Ph. D. Thesis, Rochester Institute of Technology, New York, United States.

164. Agostini B., Revellin R., Thome J.R., Fabbri M., Michel B., Calmi D., Kloter U. (2008), High heat flux flow boiling in silicon multi-microchannels – part iii: saturated critical heat flux of r236fa and two-phase pressure drops, Int J Heat Mass Transf, 51, 5426–5442.

165. Park J.E. (2008), Critical heat flux in multi-microchannel copper elements with low pressure refrigerants, Ph. D. Thesis, Ecole Polytechnique Federale De Lausanne, Lausanne, Switzerland.

166. Mauro, A.W., Thome J.R., Toto D., Vanoli G.P. (2010), Saturated critical heat flux in a multi-microchannel heat sink fed by a split flow system, Exp Therm Fluid Sci, 34, 81–92.

167. Basu S. (2009) Heat transfer characteristics for flow boiling of r134a in horizontal circular microtubes, M. S. Thesis, Rensselaer Polytechnic Institute, New York, United states.

168. Roday A.P. (2007), Study of the critical heat flux condition in microtubes, Ph. D. Thesis, Rensselaer Polytechnic Institute, New York, United states.

169. Hsieh S.S., Lin C.Y. (2012), Correlation of critical heat flux and two-phase friction factor for subcooled convective boiling in structured surface microchannels, Int J Heat Mass Transf, 55, 32–42.

170. Roach G.M., Abdel-Khalik S.I., Ghiaasiaan S.M., Dowling M.F., Jeter S.M. (1999), Low-flow critical heat flux in heated microchannels, Nuclear Sci Engg, 131, 411–425.

171. Kuan W.K., Kandlikar S.G. (2008), Experimental study and model on critical heat flux of refrigerant-123 and water in microchannels, ASME J Heat Transf, 130, (DOI: 10.1115/1.2804936).

172. Revellin R., Thome J.R. (2008), A theoretical model for the prediction of the critical heat flux in heated microchannels, Int J Heat Mass Transf, 51, 1216–1225.

173. Revellin R., Quiben J.M., Bonjour J., Thome J.R. (2008), Effect of local hot spots on the maximum dissipation rates during flow boiling in a microchannel, IEEE Trans Compon Packag Tech,, 31, 407-416.

174. Plesset M.S., Zwick S.A. (1954), Growth of vapor bubbles in superheated liquids, Appl Phys, 25, 493–500.

175. Forster H.K., and Zuber N. (1954), Growth of a vapor bubbles in superheated liquid, Appl Phys, 25, 474–478.

176. Plesset M.S., Prosperetti A. (1977), Bubble dynamics and cavitation, Ann Rev Fluid Mech, 9, 145-185.

177. Fu B.R., Pan C. (2009), Bubble growth with chemical reactions in microchannels, Int J Heat Mass Transf, 52, 767–776.

178. Lee J.Y., Kim M.H., Kaviany M., Son S.Y. (2011), Bubble nucleation in microchannels flow boiling using single artificial cavity, Int J Heat Mass Transf, 54, 5139–5148.

179. Thome, J. R. (2004), Engineering data book III, Wolverine Tube, Inc., Lausanne, Switzerland, Chap. 17.

180. Hewitt, G. F., (1982), Measurement of void fraction-handbook of multiphase systems, McGraw-Hill, New York.

181. Fletcher N.H. (1959), On ice-crystal production by aerosol particles, J Meteorology, 16, 173-180.

182. http://rkt.chem.ox.ac.uk/lectures/liqsolns/liquid_surfaces.html.

183. Xavier, C., (1993), Fortran 77 and numerical methods, New Age, New Delhi, India.

184. Shakir, S., Thome, J.R., (1986), Boiling nucleation of mixtures on smooth and enhanced surfaces, Proceeding eighth International Heat Transfer Conference, San Francisco, 4, pp. 2081–2086.

185. Jensen, M. J. (2002), Bubbles in microchannels, Master Thesis, Technical University of Denmark, Kongens Lyngby, Denmark.

186. Meder, S. (2007), Study on bubble growth rate in a single microchannel heat exchanger with high-speed cmos-camera, Master Thesis, Swiss Federal Institute Of Technology Zurich And Stanford University California.

187. Griffith, P., Clark, J.A., Rohsenow, W.M., (1958), 'Void volumes in subcooled boiling system, Technical Report No. 12, Massachusetts Institute of Technology, Cambridge, Massachusetts.

188. Basu N., Warrier G.R., Dhir V.K. (2005), Wall heat flux partitioning during subcooled flow boiling: part i—model development, ASME J Heat Transf, 127, 131-140.

189. Ahmadi R., Ueno T., Okawa T. (2012), Bubble dynamics at boiling incipience in subcooled upward flow boiling, Int J Heat Mass Transf, 55, 488-497.

190. Basu N., Warrier G.R., Dhir V.K. (2005), Wall heat flux partitioning during subcooled flow boiling: part ii—model validation, ASME J Heat Transf, 127, 141-148.

191. Yeoh G.H., Cheung S.C.P., Tu J.Y., Ho M.K.M. (2008), Fundamental Consideration of Wall Heat Partition of Vertical Subcooled Boiling Flow, Int J Heat Mass Transf, 51, 3840-3853.

192. Judd R.L. (1999), The role of bubble waiting time in steady nucleate boiling, ASME J Heat Transf, 121, 852-855.

193. Dhir V.K. (1998), Boiling heat transfer, Annu Rev Fluid Mech, 30, 365–40.

194. Han C.Y., Griffith P. (1962), The Mechanism of heat transfer in nucleate pool boiling, Report no. 7673-19, Massachusetts Institute of Technology, Cambridge, Massachusetts.

195. Fazel S.A.A., Shafaee S.B. (2010), Bubble dynamics for nucleate pool boiling of electrolyte solutionsASME J Heat Transf, 132, 1-7.

196. Li J., Cheng P. (2004), Bubble cavitation in a microchannels, Int J Heat Mass Transf, 47, 2689–2698.

197. Kandlikar, S.G., Garimela, S., Li, D., Colin, S., King, M.R., (2006) Heat Transfer and Fluid Flow in minichannels and Microchannels, Elsevier, Oxford, UK (ISBN: 0080444903).

198. Kenny T.W., Goodson K.E., Santiago J.G., Wang E., Koo J.M., Jiang L., Pop E., Sinha S., Zhang L., Fogg D., Yao S., Flynn R., Chang C.H., Hidrovo C.H. (2006), Advanced cooling technologies for microprocessors, Int J High Speed Ele Sys,16, 301-313.

199. Mukherjee A., Kandlikar S.G. (2009), The effect of inlet constriction on bubble growth during flow boiling in microchannels, Int J Heat Mass Transf., 52, 5204-5212.

200. Munson B.R., Okiishi, T.H., Huebsch, W.W., Rothmayer, A.P., (2013), Fundamental of Fluid Mechanics, seventh Ed. John Wiley and Sons, USA (ISBN 978-1-118-11613-5).

201. Kosar, A., Peles, Y., Bergles, A.E., Cole, G.S., (2009), Experimental Investigation of Critical Heat Flux in Microchannels for Flow Field Probes, ASME Seventh Int Conference on Nanochannels, Microchannels and Minichannels, June 22-24, Pohang, South Korea.

202. Kaya A., Ozdemir M.R., Kosar A. (2013), High mass flux flow boiling and critical heat flux in microscale, Int J Therm Sci, 65, 70-78.

203. Inasaka F., Nariai, H. (1992), Critical heat flux of subcooled flow boiling for water in uniformly heated straight tubes, Fusion Engg Des,19, 329–337.

204. Sumith B., Kaminaga F., Matsumura K. (2003), saturated flow boiling of water in a vertical small diameter tube, Exp Therm Fluid Sci**,** 27, 789–801.

205. Wu H.Y., Cheng P. (2003), Visualization and measurements of periodic boiling in silicon microchannels, Int J Heat Mass Transf, 46, 2603–2614.

206. Chen T., Garimella S.V. (2012), A Study of critical heat flux during flow boiling in microchannel heat sinks, ASME J Heat Transf, 134, (DOI:10.1115/1.4004715).

207. Xie G., Chen Z., Sunden B., Zhang W. (2013), Numerical predictions of flow and thermal performance of water-cooled single-layer and double-layer wavy microchannel heat sinks, Num Heat Transf A, 63, 201–225.

208. Ghaedamini H., Lee P.S., Teo C.J. (2013), Developing forced convection in converging‑diverging microchannels, Int J Heat Mass Transf, 65, 491‑499.

209. Steinke M.E., Kandlikar S.G. (2004), Review of single-phase heat transfer enhancement techniques for application in microchannels, minichannels and microdevices, Int J Heat Tech, 22, 3–11.

210. Jung J.Y., Oh H.S., Kwak H.Y. (2009), Forced convective heat transfer of nanofluids in microchannels, Int J Heat Mass Transf, 52, 466–472.

211. Byrne M.D., Hart R.A., Silva A.K. (2012), Experimental thermal-hydraulic evaluation of CuO nanofluids in microchannels at various concentrations with and without suspension enhancers, Int J Heat Mass Transf, 55, 2684–2691.

212. Wang X.D., An B., Lin L., Lee D.J. (2013), Inverse geometric optimization for geometry of nanofluid-cooled microchannel heat sink, Appl Therm Engg, 55, 87‑94.

213. Wang X.D., An B., Xu J.L. (2013), Optimal geometric structure for nanofluid-cooled microchannel heat sink under various constraint conditions, Energy Convers Manage, 65, 528‑538.

214. Kandlikar S.G, Widger T., Kalani A., Mejia V. (2013), Enhanced flow boiling over open microchannels with uniform and tapered

gap manifolds, ASME J Heat Transf, 135, (DOI: 10.1115/1.4023574).

215. Kalani A., Kandlikar S.G. (2014), Evaluation of pressure drop performance during enhanced flow boiling in open microchannels with tapered manifolds, ASME J Heat Transf, 136, (DOI: 10.1115/1.4026306).

216. Yadav V., Baghel K., Kumar K., Kadam S.T. (2016), Numerical investigation of heat transfer in extended surface microchannels, Int J Heat Mass Transf, 93, 612‑622.

217. Yan F, Lee P.S., Jin L.W., Chua B.W. (2014), Experimental investigation on heat transfer and pressure drop of a novel cylindrical oblique fin heat sink, Int J Therm Sci, 76, 1-10.

218. Sahar A., Ozdemir M.R., Fayyadh E.M., Wissink J., Mahmoud M.M, Karayiannis T.G. (2016), Single phase flow pressure drop and heat transfer in rectangular metallic microchannels, Appl Therm Engg, 93, 1324-1334.

219. Ozdemir M.R., Mahmoud M.M, Karayiannis T.G. (2016), Flow boiling heat transfer in a rectangular copper microchannel, J Therm Engg, 2, 761-773.

220. Holman J.P., (2010), Experimental methods for engineers, seventh Ed. Tata McGraw hill, New York (ISBN 9780070647763).